Dissertation

submitted to the

Combined Faculties for the Natural Sciences and for Mathematics

of the Ruperto-Carola University of Heidelberg, Germany

for the degree of

Doctor of Natural Sciences

Put forward by

Dipl.-Phys. Fabian Allmendinger

Born in: Wuppertal

Oral examination: January 21st, 2015

Precise Tests of Fundamental Symmetries at Low Energies using a ^{3}He-^{129}Xe Comagnetometer

Referees: Herr Priv.-Doz. Dr. Ulrich Schmidt

Herr Prof. Dr. Ulrich Uwer

Zusammenfassung:

Verschiedene Theorien, die die Physik jenseits des Standardmodells beschreiben, sagen neue Phänomene bei derart hohen Energien vorher, die in Beschleunigerexperimenten nicht zu erreichen sind. Als Alternative werden bestimmte Größen bei niedrigen Energien sehr präzise gemessen und mit deren Standardmodellvorhersagen verglichen. Im Rahmen dieser Dissertation werden zwei experimentelle Herangehensweisen behandelt: Zum einen würden Effekte der Quantengravitation auf der Planck-Skala, obwohl stark unterdrückt, noch bei niedrigen Energien Auswirkungen haben. Dies wird mit Tests der CPT- und Lorentzinvarianz-verletzenden Kopplung des (gebundenen) Neutronspins an ein hypothetisches Hintergrundfeld untersucht. Zweitens tragen zusätzliche Quellen von CP-Verletzung zu einem permanenten elektrischen Dipolmoment (EDM) bei, das mehrere Größenordnungen über der Standardmodellvorhersage liegen kann. Genaue Messungen des EDMs von ^{129}Xe können darüber wichtige Aufschlüsse geben. Der experimentelle Ansatz beruht auf der Frequenzmessung von frei präzedierenden, kernspinpolarisierten ^{3}He- und ^{129}Xe-Atomen in einem homogenen Magnetfeld (400nT). Als Detektoren werden rauscharme LT$_C$ SQUIDs eingesetzt. Diese Dissertation behandelt den experimentellen Aufbau und die Datenauswertung zur Suche nach einer CPT- und Lorentzinvarianz-verletzenden Kopplung der ^{3}He- und ^{129}Xe-Spins an ein Hintergrundfeld. Aus den Daten konnte eine obere Grenze von $\tilde{b}_{\perp}^{\mathrm{n}} < 8.4 \cdot 10^{-34}$ GeV (68% C.L.) für die äquatoriale Komponente des Hintergrundfeldes bestimmt werden. Des Weiteren werden die Vorbereitungen und technischen Entwicklungen für die ^{129}Xe-EDM-Messungen beschrieben.

Abstract:

Effects of theories beyond the Standard Model would become directly apparent at high energies, which are probably out of reach for colliders. As an alternative, low-energy high-precision measurements of quantities are performed, looking for deviations from the Standard Model (SM) predictions. In this case: Firstly, a small amount of the large effects of quantum gravity at the Planck scale should remain at low energies, which is tested by looking for Lorentz invariance violation in the neutron sector. Secondly, new sources of CP-violation would cause permanent electric dipole moments (EDMs) of particles that are many orders of magnitude larger than the EDMs predicted by the SM. The experimental approach is to measure the free precession of nuclear spin polarized ^{3}He and ^{129}Xe atoms in a homogeneous magnetic guiding field of about 400 nT using LT$_C$ SQUIDs as low-noise magnetic flux detectors. This dissertation reports on the search for a CPT and Lorentz invariance violating coupling of the ^{3}He and ^{129}Xe nuclear spins to posited background fields. An upper limit on the equatorial component of the background field interacting with the spin of the bound neutron $\tilde{b}_{\perp}^{\mathrm{n}} < 8.4 \cdot 10^{-34}$ GeV (68% C.L.) was obtained. Furthermore, the technical developments and preparations for measurements of the ^{129}Xe EDM are described.

Contents

1 Introduction and Theoretical Motivation

The Standard Model (SM) of particle physics in combination with the theory of General Relativity (GR) provides an excellent description of nature and is successful to a great extent. However, there are a number of theoretical issues and as yet unexplained experimental observations, which have led to the general understanding that theoretical developments are needed to overcome the deficiencies of the SM and GR, usually referred to as "Physics beyond the Standard Model".
In the following sections, a range of theoretical problems with the SM and GR, as well as experimental observations that cannot be explained within the SM, are presented. Possible theoretical solutions are outlined. Then I will discuss the ways in which the low-energy, high-precision experiments which are presented in this dissertation can help us decide which theory is currently the best description of nature - or shed light on as yet undiscovered properties of nature.

1.1 Unsolved Problems in the Present Description of Nature

Theoretical problems

Our present description of gravity is based on Albert Einstein's theory of General Relativity (GR), which is formulated within the framework of classical (non-quantum) physics. GR models gravity as a curvature of space-time. The curvature is directly related to the mass (or energy) of matter or radiation. On the other hand, the electromagnetic, weak, and strong interactions are described by means of quantum field theories, a radically different formalism for describing physical phenomena using particle fields embedded in the flat space-time of special relativity. Thus GR and the SM must be regarded as incompatible. The first approaches in combining these theories that come into mind - like treating gravity as another particle field - lead immediately to mathematical problems (renormalization problem).
As Einstein's theory is not a quantum theory, it is to be expected that it will ultimately be replaced by a more fundamental theory that will hold at the quantum level. Possible quantum gravity theories are string theory and loop quantum gravity, for example. At a certain scale, gravity and quantum physics are expected to meet. An upper limit for this scale is the Planck scale, with the Planck mass $m_P \approx 10^{19}$ GeV.
Some quantum gravity theories, such as string theory, are intended to unify gravity with the other fundamental interactions, whereas others, such as loop quantum gravity, are constructed to quantize the gravitational field while keeping gravity separate from the other interactions. A theory of quantum gravity which also unifies all known interactions, is usually referred to as a "theory of everything" (TOE).
One of the difficulties of quantum gravity is its experimental accessibility. Quantum

gravitational effects are only expected to become apparent near the Planck scale, a scale far higher in energy than that which is accessible to particle accelerators at the moment (and most likely in the foreseeable future). Therefore, one must think about experimental alternatives.

The **Strong CP problem** is the as yet unsolved question of why quantum chromodynamics (QCD) does not violate CP symmetry, although the underlying theory allows such a violation: There are natural terms in the QCD Lagrangian with the CP symmetry breaking parameter Θ. One would assume that the angle Θ would naturally be of order one. However, there are no experimental results that indicate any CP violation in the QCD sector. The particular value of Θ that must be very close to zero (experimental result from neutron electric dipole moment measurements: $\Theta < 10^{-10}$) is an example of a fine-tuning problem.
There are several proposed solutions to the Strong CP problem: Firstly, the CP symmetry breaking parameter Θ would become unobservable if at least one of the quarks were massless. However, there is no experimental evidence that any of the quarks is massless, and thus this mechanism seems very unlikely.
Secondly, the Peccei-Quinn theory offers an alternative solution to the Strong CP problem. An additional global U(1) symmetry (referred to as the PQ symmetry) is introduced into the SM QCD Lagrangian and is subsequently broken both spontaneously and explicitly. The breaking of the PQ symmetry gives rise to a pseudoscalar Nambu-Goldstone boson, known as the **Axion**, which causes Θ to become effectively zero.

Unexplained experimental observations

One of the prominent unsolved questions in physics today is related to the origin of matter: Why is our world made of matter, and why is there no relevant amount of anti-matter in the observable Universe? The observed Matter-Antimatter Asymmetry, or **Baryon Asymmetry** $A = \frac{n_B - n_{\overline{B}}}{n_\gamma} \approx 10^{-10}$ (with the density of matter n_B, the density of anti-matter $n_{\overline{B}}$ and the photon density n_γ) is much larger than the expected asymmetry of $A \approx 10^{-18}$ from baryogenesis models based on the SM.
To generate a Baryon Asymmetry, three conditions (Sakharov conditions) must be satisfied, if one assumes CPT conservation [1]:
There must be:

- a Baryon number violating process
- a C-symmetry and CP-symmetry violating process
- a system out of thermal equilibrium.

The CP-violating processes in the SM in the weak interaction are far too small to explain the observed Baryon Asymmetry. As a consequence, the search for additional sources of CP violation is essential.
Alternatively, the observed baryon asymmetry can be explained, if CPT symmetry is not conserved and if there are processes that violate baryon-number conservation (in this case there is no need for a system out of thermal equilibrium). As CPT invariance is closely linked to Lorentz invariance via the CPT theorem [2, 3], it makes sense to search for Lorentz invariance violations to put stringent limits on a violation of CPT symmetry.

Another unsolved question of great importance in contemporary physics is the identity of **Dark Matter**. Dark matter neither emits nor absorbs electromagnetic radiation at a measurable level, but the existence of dark matter is generally accepted on the basis of overwhelming astrophysical evidence: the existence and properties of dark matter are inferred from its gravitational effects on visible matter, radiation, and the large-scale structure of the universe. Much of the evidence for dark matter comes from the observation of the motions of galaxies and from observations of gravitational lensing of galaxy clusters. This allows us to directly estimate the gravitational masses of galaxies, clusters of galaxies and the entire universe. These masses are significantly higher than the mass of the visible matter these objects contain. According to the data of the Planck spacecraft mission, the universe contains 4.9% baryonic matter, 26.8% dark matter and 68.3% dark energy [4]. Among others, the **Axion** which has been mentioned above is a possible dark matter candidate.

1.2 Lorentz Invariance Violation

The negative results of the famous Michelson-Morley experiment in 1887 [6], which looked for an anisotropy in the speed of light, finally led to the formulation of Einstein's theory of special relativity. This theory is based on the postulate that the laws of physics are invariant under Lorentz transformations (boosts and rotations). Lorentz invariance has become one of the fundamental symmetries in modern physics since then. Modern Michelson-Morley type experiments improved the limits by a factor 4000.
Over the last few decades there has been increasing interest in tests of Lorentz invariance for the following reasons:
As stated above, the effects of a theory of quantum gravity would appear at the Planck scale. If Lorentz invariance is violated by quantum gravity, it should be strongly violated at $m_P \approx 10^{19}$ GeV. Experimental investigations at the Planck scale are beyond our reach, as current colliders work at the TeV scale and the highest energies found in particles of cosmic radiation are in the order of 10^{11} GeV. However, it is very likely that a small amount of Lorentz invariance violation remains at low energies. As an alternative to high-energy experiments, one can search for tiny Planck-suppressed effects that may be visible in high-precision experiments at low energies. It makes sense to look for signs of Lorentz invariance violation as they cannot be explained within the SM or GR and thus will be a clear indication of new physics. There are mechanisms in both string theory and loop quantum gravity that can lead to Lorentz invariance violation. Though these theories do not presently give verifiable predictions at a quantifiable level at low energies, they motivate experimental searches in this direction.
Furthermore, by putting limits on Lorentz invariance violation, one automatically puts limits on CPT violation, as a CPT violation would immediately lead to a violation of Lorentz invariance. This was shown by O. Greenberg [30]. In our current understanding of nature, CPT symmetry and Lorentz invariance are fundamental properties, and thus both must be thoroughly tested in experiments.
An approach that helps to bridge the gap between theories that do not give definite testable predictions at the moment (although they motivate searches in this direction)

on the one side, and experiments on the other side, is effective field theory. Every reasonable effective field theory must:

- contain the SM
- contain GR
- contain any higher couplings between the SM and GR
- be invariant under *observer* Lorentz transformation. (The results of an experiment are not dependent on the chosen coordinate system of the observer.)

In contrast to the *observer* Lorentz invariance, violations of *particle* Lorentz invariance are allowed, meaning that physics may change as an individual particle field is rotated or boosted while the coordinate system remains fixed. The general effective field theory that has all of the properties listed above is called the Standard Model Extension.

1.2.1 The Standard Model Extension

The theoretical framework presented by A. Kostelecký and colleagues parametrizes the general treatment of CPT and Lorentz invariance violating effects in a Standard Model Extension (SME) [26–28]. The SME framework was conceived to facilitate experimental investigations of Lorentz and CPT symmetry, given the theoretical motivation for violation of these symmetries. Although Lorentz invariance violating interactions are motivated by models such as string theory [28, 31], loop quantum gravity [32–35], etc., the low-energy effective action appearing in the SME is independent of the underlying theory.
The SME lagrange density is constructed to contain all possible terms that violate Lorentz invariance. For practical purposes, in low-energy experiments one usually takes a subset with a finite number of terms, including the leading order effects in Lorentz invariance violation. One special subset, known as the **minimal Standard Model Extension**, is restricted to power-counting renormalizable and gauge-invariant terms. The Lorentz invariance violating coefficients in the minimal SME have been widely used by experimentalists as the standard for reporting bounds on Lorentz invariance violation and comparing experimental sensitivity. Since most of the low-energy experiments involve only electromagnetic interactions between charged particles and photons (effects involving coupling to a gravitational field are expected to be smaller), it often suffices to use a minimal QED sector of the SME.
The Lagrangian of the QED limit of the minimal SME can be written as

$$\mathcal{L}_{\text{QED}} = \mathcal{L}_0 + \mathcal{L}_{\text{int}} \quad . \tag{1.1}$$

The Lagrangian $\mathcal{L}_0$ contains the conventional Lorentz invariant terms in QED describing photons, massive charged fermions, and their usual couplings, while $\mathcal{L}_{\text{int}}$ contains the Lorentz invariance violating interactions. Since the minimal SME in flat spacetime is restricted to the renormalizable and gauge-invariant terms in the full SME, the QED sector interactions in $\mathcal{L}_{\text{int}}$ have a finite number of terms. For the case of photons and a

single fermion species ψ, the Lorentz invariance violating terms are given by

$$\begin{aligned}\mathcal{L}_{\text{int}} &= -a_\mu\bar{\psi}\gamma^\mu\psi - b_\mu\bar{\psi}\gamma_5\gamma^\mu\psi + ic_{\mu\nu}\bar{\psi}\gamma^\mu D^\nu\psi \\ &\quad + id_{\mu\nu}\bar{\psi}\gamma_5\gamma^\mu D^\nu\psi - \tfrac{1}{2}H_{\mu\nu}\bar{\psi}\sigma^{\mu\nu}\psi \\ &\quad -\frac{1}{4}(k_F)_{\kappa\lambda\mu\nu}F^{\kappa\lambda}F^{\mu\nu} + \frac{1}{2}(k_{AF})^\kappa\epsilon_{\kappa\lambda\mu\nu}A^\lambda F^{\mu\nu} \quad ,\end{aligned} \tag{1.2}$$

with $iD_\mu := i\partial_\mu - qA_\mu$. The terms with coefficients a_μ, b_μ and $(k_{AF})_\mu$ are odd under CPT, while those with $H_{\mu\nu}$, $c_{\mu\nu}$, $d_{\mu\nu}$, and $(k_F)_{\kappa\lambda\mu\nu}$ preserve CPT. All seven terms violate Lorentz invariance. In general, superscript labels will be added to these parameters to denote the (fundamental) particle species [27–29].
Lagrangian terms of the same form are expected to describe composite particles - in particular protons and neutrons - in QED systems as well. Then the SME coefficients represent composites stemming from quark and gluon interactions. Since QED and its relativistic quantum-mechanical limits describe proton and neutron electromagnetic interactions in atoms in excellent agreement with experiments, defining terms involving composite SME parameters for protons and neutrons is a reasonable extension of the theory. The QED extension of the SME treats protons and neutrons as the basic constituents of the theory. The Lagrangian $\mathcal{L}_{\text{int}}$ then contains the most general set of Lorentz invariance violating interactions in this context. The new parameters of these terms are denoted using tildes.
For example, the parameters that are important for this work are the $\tilde{b}$ coefficients. They are defined as

$$\tilde{b}_J^w := b_J^w - md_{J,0}^w - \tfrac{1}{2}\epsilon_{Jkl}H_{kl}^w \quad (\text{with } J = X,\ Y,\ Z\ ; \quad w = e,\ p,\ n) \tag{1.3}$$

for the electron, proton, and neutron, respectively. Finally, the leading-order effects of the interactions can be determined. It suffices to use a non-relativistic description of a potential V for the particles involved given by

$$V = -\tilde{\boldsymbol{b}}^{\boldsymbol{w}}\cdot\boldsymbol{\sigma}^{\boldsymbol{w}} \quad (\text{with } w = e,\ p,\ n)\ . \tag{1.4}$$

This can be interpreted as a coupling of the electron, proton, or neutron spin $\boldsymbol{\sigma}^{\boldsymbol{w}}$ to a hypothetical background field $\tilde{\boldsymbol{b}}^{\boldsymbol{w}}$ (see Fig. 1.1).
The SME coefficients are expected to be fixed with respect to a nonrotating coordinate frame, e.g. with respect to distant stars. The suitable choice of a coordinate frame fixing the directions X, Y, Z is a sun-centered frame using celestial equatorial coordinates. Further information on the coordinate systems and transformations that are used in this work can be found in Appendix A.1 on page 127.
Finally, the experimental task is to search for a coupling of the electron, proton, or neutron spin $\boldsymbol{\sigma}^{\boldsymbol{w}}$ to a hypothetical background field $\tilde{\boldsymbol{b}}^{\boldsymbol{w}}$.

1.2.2 Experimental Searches for Lorentz Invariance Violation

There is a huge variety of possible tests of Lorentz invariance, including astrophysical observations (e. g. vacuum birefringence), and experiments on earth using Penning traps or cavities (like the Michelson-Morley experiment). Thus, the following presentation is narrowed down to experiments that measure the SME parameters $\tilde{b}_J^w$ with

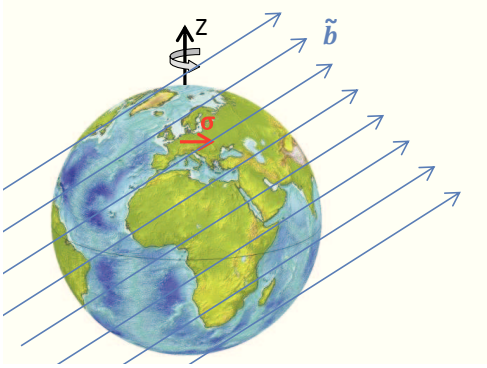

Figure 1.1: Illustration of the coupling $V = -\tilde{b}_J^w \cdot \sigma_J^w$. The hypothetical background field $\tilde{b}_J^w$ is fixed with respect to distant stars, whereas the spins rotate with the Earth.

methods that are similar to the ^{3}He-^{129}Xe comagnetometer in this work.
Up until now, experiments were consistent with Lorentz invariance and resulted in the determination of upper limits on the SME coefficients. Typical experiments, which are briefly described here, look for couplings between the hypothetical background fields and particle properties, such as spin (or propagation direction). As earthbound experiments are unavoidably rotating and revolving relative to the Sun-centered frame, a coupling would manifest in an annual and sidereal variation of a specific observable (usually the energy levels of particles or atoms). Since the translational motion of the Earth around the Sun is non-relativistic, annual variations are typically suppressed by a factor 10^{-4}. Thus sidereal variations are the leading time-dependent effect to look for in experimental data.

Hughes-Drever type experiments

Hughes *et al.* [9] and Drever *et al.* [10] independently measured the Larmor frequency of ^{7}Li, and looked for sidereal frequency changes as the laboratory frame rotated with respect to distant stars.
Hughes–Drever type experiments, sometimes referred to as "clock comparison experiments" (but it has to be pointed out, that this is not a measurement of time dilation), in general are spectroscopic tests of the isotropy of mass and space. As in Michelson–Morley experiments, they test the existence of a preferred frame of reference. However, unlike Michelson–Morley type experiments, Hughes–Drever experiments test the isotropy of the interactions of matter itself. The accuracy that can be achieved makes these experiments one of the most accurate confirmations of relativity. Searches for an anomalous spin coupling to a posited relic background field that permeates the universe, have been performed with electron and nuclear spins with increasing sensitivity [11, 12, 14–22, 24, 25]. A list of the best limits on spin-anisotropy can be found in Tab. 1.1.
The common principle of modern Hughes-Drever type experiments is the use of at least two different systems which are radiating on their Zeemann transitions. A coupling of

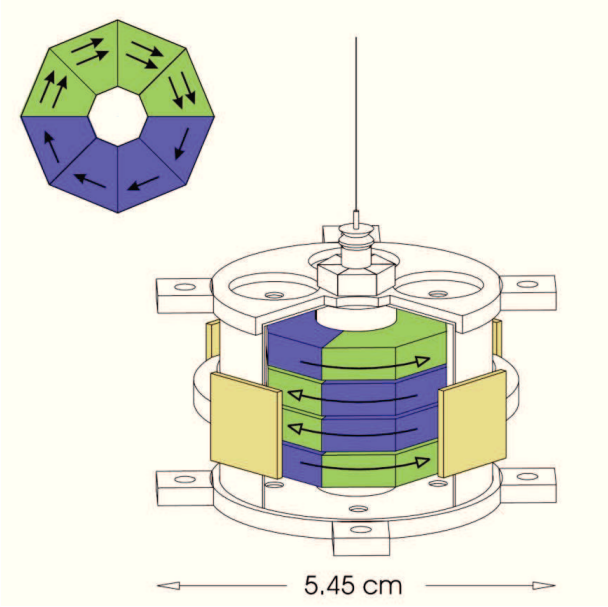

Figure 1.2: A drawing of the spin pendulum as it was used by the Eöt-Wash group. The light green and darker blue parts are made of Alnico and $SmCo_5$, respectively. Upper left: Top view of a single puck; the effective spin polarization points to the right. Lower right: The assembled pendulum with the magnetic shield shown cut away to reveal the four pucks inside. Two of the four mirrors (light gold), that are used to monitor the pendulum twist, are prominent. Arrows with filled heads show the relative densities and directions of the electron spins, open-headed arrows show the directions of the magnetic field. Source: [22].

the spins to a posited relic background field would change the Larmor frequencies.

Spin-polarized torsion balance

With the spin-polarized torsion balance of the Eöt-wash group at the University of Washington, new interactions that couple to the electron spin have been investigated [22]. Among others, upper bounds for the couplings of the electron spin to hypothetical background fields as described by the SME could be derived (see Tab. 1.1). The central part of the experiment is a spin pendulum (see Fig. 1.2) that contains a high number (in the order of 10^{23}) of polarized electrons, while having a negligible external magnetic moment and a high gravitational symmetry. The spin pendulum consists of four octagonal "pucks". One half of each puck is made of Alnico 5 (a conventional soft ferromagnet in which the magnetic field is almost entirely created by electron spins) and the other half is made of $SmCo_5$, a hard rare-earth magnet in which the orbital magnetic moment of the electrons in the Sm^{3+} ion nearly cancels the spin magnetic moment. Having this spin pendulum with aligned electron spins and no net magnetic moment, the experiment then makes use of a substantially improved version of the Eöt-Wash rotating torsion balance that was used earlier for tests of the equivalence principle.

Briefly, a vacuum vessel containing the torsion pendulum on a tungsten suspension fiber and its associated optical readout system was rotated uniformly on a turntable about a vertical axis. Magnetic fields and gradients were reduced by active and passive shielding (a stationary set of Helmholtz coils and four layers of co-rotating mu-metal shielding). Gravity gradients were canceled with a precision that was limited by the fluctuating water content of the ground outside the laboratory. The turntable stood on thermally adjustable feet that kept its rotation axis in a vertical position (better than 10 nrad). Over the course of the experiment the turntable rotation frequency f was set to different values (between $\frac{3}{29}f_0$ and $\frac{3}{20}f_0$, where f_0 is the free-oscillation frequency of the pendulum). The pendulum twist angle Θ was recorded as a function of the turntable angle Φ by means of the optical readout system. This signal was processed to extract the torque. A Lorentz invariance violating coupling of the type $V = -\boldsymbol{\sigma} \cdot \tilde{\boldsymbol{b}}^{\boldsymbol{e}}$ would cause a orientation dependent torque, and thus, a signal $\Theta(\Phi) \propto \sin(\Phi)$. Upper bounds on such a signal in the data can finally be used to extract the limits on Lorentz invariance violation, $|\tilde{\boldsymbol{b}}^{\boldsymbol{e}}| < 10^{-31}$ GeV, thereby largely ruling out effects in first order Planck scale suppression (see Tab. 1.1).

Experiment	Authors	Year	Constraints on $\tilde{b}_J^w$ in GeV			Description	
			Proton	Neutron	Electron		
^{3}He-^{129}Xe comagnetometer	Cané *et al.*	2004		10^{-32}		Zeemann maser	[21]
Spin-torsion pendulum	Heckel *et al.*	2006			10^{-30}	Spin-polarized torsion balance	[23]
	Heckel *et al.*	2008			10^{-31}		[22]
K-^{3}He comagnetometer	Brown *et al.*	2010	10^{-32}	10^{-33}		Zeemann maser	[12]
^{21}Ne-Rb-K comagnetometer	Smiciklas *et al.*	2011		10^{-29}		Zeemann maser	[13]
Hg-Cs comagnetometer	Peck *et al.*	2012	10^{-30}	10^{-31}		Zeemann maser	[25]
^{3}He-^{129}Xe comagnetometer	Gemmel *et al.*	2010		10^{-32}		Free running comagnetometer	[37]
	Allmendinger *et al.*	2014	10^{-33}	10^{-34}			[5, 53]
First order Planck supression			10^{-19}	10^{-19}	10^{-26}		
Second order Planck supression			10^{-38}	10^{-38}	10^{-48}		

Table 1.1: Experimental limits on SME parameters $\tilde{b}_J^w$ using spin-polarized systems (comagnetometers and torsion balances). (Selection of experiments with the highest sensitivities.) The last two rows give the orders of magnitude in Planck supression $\Delta E^{(n)} \sim (\frac{m_w}{M_p})^n \cdot m_w$, where the low energy scale is set by the mass m_w of the particle.

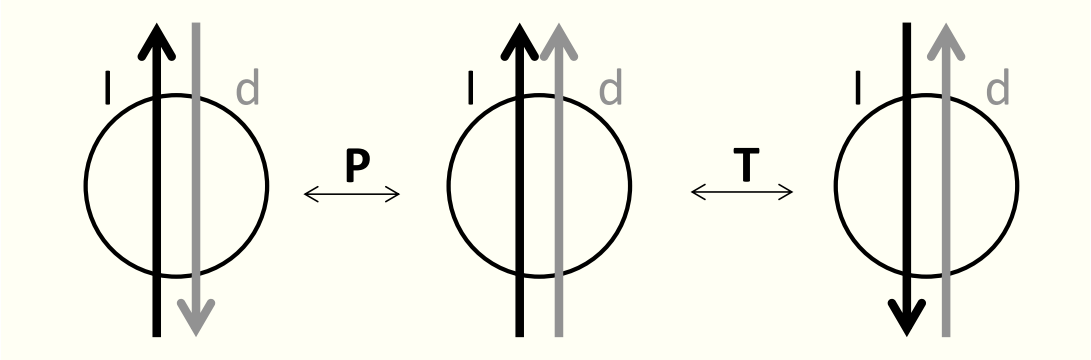

Figure 1.3: A permanent electric dipole moment of a particle violates both P and T symmetries and thus violates CP symmetry (assuming CPT conservation). Under parity transformation P, the electric dipole moment $\boldsymbol{d}$ changes sign, whereas the spin $\boldsymbol{I}$ stays unchanged. Under time reversal T, $\boldsymbol{d}$ stays unchanged, but $\boldsymbol{I}$ changes sign.

1.3 CP Violation and Permanent Electric Dipole Moments of Particles

Until 1956 it was assumed that all physical processes are invariant under time reversal T, charge conjugation C and spatial or parity inversion P. These symmetries were considered as fundamental properties and every allowed process would transform into an allowed process by applying one of the T, C, or P transformations. Early tests showed that parity was conserved in gravity and in the electromagnetic and strong interaction. Then, in 1956, the famous Wu experiment used the beta decay of polarized ^{60}Co to show that the weak interaction violates P symmetry to the maximum extent. Only the left-handed components of particles (e.g. left-handed neutrinos) and right-handed components of antiparticles (e.g. right-handed anti-neutrinos) participate in weak interactions. Parity transformation leads to particles that do not exist (e.g. right-handed neutrinos or left-handed anti-neutrinos). The same argument is valid for charge conjugation C (e.g. transforming left-handed neutrinos into left-handed anti-neutrinos). Therefore, the separate C and P symmetries are violated in the weak interaction of the SM. However, the combination of both transformations, the CP transformation, leads to particles that do exist (e. g. transforming a left-handed neutrino into a right-handed anti-neutrino). Thus, in the following years, it was assumed (or hoped) that CP symmetry is still conserved.
In 1964, a violation of CP symmetry was found in the decay of neutral Kaons and later in the B-meson system. This CP violation is small (compared to the maximal violation of parity) and a property of the weak interaction. So far, CP violation has only been observed in the weak interaction. The CP violation is well described in the SM as a complex phase factor δ. This phase factor is one of the four free parameters of the Cabibbo-Kobayashi-Maskawa (CKM) matrix, which describes the quark-mixing. δ only causes CP violation in flavor-changing processes, and all CP-violating processes that are

known today occur through quark interaction involving that phase.
Nevertheless, QCD also allows CP violation in the strong interaction, with the term parameterized by Θ, which was found to be $\Theta < 10^{-10}$ by experiments measuring the neutron EDM as described above (strong CP problem and the axion).
However, there are strong arguments, that CPT symmetry as a result of the simultaneous combination of the three transformations C, P, and T is conserved. This is based on the CPT theorem of Pauli and Lüders [3], which follows from fundamental principles: causality, locality, and Lorentz invariance. The connection between Lorentz invariance and CPT has been mentioned in the previous section.
Because a part of this dissertation addresses the experimental efforts to measure the EDM of ^{129}Xe, the connection between CP violation and permanent electric dipole moments will be described below.
A permanent EDM of a fundamental or composite particle must be aligned parallel to the Spin $\boldsymbol{I}$, as the spin is the only available vector for an eigenstate of the isolated particle. Otherwise, there would have to be a further quantum number that describes the direction of the EDM (parallel or anti-parallel to the spin), and this would lead to additional states that obviously do not exist (Pauli principle). Therefore:

$$\boldsymbol{d} = d \cdot \frac{\boldsymbol{I}}{|\boldsymbol{I}|} \quad . \tag{1.5}$$

If one now applies P (inverting all spatial coordinates), the electric dipole moment $\boldsymbol{d}$ changes sign, whereas the spin $\boldsymbol{I}$ stays unchanged. Furthermore, under time reversal T, $\boldsymbol{d}$ stays unchanged, but $\boldsymbol{I}$ changes sign (see Fig. 1.3). Assuming CPT symmetry conservation, this is equivalent to CP symmetry violation.
As such, an EDM is an excellent candidate to look for new sources of CP violation, with its connection to the observed matter-antimatter asymmetry in our universe, as explained above. Furthermore, the Standard Model predictions for EDMs are very small. They occur only at the four-loop or higher level, stemming from the CP violation in the weak interaction. For example, since the complex phase factor of the CKM matrix only enters in matrix elements where heavier quarks are involved, SM contributions to particle EDMs - in particular, the neutron EDM - are of second order in the weak interaction coupling constants, and hence are very small: of order $d_n \approx 10^{-31}$ to 10^{-33} ecm. The SM prediction for the electron EDM is even smaller: $d_e \approx 10^{-37}$ to 10^{-40} ecm. A significantly larger EDM would be a clear indication of physics beyond the SM.
Many experiments have been and are currently being conducted to measure the EDMs of several particles. All of these measurements are consistent with a vanishing dipole moment. However, these results can be used to extract limits on CP symmetry violation that a theoretical model may permit. For example, in supersymmetric models (SUSY), by doubling the number of fundamental particles, quite a few new parameters with additional CP-violating phases are introduced that contribute to EDMs. In the simplest SUSY model (minimal supersymmetric standard model), with only two additional CP-violating phases, the natural size of EDMs would be in the order of $|d_n| = 10^{-25}$ to 10^{-28} ecm. Current experimental results show such large EDMs to be unlikely (see below), which presents a serious challenge for SUSY.
In principle, the EDMs of different systems should be measured to distinguish between the various sources of CP violation that can be intrinsic leptonic, intrinsic hadronic,

resulting from interactions in composite particles, or CP-odd forces between the constituents in atoms, for example (see Fig. 1.4). In some composite systems, such as molecules and atoms, internal fields can significantly enhance or attenuate the visibility of EDMs, which must also be taken into account. The highest sensitivity so far could be reached in measurements of the neutron, the ^{129}Xe atom, the diamagnetic ^{199}Hg atom (predominantly sensitive to the nuclear EDM), and the ThO molecule (predominantly sensitive to the electron EDM).

1.3.1 The EDM of ^{129}Xe

This experiment, using a ^{3}He-^{129}Xe comagnetometer, is an attempt to measure the atomic EDM of ^{129}Xe. Thus the individual sources of EDMs which contribute to the total atomic EDM will be presented.
An atomic EDM of a composite particle like the ^{129}Xe atom would arise from intrinsic EDMs of the elementary fermions or from the interaction between these constituents. The various theories like SUSY, Left-Right Symmetry, Technicolor, and Multi-Higgs, which incorporate new sources of CP violation, should give direct predictions concerning the value of EDMs of the fundamental particles, especially the electron EDM d_e, and the quark EDMs, as well as possible CP-violating quark-lepton interactions and "ChromoEDMs" (stemming from the quark-quark interaction). Then extensive QCD calculation is needed to get to the resulting nucleon EDMs (neutron EDM d_n) and CP-violating nucleon-nucleon interactions. Afterwards, nuclear models must be applied to calculate the resulting nuclear EDM. Finally, the atomic EDM can be determined using atomic theory incorporating the nuclear EDM, the electron EDM, and CP-violating quark-lepton forces.
On the electron and nucleon level, the different contributions to the atomic EDM can be categorized by the different sources:

- an intrinsic EDM of the electron. This effect is large in atoms with an unpaired electron such as Rb. It is quite small for atoms with closed electron shells like Hg and Xe in their ground state.
- CP- and P-violating electron-nucleon interactions. Three relativistically invariant forms for these interactions exist: tensor-pseudotensor interactions with a dimensionless parameter C_T measuring the strength of this interaction, scalar-pseudoscalar interactions with the parameter C_{SP}, and pseudoscalar-scalar interactions with the parameter C_{PS}.
- an EDM of the neutron or proton, or CP- and P-violating nucleon-nucleon interactions with a dimensionless parameter η describing the strength of this interaction.

As the calculation of the final atomic EDM involves a lot of steps with theoretical uncertainties (nuclear models), the relation between the fundamental sources of CP violation and the atomic EDM has large uncertainties. The ^{129}Xe-EDM can be expressed as a linear combination of the various sources with numeric coefficients that are known with a precision of about 30% [62, 63]:

$$\begin{aligned} d_{Xe} &= -10^{-3} d_e + 5 \cdot 10^{-21}\text{ecm} \cdot C_T \\ &\quad +5 \cdot 10^{-23}\text{ecm} \cdot C_{SP} + 1 \cdot 10^{-23}\text{ecm} \cdot C_{PS} + 4.7 \cdot 10^{-26}\text{ecm} \cdot \eta \end{aligned} \tag{1.6}$$

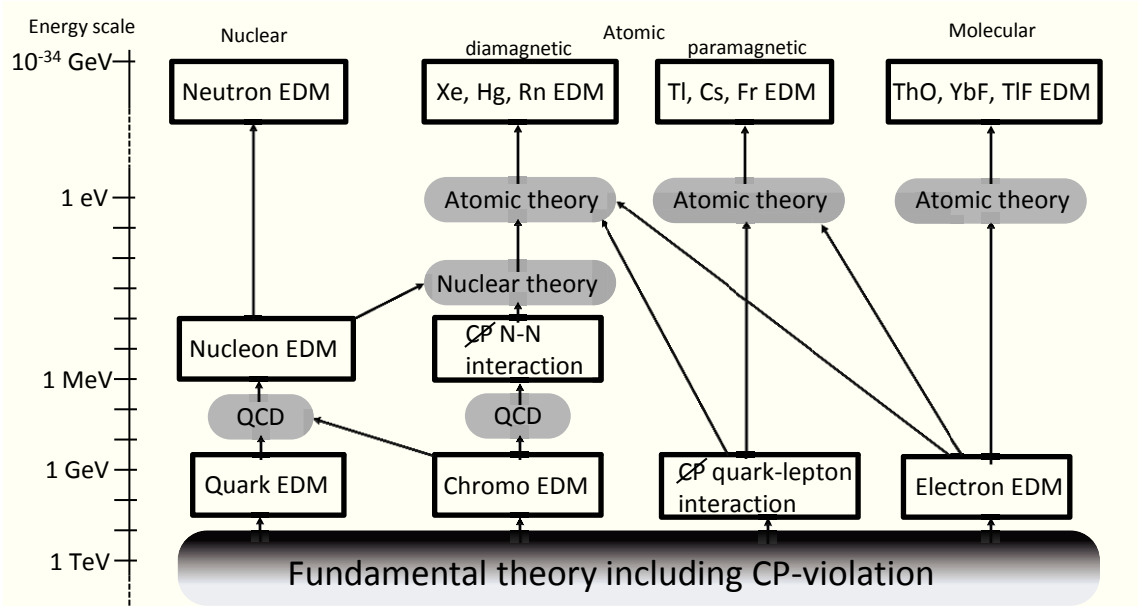

Figure 1.4: The various theories like SUSY, Left-Right Symmetry, Technicolor, Multi-Higgs that incorporate new sources of CP violation should give direct predictions concerning the value of EDMs of the fundamental particles, especially the electron EDM d_e, the quark EDMs as well as possible CP-violating quark-lepton interactions and "ChromoEDMs" (stemming from the quark-quark interaction). Then extensive QCD calculation is needed to get to the resulting nucleon EDMs (neutron EDM d_n) and CP-violating nucleon-nucleon interactions. Afterwards nuclear models have to be applied to calculate the resulting nuclear EDM. Finally, the atomic EDM can be determined using atomic theory incorporating the nuclear EDM, the electron EDM and CP-violating quark-lepton forces. For other particles like the TlF molecule or the neutron much less model dependent assumptions are needed.

1.3.2 Experimental Searches for EDMs of Particles

All experiments that search for an EDM have in common that they use neutral particles with a non-zero total angular momentum $\boldsymbol{F}$, preferably with $F = \frac{1}{2}$. Polarized particles of this type are placed in a magnetic field, and the Larmor precession frequency is measured. By applying an additional electric field $\boldsymbol{E}$ parallel or anti-parallel, an EDM would result in a shift $\delta\omega_p = +2d \cdot E/\hbar$ or $\delta\omega_p = -2d \cdot E/\hbar$ of the precession frequency, respectively. The difference $\omega_p - \omega_a$ in precession frequencies for these two configurations can be measured, and finally the EDM can be calculated (assuming that the magnetic field stays constant):

$$d = \frac{\hbar\,(\delta\omega_p - \delta\omega_a)}{4E} = \frac{\hbar\,(\omega_p - \omega_a)}{4E} \tag{1.7}$$

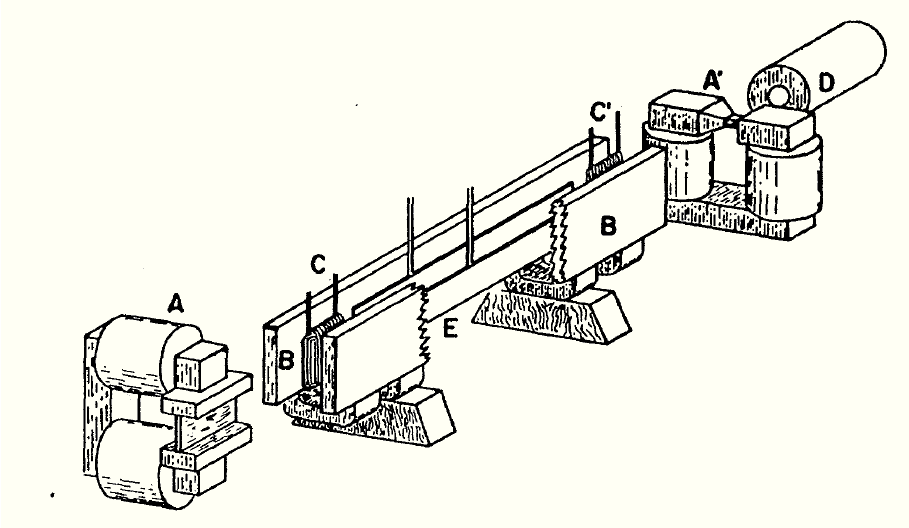

Figure 1.5: Sketch of the experimental set-up to measure the neutron EDM taken from the original publication by J. Smith, E. Purcell and N. Ramsey [68].
A: magnetized iron mirror polarizer, B: the pole faces of the homogeneous field magnet, C and C': rf-coils, A': analyzer and D: detector.

A detailed discussion of the measurement principle will be given in the section "Theory of operation of the ^{3}He-^{129}Xe comagnetometer" on page 29 and the following pages.

The electron EDM via molecular EDMs

The EDM of the electron can be measured in heavy neutral atoms or molecules with exceptionally high internal effective electric fields. Experiments using thallium atoms found $|d_e| < 1.6 \cdot 10^{-27}$ ecm [64], and other experiments using ytterbium fluoride (YbF) molecules found $|d_e| < 1.1 \cdot 10^{-27}$ ecm [65, 66].
The best experimental limit on the electron EDM $\boldsymbol{d_e}$ was published by the ACME collaboration [67] in the year 2014. They used the polar molecule thorium monoxide (ThO) and could take advantage of the high internal electric field $E_{\text{eff}} \approx 84$ GV/cm. They measured $d_e = (-2.1 \pm 3.7_{\text{stat}} \pm 2.5_{\text{syst}}) \cdot 10^{-29}$ ecm. This corresponds to an upper limit of $|d_e| < 8.7 \cdot 10^{-29}$ ecm (90% confidence level).
The experimental method will be shortly described: To measure $\boldsymbol{d_e}$, the ACME collaboration performed a spin precession measurement on collimated pulses of ^{232}Th^{16}O molecules from a cryogenic buffer gas beam source. The molecules enter a magnetically shielded region and pass between parallel plates that generate a laboratory electric field. An aligned spin state is prepared via optical pumping and state preparation lasers. Parallel electric and magnetic fields exert torques on the electric and magnetic dipole moments, causing the spin vector to precess. The precession angle is measured by a laser with rapidly alternating linear polarizations. Then the resulting fluorescence light is collected and detected with photomultiplier tubes. A change in this angle, as the electric field is reversed, is proportional to $\boldsymbol{d_e}$.

The neutron EDM

Measurements of the neutron EDM began in the 1950s and were first carried out by J. Smith, E. Purcell and N. Ramsey [68], applying a magnetic resonance method (see Fig. 1.5). They used a polarized thermal neutron beam at the Oak Ridge reactor. The neutron beam was polarized by total reflection from a polished, magnetized iron mirror, and then passed into a region of a homogeneous magnetic field. A radio frequency magnetic field tuned to the mean Larmor frequency was applied by a small coil. The neutron beam then traveled through a region with a constant electric field and then went through a second rf-coil. Finally, the neutrons were analyzed by an inhomogeneous magnetic field (spatially separating the two spin states) and detected by a BF_3 neutron counter. An electric field changes the Larmor frequency by $\boldsymbol{d_n} \cdot \boldsymbol{E}$, and thus, would shift the spin echo point (i.e. the frequency with the maximal count rate or transmission). The result was by that time remarkably precise: $d_n = (-0.1 \pm 2.4) \cdot 10^{-20}$ ecm, which corresponds to an upper limit of $d_n < 5 \cdot 10^{-20}$ ecm (95% confidence level).
Subsequent measurements using neutron beams could improve the limits on the neutron EDM resulting in $|d_n| < 3 \cdot 10^{-24}$ ecm, but soon systematic uncertainties became dominant (mostly due to the motional magnetic field $\boldsymbol{B} = \boldsymbol{v} \times \boldsymbol{E}/c^2$ that the moving particle sees in an electric field; see p. 118) over statistical uncertainties.
Later experiments could overcome this limitation by using stored ultracold neutrons that had a second advantage: the interaction time of the particles with the electric field could be increased by a factor 10^4. The best limit up to date on the neutron EDM was measured at the Institut Laue-Langevin (published in the year 2006) resulting in $|d_n| < 2.9 \cdot 10^{-26}$ ecm [69].
There is an ongoing interest in the neutron EDM and a lot of experiments in this field are currently planned or in the set-up phase (at the ILL, PSI, FRMII, SNS and TRIUMF) aiming at the 10^{-28} ecm limit.

The ^{199}Hg EDM

The most sensitive measurements to date searching for EDMs in diamagnetic atoms have been performed by Griffith et al. at the University of Washington on ^{199}Hg atoms [70–72]. The ^{199}Hg atom has a $^1S_0$ electronic ground state and nuclear spin 1/2. An EDM of the atom in the ground state would arise from CP violation in the nucleus. The experimental set-up uses a stack of four cells made from high-purity fused silica in a common magnetic field ($B \approx 22\ \mu$T) (see Fig. 1.6). The cells contain enriched ^{199}Hg (92%). The middle two cells have oppositely directed electric fields resulting in EDM-sensitive frequency shifts of opposite sign. The outer two cells are enclosed by the high voltage electrodes, and thus, are in a zero electric field and consequently free of EDM effects. The outer cells are used to reduce magnetic field noise and to provide checks for magnetic field drifts that might be correlated with the applied high voltage (and leakage currents). The ^{199}Hg vapor inside the cells is polarized by means of optical pumping using a 254 nm laser system. After the pumping process, the same laser system is used to monitor the precessing magnetization that decays with a time constant $T_2 \approx 100$ to 200 s. Finally the Larmor frequencies are extracted and compared with respect to different electric field settings (as explained before). The ^{199}Hg EDM was found to be consistent with zero: $d_{Hg} = (0.49 \pm 1.29_{\text{stat}} \pm 0.76_{\text{syst}}) \cdot 10^{-29}$ ecm. An upper limit was extracted: $d_{Hg} < 3.1 \cdot 10^{-29}$ ecm (95% confidence level).

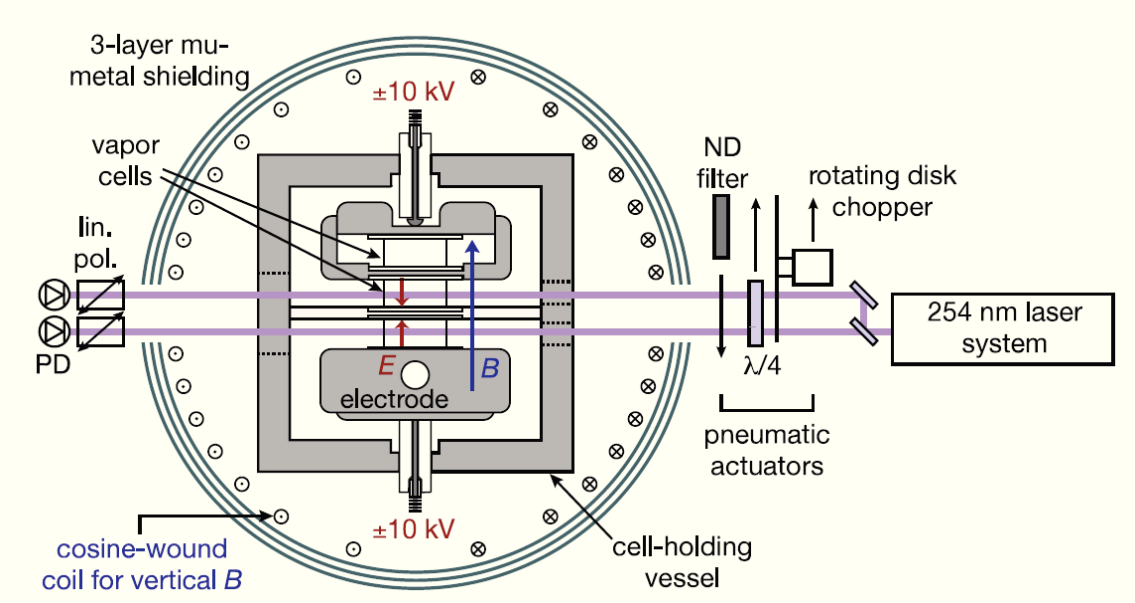

Figure 1.6: Sketch of the experimental set-up to measure the ^{199}Hg EDM taken from the publication by W. C. Griffith [70].

The ^{129}Xe EDM

The most precise measurements of the ^{129}Xe EDM so far have been performed at the University of Michigan by M. A. Rosenberry and T. E. Chupp in the year 2000 [73, 74]. They used a sample of co-located nuclear polarized ^{3}He and ^{129}Xe gas, and thereby constructed a comagnetometer to effectively suppress magnetic field drifts and the corresponding systematic limitations. The principle of comagnetometry is also applied in the measurements that are the topic of this dissertation. Therefore this principle is discussed in detail in Chapter 2 on page 32.

The experimental set-up at the University of Michigan is sketched in Fig. 1.7. The central component is a vessel made of borosilicate glass containing the ^{3}He and ^{129}Xe atoms besides N_2 as a buffer gas, and a small amount of rubidium that is used to polarize both the ^{3}He and ^{129}Xe atoms by Spin Exchange Optical Pumping (SEOP, see page 35). This vessel consists of a spherical pump cell and a cylindrical maser cell, which are connected by a transfer tube. The atoms are nuclear-spin polarized in the pump cell and then diffuse through the transfer tube into the maser cell. The maser cell has molybdenum electrodes to generate the electric field (max. 3.6 kV/cm). The magnetic guiding field (315 μT) is generated by a solenoid, and the whole set-up is surrounded by a three-layer mu-metal magnetic shielding.

The precessing magnetization of the two gases is detected by pickup coils. A feedback mechanism adjusts the current of the solenoid, so that the ^{129}Xe Larmor frequency is kept constant. Then the ^{3}He Larmor frequency is extracted and compared with respect to different electric field settings.

The measurement result after 125 runs (each lasting between eight hours and several

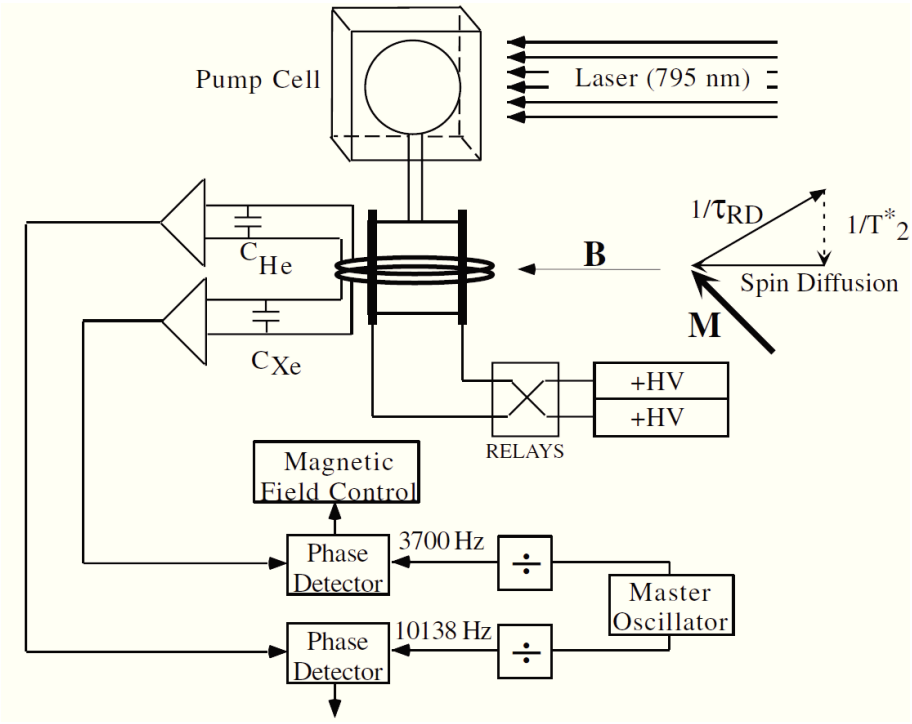

Figure 1.7: Sketch of the experimental set-up to measure the ^{129}Xe EDM using a He-Xe dual maser taken from the publication by M. A. Rosenberry [73]. Inset: The magnetization vector $\boldsymbol{M}$ has a fixed magnitude and projection along the z axis, i.e., steady state oscillation is sustained above threshold due to the equilibrium of three torques: spin diffusion from the pump cell, coherence relaxation, and radiation damping, which depends on $\boldsymbol{M}$.

days) is: $d_{Xe} = (0.7 \pm 3.3_{\text{stat}} \pm 0.1_{\text{syst}}) \cdot 10^{-27}$ ecm.

1.4 Motivation for Low-Energy High-Precision Experiments

To summarize the preceding sections, and to point out the benefit of high-precision experiments at low energies:
It is widely believed that the SM together with GR is a low-energy manifestation of a more complete theory, that perhaps unifies the four fundamental interactions, or at least describes gravity at the quantum level. Many extensions to the SM have been proposed, and these give predictions for physical phenomena that differ from those of the SM. Some searches for new physics beyond the SM are performed at high-energy particle colliders. There the new processes or particles would be seen directly if the energy would be sufficient to produce them. However, the effects (e.g. of a theory of quantum gravity) would become apparent at high energy scales (e.g. the Planck scale $m_P \approx 10^{19}$ GeV) that is by far out of reach for particle colliders.
As an alternative, a very sensitive probe can be constructed at low energies through precision measurements of quantities, that can be described by the SM. Then physics beyond the SM would become apparent indirectly through a deviation of the measured values from the SM predictions. The precision measurements that are the topic of this dissertation are of this kind:
Firstly, a small amount of the large effects of quantum gravity at the Planck scale should remain at low energies. This can be tested by looking for a violation of Lorentz invariance in the neutron sector. Secondly, new sources of CP violation would cause permanent EDMs of particles that are many orders of magnitude larger than the EDMs predicted by the SM. Therefore, experiments that put limits on EDMs can rule out (or at least narrow down) such models, or if they detect one will have an unambiguous evidence of new physics. Historically, the stringent limit on the neutron EDM has ruled out more speculative models than any other single experimental approach in particle physics. EDM precision measurements in various systems with different sensitivities will continue to constrain proposed models of physics beyond the SM. The various searches for CP violation are a good example of how low- and high-energy experiments are complementary to each other.
In Fig. 1.8, the different theoretical motivations for the experiments that are performed with this ^{3}He-^{129}Xe comagnetometer (including the search for a spin-depended short-range force mediated by the axion, that is not a focus of this dissertation) are sketched, showing the huge variety of fundamental questions that can be addressed.

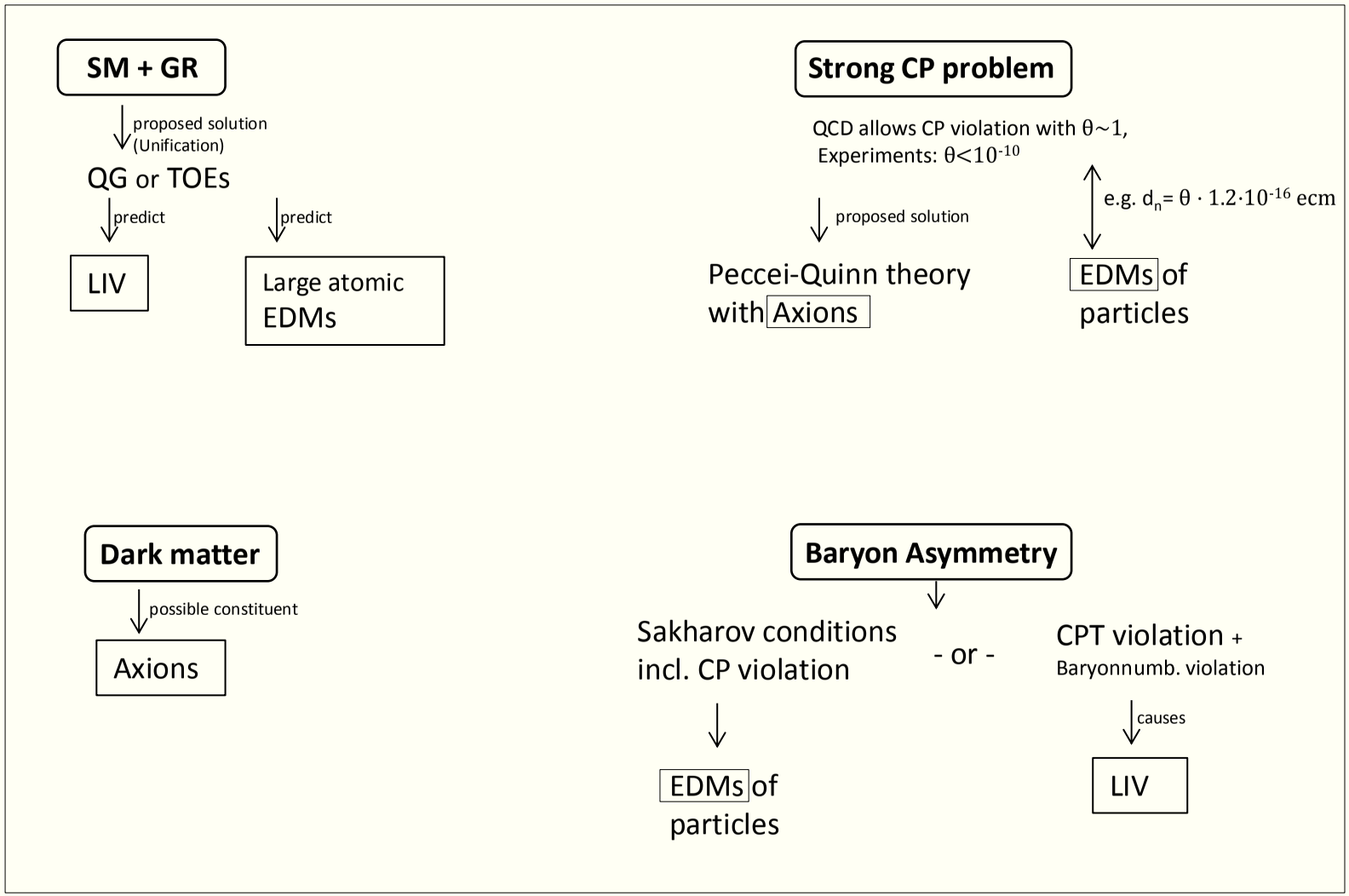

Figure 1.8: Overview of fundamental problems (Unification of the SM and GR, the strong CP problem, the nature of dark matter, and the origin of the baryon asymmetry) and the connections to measurements with the ^{3}He-^{129}Xe comagnetometer (Lorentz Invariance Violation (LIV), ^{129}Xe-EDM, and the search for a force mediated by Axions).

2 The ^{3}He-^{129}Xe Comagnetometer

In this chapter, the common basic set-up and the principle of measurement for the experiments putting limits on i) Lorentz invariance violation, ii) the electric dipole moment of ^{129}Xe, and iii) the Axion mass and coupling strength will be presented. Methods and experimental techniques, that are specialized or unique for a certain experiment, are described in the following chapters with a detailed description of the experiment putting limits on Lorentz invariance violation in Chapter 3, and with a detailed description of the ^{129}Xe-EDM experiment in Chapter 4. The measurements concerning the axion are described in [41, 42].
Finally, a discussion of deterministic phase shifts and systematic effects, that affect all measurements performed with the ^{3}He-^{129}Xe comagnetometer, will be given at the end of this chapter.

2.1 Theory of Operation

2.1.1 Spins in a Magnetic Field

Microscopic description

The energy of a magnetic moment $\boldsymbol{\mu}$ in a magnetic field $\boldsymbol{B_0}$ is given by

$$E = -\boldsymbol{\mu} \cdot \boldsymbol{B_0} \ . \tag{2.1}$$

The corresponding Hamiltonian of a particle with spin $\boldsymbol{\sigma}$ (associated with a magnetic moment $\boldsymbol{\mu} = \gamma\boldsymbol{\sigma}$) has the form

$$\begin{aligned} H &= -\boldsymbol{\mu} \cdot \boldsymbol{B_0} \\ &= -\gamma\hat{\boldsymbol{\sigma}} \cdot \boldsymbol{B_0} \end{aligned} \tag{2.2}$$

with the gyromagnetic ratio γ.
In the following paragraph, only spin $\frac{1}{2}$ particles are considered.
The components of the spin operator are defined by the Pauli matrices:

$$\hat{\boldsymbol{\sigma}} = \frac{\hbar}{2}\left[\begin{pmatrix} 0 & 1 \\ 1 & 0 \end{pmatrix}, \begin{pmatrix} 0 & -i \\ i & 0 \end{pmatrix}, \begin{pmatrix} 1 & 0 \\ 0 & -1 \end{pmatrix}\right] \ . \tag{2.3}$$

In the energy spectrum, one finds the well-known Zeemann splitting

$$\Delta E = E_{+\frac{1}{2}} - E_{-\frac{1}{2}} = \gamma\hbar B_0 \tag{2.4}$$

with the corresponding transition frequency, the Larmor frequency

$$\omega_L = \gamma B_0 \ . \tag{2.5}$$

To calculate the expectation value of a magnetic moment as a function of time $\langle \boldsymbol{\mu}(t) \rangle$, one has to solve the Schrödinger equation with the Hamiltonian given in Eq. (2.2). One finds that the expectation value follows the classical Euler's equation of rigid bodies:

$$\frac{d\langle \boldsymbol{\mu}(t) \rangle}{dt} = \gamma \langle \boldsymbol{\mu}(t) \rangle \times \boldsymbol{B}(t) \quad . \tag{2.6}$$

Macroscopic description and Bloch equation

For a large number N of spins (associated with microscopic magnetic moments) in a macroscopic sample with volume V, the magnetization $\boldsymbol{M}$ is defined by

$$\boldsymbol{M} = \frac{N}{V} \langle \boldsymbol{\mu} \rangle \tag{2.7}$$

with the ensemble average of the magnetic moments $\langle \boldsymbol{\mu} \rangle$. If one interprets the triangular brackets $\langle \cdot \rangle$ in Eq. (2.6) now as the ensemble average, the coherent motion of the spins in a magnetic field can be described with the same relation. Strictly speaking, the expectation value of the total magnetization and the expectation value of a single microscopic magnetic moment are only equal if the spins do not interact with each other. In experiments, one usually measures the result of a large number of spins simultaneously with the ensemble expectation value corresponding to the macroscopic magnetization. Finally, this leads to the Bloch equations describing the time evolution of the macroscopic magnetization which again has the form of the classical expression:

$$\frac{d\boldsymbol{M}(t)}{dt} = \gamma \boldsymbol{M}(t) \times \boldsymbol{B}(t) \quad . \tag{2.8}$$

The solution for a constant magnetic field in the z direction $\boldsymbol{B} = (0, 0, B_z)$ and a perpendicular magnetization $\boldsymbol{M}(t = 0) = (M, 0, 0)$ gives the classical precession of $\boldsymbol{M}$ around the direction of the magnetic field:

$$\boldsymbol{M}(t) = (M \cdot \cos(\omega_L \cdot t), M \cdot \sin(\omega_L \cdot t), 0) \tag{2.9}$$

with the Larmor frequency (Eq. (2.5)) as precession frequency: $\omega_L = \gamma B_z$.
Due to several relaxation processes, the transverse magnetization decays with a characteristic time constant T_2^*, while the longitudinal magnetization tends to reach the thermal equilibrium value $M_{z,\mathrm{equ}}$ with a characteristic time constant T_1. The origin of these relaxation mechanisms is described in Section 2.3.
To include these effects, one has to modify the Bloch equation:

$$\frac{d\boldsymbol{M}(t)}{dt} = \gamma \boldsymbol{M}(t) \times \boldsymbol{B}(t) + \begin{pmatrix} -M_x/T_2^* \\ -M_y/T_2^* \\ (M_{z,\mathrm{equ}} - M_z)/T_1 \end{pmatrix} \quad . \tag{2.10}$$

2.1.2 Additional Couplings Indicating New Physics

In the case of an additional coupling H_1 to the spins that is of a non-magnetic type, the Hamilton operator is given by:

$$H = -\gamma \hat{\boldsymbol{\sigma}} \cdot \boldsymbol{B_0} + H_1 \quad . \tag{2.11}$$

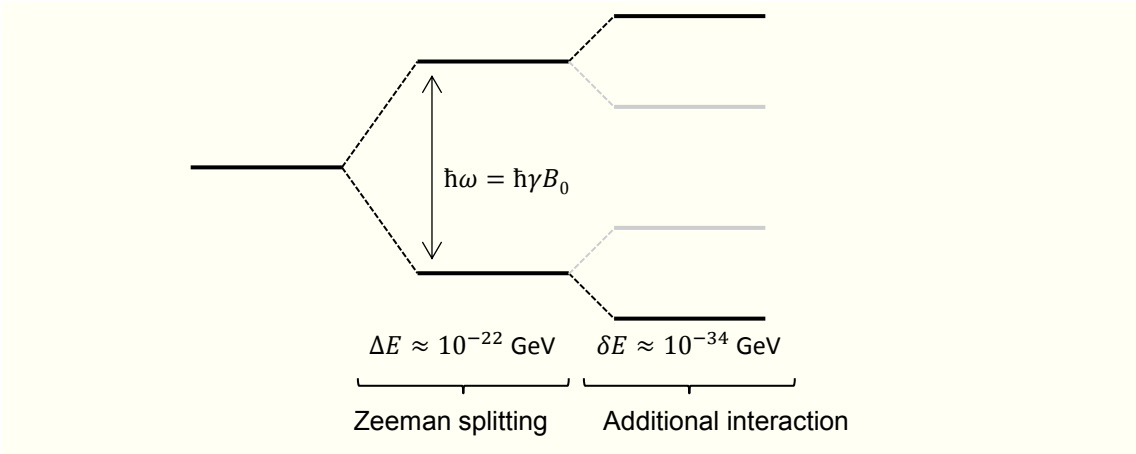

Figure 2.1: Schematic view of the energy levels of a spin $\frac{1}{2}$ particle in a magnetic field. For ^{3}He and ^{129}Xe and for a magnetic field of about 1 μT the Zeeman splitting is in the range of $\Delta E = \gamma\hbar B_0 \approx 10^{-22}$ GeV. The corresponding transition or precession frequency is about 10 Hz. The current sensitivity to additional shifts of the energy levels of the comagnetometer is 10^{-34} GeV.

This gives rise to an additional shift in the energy levels (see Fig. 2.1) with a corresponding shift $\delta\omega_1$ in the transition frequency.
Three different types of coupling are currently investigated with the ^{3}He-^{129}Xe comagnetometer:
1) For the Lorentz invariance violating coupling of the electron, proton, or neutron spin ($w = e, p, n$) to a hypothetical background field $\tilde{\boldsymbol{b}}^{\boldsymbol{w}}$, as described by the minimal Standard Model Extension in Chapter 1 (page 12 and the following pages), this is:

$$H_1 = H_{\mathrm{LV}} = -\tilde{\boldsymbol{b}}^{\boldsymbol{w}} \cdot \boldsymbol{\sigma}^{\boldsymbol{w}} \tag{2.12}$$

with the corresponding frequency shift

$$\delta\omega_{1,\mathrm{LV}} = \frac{2}{\hbar}\tilde{\boldsymbol{b}}^{\boldsymbol{w}} \cdot \boldsymbol{\sigma}^{\boldsymbol{w}} \ . \tag{2.13}$$

2) For a permanent electric dipole moment $\boldsymbol{d}$ in an electric field $\boldsymbol{E}$, as described in Chapter 1 (page 18 and following pages), this is:

$$H_1 = H_{\mathrm{EDM}} = -\boldsymbol{d} \cdot \boldsymbol{E} \ . \tag{2.14}$$

If the magnetic guiding field defining the quantization axis is aligned along the z-axis (the EDM is always parallel or anti-parallel to the spin):

$$H_{\mathrm{EDM}} = -d \cdot E_z \tag{2.15}$$

with the corresponding frequency shift

$$\delta\omega_{1,\mathrm{EDM}} = \frac{2}{\hbar} d \cdot E_z \ . \tag{2.16}$$

3) For a coupling induced by the axion, this is:

$$H_1 = H_{\text{Axion}} = V_\Sigma \tag{2.17}$$

with the corresponding frequency shift

$$\delta\omega_{1,\text{Axion}} = \frac{2}{\hbar} V_\Sigma \ . \tag{2.18}$$

The potential V_Σ is the integral of the axion-mediated spin-dependent short-range potential $V_{sp}(r)$ over the volume of the massive unpolarized sample, averaged over the volume of the polarized spin sample (details in [41, 42]).

2.1.3 Comagnetometry

In principle, this additional small energy shift resulting in a frequency shift $\delta\omega_1$ can be measured by a single spin species, for example using nuclear spin polarized ^{3}He. A macroscopic sample of polarized ^{3}He can be brought into a magnetic guiding field, which is perpendicular to the magnetization. The magnetization would precess around the direction of the magnetic guiding field with the Larmor frequency $\omega_L = \gamma B + \delta\omega_1$ according to Eq. (2.9). A modulation of the additional coupling could lead to a measurable variation in the precession frequency.
However, small drifts of the magnetic field would immediately mask such an additional shift in the Larmor frequency. Under realistic conditions, the magnetic field can be stabilized on the 10^{-6} level at best (see Fig. 3.6 on page 67). The absolute fluctuation or drift of the magnetic guiding field over the period of a single measurement run is in the order of $\delta B_0 \approx 10^{-6} \cdot 400$ nT $= 40$ pT. The energy resolution would then be limited by $\delta\Delta E = \gamma_{He} \cdot \hbar \cdot \delta B_0 \approx 10^{-26}$ GeV.
To become insensitive to fluctuations and drifts of the magnetic field, the principle of comagnetometry is used: Two different spin species are located in the same volume. In our case, this is nuclear spin polarized ^{3}He and ^{129}Xe gas contained in a glass cell. The mean magnetic field is the same for both spin species.
The weighted difference of the Larmor frequencies of the two spin species is defined by

$$\Delta\omega = \omega_{He} - \frac{\gamma_{He}}{\gamma_{Xe}} \cdot \omega_{Xe} \ . \tag{2.19}$$

In the case of a pure magnetic interaction of the spins with the magnetic guiding field like in Eq. (2.1), this is:

$$\begin{aligned} \Delta\omega &= \omega_{He} - \frac{\gamma_{He}}{\gamma_{Xe}} \cdot \omega_{Xe} \\ &= \gamma_{He} \cdot B_0 - \frac{\gamma_{He}}{\gamma_{Xe}} \cdot \gamma_{Xe} \cdot B_0 \\ &= 0 \ . \end{aligned} \tag{2.20}$$

The weighted frequency difference is independent of the strength of the magnetic guiding field. However, in general, additional interactions do not drop out:

$$\Delta\omega = \delta\omega_{1,He} - \frac{\gamma_{He}}{\gamma_{Xe}} \cdot \delta\omega_{1,Xe} \ . \tag{2.21}$$

Therefore, the weighted frequency difference is the appropriate observable to trace tiny frequency shifts stemming from non-magnetic interactions.
Alternatively, one can consider the integral over time, the weighted phase difference

$$\Delta\Phi = \Phi_{He} - \frac{\gamma_{He}}{\gamma_{Xe}} \cdot \Phi_{Xe} \ , \tag{2.22}$$

that is expected to be constant if there are no additional effects.

2.2 Polarization of ^{3}He and ^{129}Xe

The population numbers N_+ and N_- of the Zeemann states $+\frac{1}{2}$ and $-\frac{1}{2}$ with energies $E_{+\frac{1}{2}}$ and $E_{-\frac{1}{2}}$ and $\Delta E = E_{+\frac{1}{2}} - E_{-\frac{1}{2}} = \gamma\hbar B_0$ are given by the Boltzmann distribution

$$\frac{N_-}{N_+} = e^{-\frac{\Delta E}{kT}} \tag{2.23}$$

if the ensemble is in thermal equilibrium at temperature T.
As γ_{He} and γ_{Xe} are both negative, the $+\frac{1}{2}$ state has a higher energy for both nuclei. The corresponding polarization P is defined by

$$P = \frac{N_- - N_+}{N_- + N_+} \ . \tag{2.24}$$

In thermal equilibrium, this is

$$P = \frac{N_- - N_+}{N_- + N_+} = \frac{e^{-\frac{\Delta E}{kT}} - 1}{e^{-\frac{\Delta E}{kT}} + 1} = \tanh\left(-\frac{\Delta E}{2kT}\right) = \tanh\left(-\frac{\gamma\hbar B_0}{2kT}\right) \ . \tag{2.25}$$

For typical Nuclear Magnetic Resonance (NMR) applications, like Magnetic Resonance Imaging or Spectroscopy with high magnetic guiding fields (≈ 1 T) at room temperature, the polarization is in the order of $P \approx 4 \cdot 10^{-6}$. The density of spins in these kinds of measurements is high enough to generate a sufficient signal strength.
However, the polarization of ^{3}He and ^{129}Xe in thermal equilibrium at room temperature and a typical strength of the magnetic guiding field $B_0 \approx 400$ nT is only $P \approx 10^{-12}$. Furthermore, the density of spins in the sample cells is much lower, as gases with partial pressures in the order of mbar are used. Hence, the signal strength would be immeasurably low.
The polarization can be increased by many orders of magnitude by means of optical pumping (hyperpolarization) which will be presented in the following sections. [86–88]

2.2.1 Metastability Exchange Optical Pumping of ^{3}He

In the set-up at the Institut für Physik at the University of Mainz, ^{3}He can be polarized by Metastability Exchange Optical Pumping (MEOP) [86]. This process is very efficient and polarizations of $P \approx 90\%$ can be reached.
At a pressure of about 1 mbar and a constant homogeneous magnetic field of about 1 mT, a weak gas discharge excites the ^{3}He atoms from the ground state (1^1S_0) into the metastable 2^3S_1 state. Transitions from this metastable triplet state to the singlet ground state are forbidden due to angular momentum conservation. However,

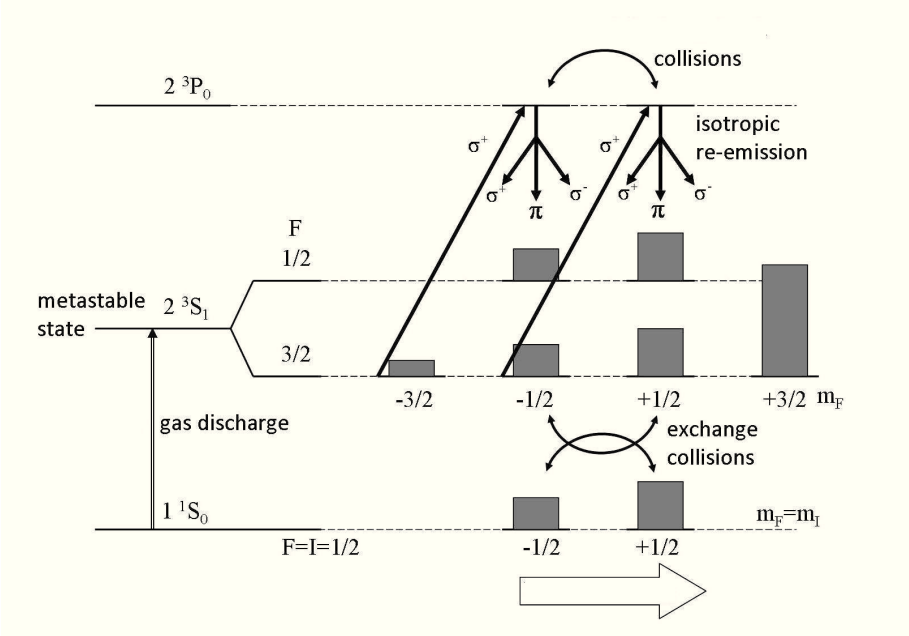

Figure 2.2: Metastability exchange optical pumping of ^{3}He. Source: [39]

de-excitation to the ground state can arise due to collisions of the ^{3}He atoms with the glass wall of the pumping cell. Thus, the lifetime of the 2^3S_1 state is about 1 ms.
The energy levels and transitions of ^{3}He, which are described in the following explanation, are illustrated in Fig. 2.2.
The magnetic field causes a splitting of the hyperfine levels with $F = \frac{1}{2}; \frac{3}{2}$ into Zeeman levels with the quantum number m_F. σ^+ photons at $\lambda = 1083.03$ nm (right-circularly polarized laser light) induce the transition from 2^3S_1 to 2^3P_0 with $\Delta m_F = +1$. The angular momentum of the absorbed photons is transfered to the ^{3}He atoms. The 2^3P_0 state has a lifetime of $\tau \approx 10^{-7}$ s. This is long enough so that atomic collisions lead to radiation-less transitions into the other 2^3P levels ($2^3P_{1,2}$). This process is called collisional mixing. Since the $2^3P_{0,1,2}$ levels are (almost) equally occupied, de-excitation happens isotropically into the Zeeman levels of the 2^3S_1 state. Consequently, unlike in the excitation process, there is no net angular momentum transfer during the de-excitation process. By repeated absorption and spontaneous reemission, the population numbers are redistributed towards increasing quantum number m_F, which leads to a polarization of the electron spin of atoms in the 2^3S_1 state.
The electronic spin and the nuclear spin are coupled via the hyperfine interaction. Thus, the nuclear spin of the ^{3}He atom (that is still in the metastable state) is also polarized. The nuclear polarized atoms collide with unpolarized atoms in the ground state 1^1S_0. Some of these collisions lead to an exchange of the excitation energy between the colliding atoms, while the nuclear spins stay unchanged. Consequently, this leads to polarized ^{3}He atoms in the ground state.
A complete description of MEOP of ^{3}He including kinetic models of the underlying processes and a detailed description of the set-up can be found in Ref. [86].

2.2.2 Spin Exchange Optical Pumping of ^{129}Xe

^{129}Xe cannot be directly polarized via MEOP. One has to use Spin Exchange Optical Pumping (SEOP). In this method the electron spins of alkali atoms (typically Rb) are polarized by optical pumping. The electron polarization of the alkali atoms is then transfered to the ^{129}Xe nuclei. This transfer happens either during binary collisions or during the relatively long lifetime of van-der-Waals molecules. In both cases, it is the nuclear electron spin-exchange interaction that couples the nuclear spin $\boldsymbol{I}$ of the ^{129}Xe atom to the electron spin $\boldsymbol{\sigma}$ of the alkali atom:

$$V = \alpha \boldsymbol{I} \cdot \boldsymbol{\sigma} \tag{2.26}$$

with the coupling constant α that depends on the spatial distance of the alkali and the ^{129}Xe atom.
The polarized gas for the experiments in Chapter 3 has been produced at the *Physikalisch-Technische Bundesanstalt* in Berlin. High polarizations of $P \approx 40\%$ can be reached. A detailed description of this set-up and general information on SEOP can be found in [88].

2.3 Mechanisms of Relaxation

The Modified Bloch equation in Eq. (2.10) includes effects of relaxation with the phenomenological time constants T_1 for longitudinal relaxation and T_2^* for transverse relaxation. The different underlying microscopical mechanisms leading to relaxation are described in the following paragraphs [75].

2.3.1 Longitudinal Relaxation

As described above, the equilibrium polarization at room temperature and small magnetic fields in the order of 1 μT is unfavorably low which makes the use of nuclear hyperpolarization necessary. The polarization in the order of $P \approx 1$ corresponds to a very low temperature of the nuclear spin system. Thus the system composed of the nuclear spins and the environment at room temperature $T_{env} \approx 300$ K is far out of thermal equilibrium. Subsequently there will be a heat flow $\frac{dQ}{dt} \propto (T_{env} - T_s)$ from the environment to the spin system until thermal equilibrium is reached. This results in an exponential decay of the nuclear polarization (in this case the equilibrium polarization $P \approx 10^{-12}$ is negligible):

$$P = P_0 \cdot e^{-t/T_1} \tag{2.27}$$

with the longitudinal relaxation time T_1. $\frac{1}{T_1}$ is proportional to the thermal conductivity between the environment and the spin system. This energy transfer leading to thermal equilibrium is usually referred to as "spin-lattice relaxation" in condensed matter Nuclear Magnetic Resonance (with the environment being the "lattice").
In gases, different mechanisms contribute to this thermal conductivity:

$$\frac{1}{T_1} = \frac{1}{T_{1,\text{grad}}} + \frac{1}{T_{1,\text{wall}}} + \frac{1}{T_{1,\text{bin}}} + \frac{1}{T_{1,\text{vdW}}} \quad . \tag{2.28}$$

The different contributions have a common principle: the interaction of the spins with the environment is based on magnetic interactions that cause spin flips. The individual mechanisms are explained in the following paragraphs:

Gradient relaxation

The contribution associated with $T_{1,\mathrm{grad}}$ is generated by gradients of the magnetic guiding field. The nuclear polarized atoms are usually in the gas phase and contained in a glass cell. The gas atoms move randomly around the cell. Due to the inhomogeneities of the magnetic field, the strength of the magnetic field at the position of an individual gas atoms varies with time. The spectral density of this randomly fluctuating magnetic field contains components around the Larmor frequency ω_L and will cause spin flips, and thereby lower the polarization. The exact description of this mechanism can be found in [75, 76]. In [77] an analytical description for the gradient relaxation in a spherical volume with radius R was derived. For the "regime of motional narrowing" (or the "low pressure regime") with low pressures and low magnetic fields the result can be simplified to:

$$\frac{1}{T_{1,\mathrm{grad}}} \approx \frac{8R^4\gamma^2}{175D}\left(|\boldsymbol{\nabla}B_y|^2 + |\boldsymbol{\nabla}B_z|^2\right) \tag{2.29}$$

with the diffusion coefficient of the gas D.
For the "high pressure regime", i.e. for high magnetic fields and high pressures, the gradient relaxation is given by

$$\frac{1}{T_{1,\mathrm{grad}}} \approx \frac{D}{B^2}\left(|\boldsymbol{\nabla}B_y|^2 + |\boldsymbol{\nabla}B_z|^2\right) \quad . \tag{2.30}$$

During the production and transport of the polarized gas, the gradient relaxation is in the high pressure regime, and consequently Eq. (2.30) applies (during transport: the pressure is about 3 bar and the magnitude of the magnetic guiding field is in the order of $B_0 = 800\ \mu$T).
In contrast, during the measurements, Eq. (2.29) applies (motional narrowing regime) with pressures in the order of mbar and $B_0 \approx 400$ nT.

Wall relaxation

The nuclear polarized gas atoms are usually contained in a cell made of glass. Gas atoms collide with the surface of the cell, can be adsorbed to the surface or even diffuse into the bulk of the glass. Dipolar coupling or Fermi-contact interaction with ferromagnetic or paramagnetic impurities (iron particles, dangling bonds) on the surface or inside the bulk material cause spin flips and subsequently depolarization [81–83].
The rate of the wall relaxation is proportional to the ratio of the surface A to the volume V of the cell:

$$\frac{1}{T_{1,\mathrm{wall}}} = \frac{1}{\eta}\frac{A}{V} \tag{2.31}$$

with the constant η describing the relaxation properties of the wall material (e.g. ferro- and paramagnetic impurities).
To maximize $T_{1,\mathrm{wall}}$ one uses spherical glass cells (whenever possible) with a radius R.

Then $T_{1,\text{wall}} = \eta R$. The wall material is an alumosilicate glass (GE-180)[1] that strongly suppresses the diffusion of gas atoms into the bulk material and contains very little ferro- and paramagnetic impurities.

Binary and van-der-Waals relaxation

In binary collisions of the gas atoms, short-lived molecules (^{3}He-^{3}He, ^{129}Xe-^{129}Xe or ^{129}Xe-^{3}He) can be formed, either bound by covalent bonds or van-der-Waals bonds. In addition to the translational degrees of freedom, these molecules have rotational and vibrational degrees of freedom. The nuclear spins couple to the rotational angular momentum of the molecule, which transfers part of the nuclear spin polarization to orbital angular momentum. The formation rate of such molecules with covalent bonds depends on the partial pressure p and on the temperature T. In [84] and [85] the relaxation times due to binary collisions in ^{3}He and ^{129}Xe are given:

$$\begin{aligned} T_{1,\text{bin}}^{He} &\approx 754\ \text{h} \cdot \frac{p_0}{p_{He}} \cdot \frac{T}{T_0} \quad , \\ T_{1,\text{bin}}^{Xe} &\approx 56\ \text{h} \cdot \frac{p_0}{p_{Xe}} \cdot \frac{T}{T_0} \end{aligned} \tag{2.32}$$

with $p_0 = 1013$ mbar and $T_0 = 273.15$ K. The relaxation due to the formation of ^{129}Xe-^{3}He molecules is negligible.
Additionally, xenon forms van-der-Waals molecules with relatively long lifetimes, and thus, large contributions to relaxation. The lifetime of van-der-Waals molecules can be drastically reduced by buffer gases (N_2 or SF_6, for example). Experimentally, one finds that the relaxation time due to van-der-Waals molecules can be estimated by

$$T_{1,\text{vdW}}^{\text{Xe}} = 4.1\ \text{h} \cdot \left(1 + 1.05 \frac{p_N}{p_{Xe}}\right) \tag{2.33}$$

with the partial pressures of the buffer gas p_N and xenon p_{Xe}. Thus, T_1 is drastically increased by adding a buffer gas to the gas mixture, in this case N_2 with $p_N = 25$ mbar, while $p_{Xe} = 5$ mbar.

2.3.2 Transverse Relaxation

The component of the magnetization that is perpendicular to the magnetic guiding field, the transverse magnetization, precesses with the Larmor frequency. The decay of the measurable macroscopic magnetization is an exponential decay with time constant T_2. The well-known spin-spin relaxation mechanisms (i.e. random fluctuations of the local magnetic field) from NMR experiments in solids and liquids are unimportant for thin gases. Thus:

$$\frac{1}{T_2} = \frac{1}{T_{1,\text{wall}}} + \frac{1}{T_{1,\text{vdW}}} \tag{2.34}$$

$$\approx \frac{1}{T_1} \tag{2.35}$$

[1] GE-180 is a product of "General Electric". It consists of SiO_2 (60%), BaO (18%), Al_2O_3 (14%) and CaO (7%).

However, the dephasing of the spins in an ensemble leads to an effective reduction of the macroscopic magnetization. The presence of a magnetic field gradient in a sample cell causes an increased transverse relaxation rate. The origin of this relaxation mechanism is the loss of phase coherence of the atoms due to the fluctuating magnetic field which is seen by the atoms as they diffuse throughout the cell. Based on the Redfield theory of relaxation due to randomly fluctuating magnetic fields [76], analytical expressions can be derived for the transverse relaxation rate for spherical and cylindrical sample cells [77, 79]. A simplified expression, that is valid in the regime of motional narrowing (low pressure) and low magnetic fields for a spherical sample cell of radius R, is[2]

$$\begin{aligned} \frac{1}{T_2^*} &= \frac{1}{T_1} + \frac{1}{T_{2,\text{field}}} \\ &\approx \frac{1}{T_1} + \frac{4R^4\gamma^2}{175D}\left(2|\boldsymbol{\nabla}B_x|^2 + |\boldsymbol{\nabla}B_y|^2 + |\boldsymbol{\nabla}B_z|^2\right) \end{aligned} \tag{2.36}$$

D is the diffusion coefficient of the gas ($D_{He} = 1880$ cm^2/s and $D_{Xe} = 58$ cm^2/s at $p_0 = 1$ mbar and $T_{env} = 300$ K [80]).
The diffusion coefficient D is anti-proportional to the pressure:

$$D(p) = \frac{D_0 \cdot p_0}{p} \ . \tag{2.37}$$

Thus, large transverse relaxation times in the order of several hours can only be reached with thin gases ($p \propto$ mbar) and homogeneous magnetic fields with gradients in the order of pT/cm.

Optimization of the transverse relaxation time

The transverse relaxation time determines the measurement time T of a single measurement run:

$$T \approx 3 \cdot T_2^* \ . \tag{2.38}$$

After that time the signal to noise ratio has decreased to about 5% of its initial value. Since typically $T^*_{2,Xe} < T^*_{2,He}$ (see Tab. 2.1) a maximization of $T^*_{2,Xe}$ has to be performed. The different relaxation mechanisms (especially wall and gradient relaxation) have to be considered and a compromise has to be found as wall relaxation decreases with larger measurement cells, while gradient relaxation increases. A method to reach small gradients inside the mu-metal shielding is described in Chapter 3 on page 74.
Typical optimized values for the relaxation time constants can be found in Tab. 2.1.

2.4 The Basic Set-Up

The basic set-up of the ^{3}He-^{129}Xe comagnetometer consists of the measurement cell filled with polarized ^{3}He and ^{129}Xe gas, as well as a buffer gas (nitrogen or SF_6), that is brought into a magnetically shielded room. A coil system with adjustable current sources generates a magnetic guiding field. A SQUID system then detects the field of the precessing magnetization of the polarized gases.
The several components of the comagnetometer will be described in detail in the following sections.

[2] The longitudinal gradient relaxation in Eq. (2.29) is now included in the term describing $T_{2,\text{field}}$.

	$T_{1,\mathrm{vdW}}$	$T_{1,\mathrm{wall}}$	T_1	T_2^*
^{3}He	-	200 h	200 h	100 h
^{129}Xe	26 h	30 h	14 h	8.5 h

Table 2.1: Typical values of the relaxation times under optimized experimental conditions with spherical cells made of GE-180 glass (diameter 10 cm) and partial pressures of $p_{He} \approx 3$ mbar, $p_{Xe} \approx 5$ mbar and $p_{N_2} \approx 25$ mbar. The magnetic field gradients are in the range of 20 to 30 pT/cm.

2.4.1 Magnetic Shielding

Long transverse relaxation times in the order of several hours can only be reached with homogeneous magnetic fields with gradients in the order of pT/cm. In addition, a high-resolution measurement of frequencies demands a high signal-to-noise ratio (SNR). In this case, the amplitude spectral density at the ^{3}He and ^{129}Xe Larmor frequencies of the magnetic noise stemming from the environment and from the components within the experiment must be minimized. A detailed discussion of the influence of magnetic field gradients and noise on the achievable frequency resolution can be found in Chapter 3 on page 89.
The magnetic shielding that surrounds the experiment has two functions: minimizing field gradients and attenuating external magnetic noise.
The first stage of a typical shielding consists of active shielding to compensate the Earth's magnetic field. The currents through three large Helmholtz coil pairs are adjusted by a feed-back mechanism that cancels slow drifts of the Earth's magnetic field. Different layers of passive shielding follow, with a highly conductive Faraday cage made of aluminum to effectively suppress high frequency noise, and several layers of mu-metal, a material with a high magnetic permeability. Mu-metal is an alloy of nickel (77%), iron (16%), copper (5%) and smaller amounts of chromium and molybdenum. The relative permeability μ_r can reach values of up to 10^5, but this value strongly depends on the handling of this material, mechanical stress etc., and drops with higher magnetic fields (it saturates easily). Mu-metal offers an energetically preferred path for magnetic flux lines due to its high permeability, and thus a space surrounded by this material is effectively shielded from DC fields and low frequency environmental magnetic field noise.
To eliminate the remnant magnetic field of the shielding, e. g. imprinted magnetization by the Earth's magnetic field, it is necessary to degauss the individual mu-metal layers from time to time, after the shield has been opened, for example. The aim of the degaussing procedure is to reduce the residual magnetic field to the ideal value by random orientation of the magnetic domains. To do so, an oscillating ($f \approx 10$ Hz) current with a slowly decreasing amplitude flows through wires that are closely attached to and surround the mu-metal shielding. The resulting decreasing alternating magnetic field forces the magnetization of the material on a cyclic passage through the hysteresis loop from saturation into the almost demagnetized state which is a local state of minimum energy. Much effort has been put into the theoretical description and experimental optimization

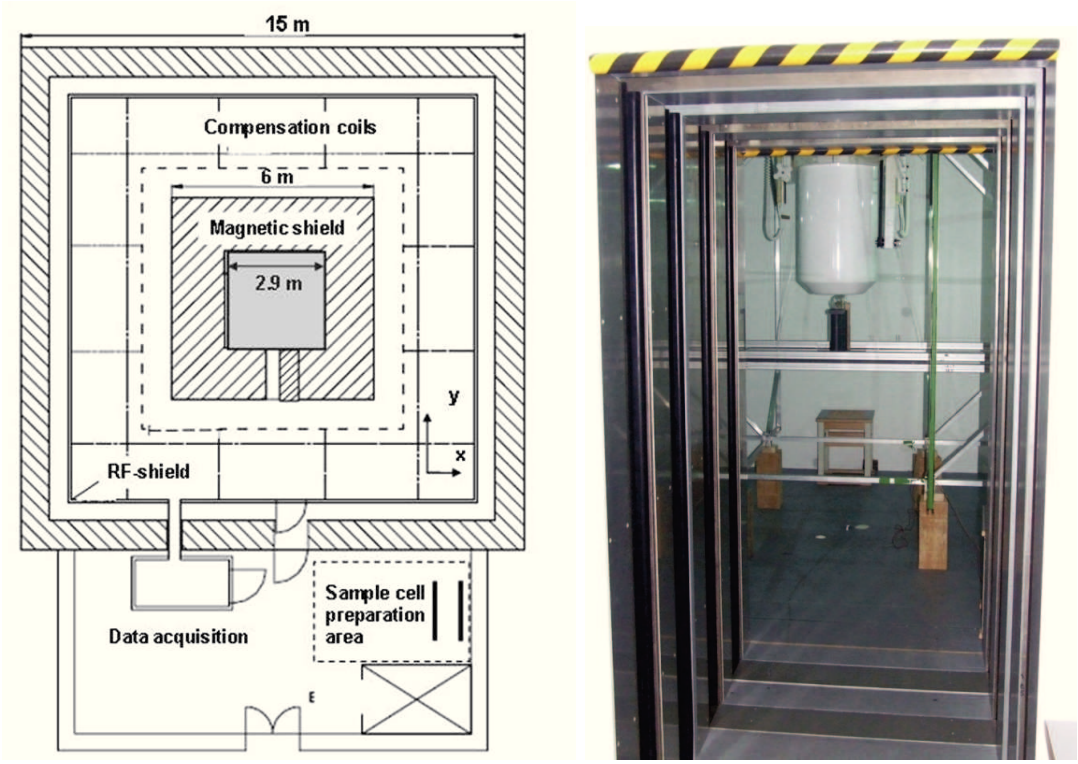

Figure 2.3: Left: A schematic top view of the Berlin Magnetically Shielded Room (BMSR-2) that is housed in a dedicated building at the Physikalisch-Technische Bundesanstalt. It is so far the best shielded room worldwide with shielding factors of 10^6 at 1 Hz and 10^9 at 10 Hz [90]. Right: View through the several doors leading through the mu-metal layers into the inner chamber with the prominent white cryostat housing the SQUID sensors and the Helmholtz coil pairs (green).

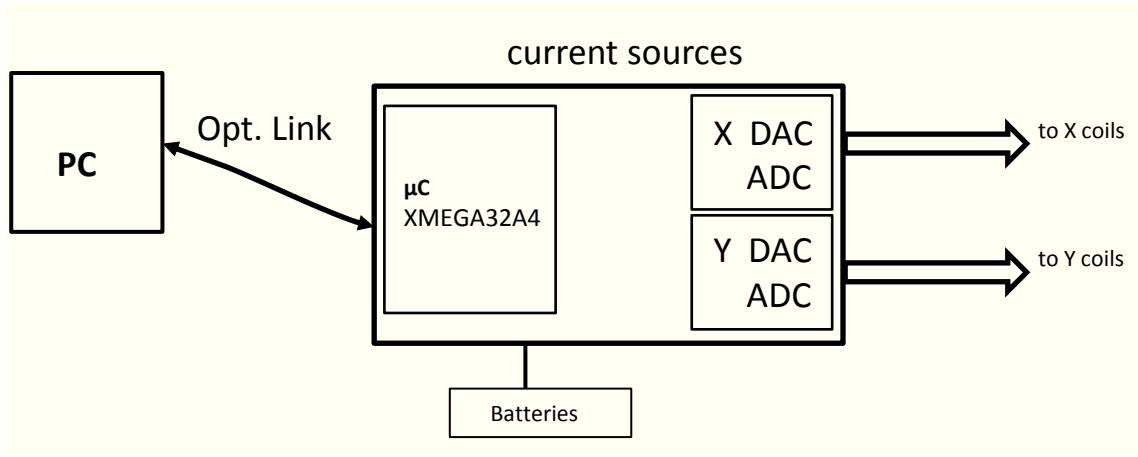

Figure 2.4: Block diagram of the high-precision low-noise dual current source. The current source is controlled from the outside via an optical link and it is powered by LiPo cells. A micro-controller is used for the communication via the optical link and to control the digital-to-analog converters (DACs).

of the degaussing process. An overview can be found for example in [89].
One of the most elaborate magnetically shielded rooms is the Berlin Magnetically Shielded Room (BMSR-2) of the Physikalisch-Technische Bundesanstalt (see Fig. 2.3) that was used for the Lorentz invariance violation measurements. With seven layers of mu-metal with a total thickness of 30 mm, an aluminum Faraday cage (10 mm), active shielding, and an additional HF-shield, the magnetic noise level inside is reduced to about 3 fT/$\sqrt{\text{Hz}}$ for frequencies of a few Hz (above about 1 Hz the noise spectrum becomes white) and the gradients reach a level of a few pT/cm at the center of the shielded room.

2.4.2 Coils and Current Sources

Inside the magnetically shielded room, a stable and homogeneous magnetic guiding field must be generated. In addition, it has to be adjustable to define different quantization axes of the spins and to tune the Larmor frequencies. The typical strength of the magnetic guiding field is $B_0 = 400$ nT. A homogeneous magnetic field can be generated by (square) Helmholtz coil pairs if there is enough space or by a cosine-coil in cylindrical shape for smaller volumes together with very stable and adjustable low-noise current sources.
New current sources for this purpose have been developed. The concept of the set-up is shown in Fig. 2.4. A schematic circuit diagram of the output stage can be found in Fig. A.8 in the appendix on p. 139. It has two independent channels, e.g. for two Helmholtz coil pairs perpendicular to each other. The output current is adjustable ($I = -50...50$ mA) with a resolution of $\Delta I = 100$ nA and a maximum frequency of $f = 1$ kHz. Any sequence of current steps, linear increase/decrease or sinusoidal currents with arbitrary phases and amplitudes can be programmed.

In order to avoid that noise from the environment is conducted into the shielded room, the current source is controlled from the outside via an optical link and it is powered by rechargeable batteries (LiPo cells). An ATMEL XMEGA32A4 micro-controller is used for the communication via the optical link and to control the digital-to-analog converters (DACs). Analog-to-digital converters (ADCs) measure the actual current through the coils as an additional feature. The crucial point for the stability and the noise of the current source is the output stage: The output voltage of the 20-bit DAC AD5791 from Analog Devices (noise spectral density $\approx 7.5\ \mathrm{nV}/\sqrt{\mathrm{Hz}}$)[3] is filtered, and then buffered by an AD8675 low-noise ($2.8\ \mathrm{nV}/\sqrt{\mathrm{Hz}}$) operational amplifier. Then the output current is driven by an AD797 operational amplifier ($0.9\ \mathrm{nV}/\sqrt{\mathrm{Hz}}$). Finally, the current through the load resistance (coil) causes a voltage drop over four sense resistors that is coupled back into a feed-back mechanism. The parallel circuit of several sense resistors was chosen to optimize for and strongly suppress temperature dependent drifts.
The expected output voltage noise of the combination of all active components in the circuit is $8\ \mathrm{nV}/\sqrt{\mathrm{Hz}}$. This value is higher, but comparable to the thermal noise of the coil with $R \approx 100\ \Omega$ that is described by the Johnson-Nyquist formula:

$$\sqrt{\overline{v^2}} \;=\; \sqrt{4k_B T R}\ , \tag{2.39}$$

where $\sqrt{\overline{v^2}}$ is the voltage noise amplitude spectral density ("RMS"), k_B is Boltzmann's constant and T the temperature of the resistor R. For room temperature and $R = 100\ \Omega$ (coils or sense resistor) this is: $1.3\ \mathrm{nV}/\sqrt{\mathrm{Hz}}$
Thus the overall voltage noise level is expected to be $8.2\ \mathrm{nV}/\sqrt{\mathrm{Hz}}$. This corresponds to an current noise of $82\ \mathrm{pA}/\sqrt{\mathrm{Hz}}$ through the coils and the resulting magnetic field noise is $1.6\ \mathrm{fT}/\sqrt{\mathrm{Hz}}$.
Linearity of the current source, as well as temperature and long term stability have been tested extensively and found to be better than needed. In Chapter 3 it will be shown that remaining drifts of the magnetic guiding field (40 pT per hour) are stemming from slow relaxation processes of the innermost mu-metal shielding.
The resulting magnetic field is a superposition of the field produced by the coils and the residual field of the inner mu-metal layer. By adjusting the direction of the magnetic guiding field one can find positions where the gradients of the two sources almost cancel each other. This procedure is described in detail in Chapter 3 on page 74. Gradients down to 20 pT/cm can be reached this way.

2.4.3 SQUIDs as Magnetic Flux Detectors

For the measurement of the precessing ^{3}He and ^{129}Xe magnetization, Superconducting QUantum Interference Devices (SQUIDs) are used. They are very sensitive magnetometers based on the Josephson effect and flux quantization. In order to reach a very low noise level (a few $\mathrm{fT}/\sqrt{\mathrm{Hz}}$), low-temperature DC-SQUID magnetometer systems are used. A DC-SQUID is made of of two Josephson junctions connected in parallel on a superconducting loop (see Fig. 2.5). The Josephson junction consists of two weakly coupled superconductors. The weak link is usually a thin insulating barrier (SIS type), but also a normal conducting layer (SNS type) is possible. The current transport through

[3] All noise level values in this paragraph are given for $f = 10$ Hz.

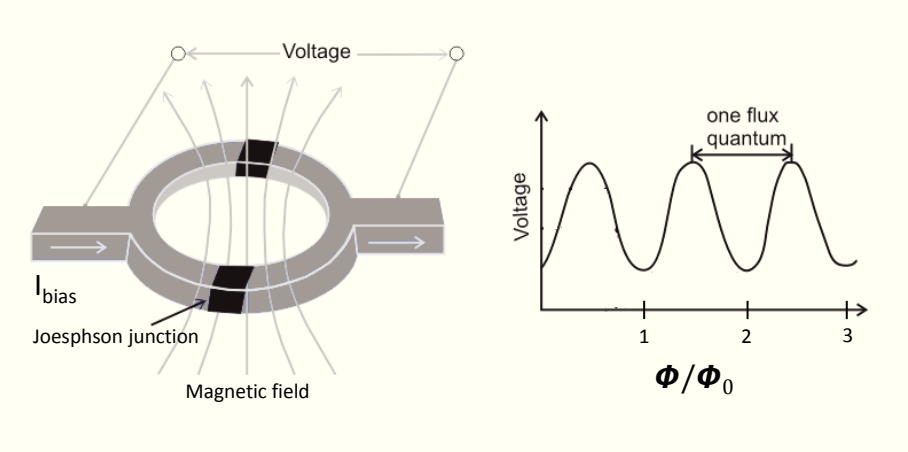

Figure 2.5: The principle of the DC SQUID with a constant bias current. The voltage drop depends periodically on the flux Φ that is enclosed by the superconducting loop.

the barrier occurs due to the tunneling of Cooper pairs. Usually the Josephson junctions are shunted by resistors and capacitors. The current-voltage characteristics of such junctions then are described very well by a linear model, the resistively and capacitively shunted junction model (RCSJ model) in most cases. A detailed description of the underlying principles is beyond the scope of this dissertation, but can be found for example in "The SQUID Handbook" [91, 92]. The important fact is that the DC-SQUID acts directly as a flux-to-voltage converter, which will be outlined very briefly here:
At zero magnetic flux, a current I_{bias} fed into the SQUID splits equally into the two branches ($I_1 = I_{\text{bias}}/2$ and $I_2 = I_{\text{bias}}/2$). If one increases the external magnetic field, a screening current I_s is induced that results in an asymmetric current in the two branches: $I_1 = I_{\text{bias}}/2 + I_s$ and $I_2 = I_{\text{bias}}/2 - I_s$, so that the magnetic flux through the SQUID is a multiple of the magnetic flux quantum $\Phi_0 = h/(2e)$. If the additional external flux is below $\Phi_0/2$ then I_s generates a magnetic field that exactly cancels the flux enclosed by the SQUID loop, otherwise it increases it to Φ_0. Similarly, for higher external magnetic fields the screening current pushes the SQUID flux to the nearest integer multiple of Φ_0. When an appropriate bias current I_{bias} is fed into the SQUID, a linear change in the magnetic flux causes a periodic change in the voltage across the junctions with the period of Φ_0. In the case of resistive shunts parallel to the Josephson junctions - removing the hysteresis and adding thermal noise - this modulation becomes smooth (see Fig. 2.5, right). Thus, the DC-SQUID in the bias current mode acts directly as a flux-to-voltage converter. To measure small changes $\delta\Phi$ in the applied flux, one usually chooses a bias current that maximizes the amplitude of the voltage modulation and the off-set flux, so that the applied flux is at the position $(2n+1)\Phi_0/4$ in order to maximize $|(\partial V/\partial \Phi_a)|$.
Usually the DC-SQUID is operated in a flux-locked feedback mode at this optimal working point in order to keep the maximal sensitivity and to linearize the response function. To do so, a magnetically coupled small feedback coil is placed near the SQUID that can

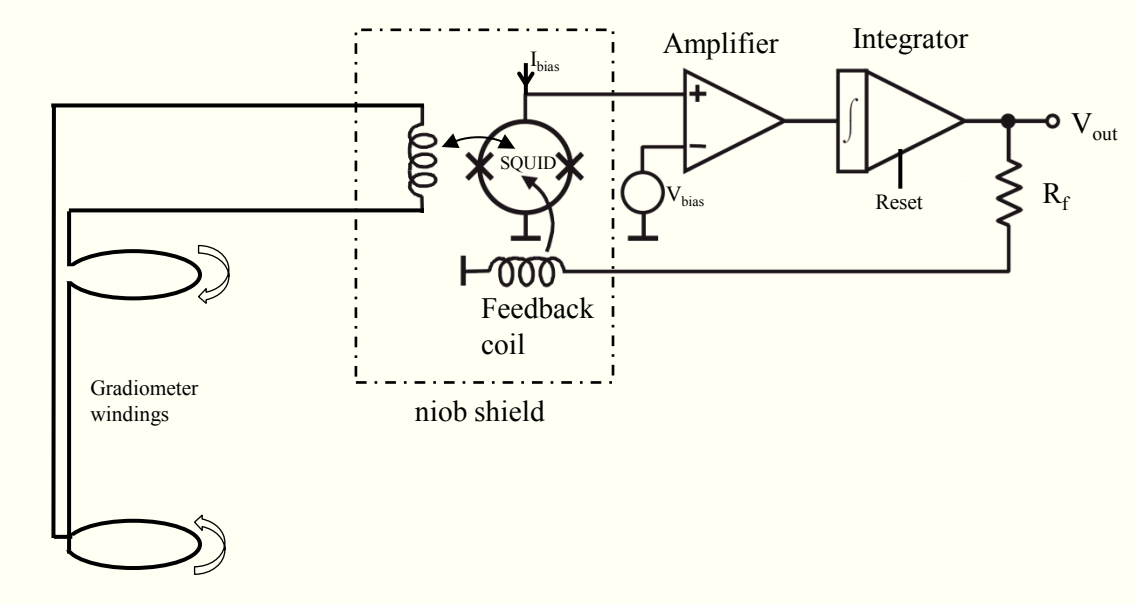

Figure 2.6: The basic principle of a Flux-Locked Loop (FLL) with an external pickup coil. The niob capsule and the components inside, as well as the niob wire forming the gradiometer loops on the left side, are at liquid helium temperature. The other components (amplifier, integrator, and the whole DAQ system is at room temperature. Changes in the external field cause a current in the pickup loop which generates a magnetic field at the SQUID position via the input coil. A deviation from the working point of the SQUID voltage is amplified, integrated and then a current is fed back into the coil via a feedback resistor R_f. The resulting change in the flux of the feedback loop also sets the current in the input coil and pickup loop back to zero. The voltage drop across the feedback resistor R_f is proportional to the flux difference of the lower and higher pickup loop. To form a magnetometer, one can use a single loop pickup coil (instead of the two pickup loops for gradiometers). When the SQUIDs are used as direct magnetic flux sensors (measuring the flux at the position of the SQUID) the niob capsule and the coils on the left side are removed.

generate an adjustable flux. A deviation from the working point of the SQUID voltage is amplified and integrated, and then a current is fed back into the coil via a feedback resistor R_f (see Fig. 2.6). Thus, external flux changes (e. g. the measurement signals) cause a proportional change in the feedback current. The voltage drop across the feedback resistor R_f can be read out, digitalized by ADCs and further processed. Such a set-up generates an extremely high system linearity (harmonic distortion down to about -120 dB at low frequencies). The dynamic range can be adjusted by changing the feedback resistor. A smaller resistor increases the dynamic range, but also increases the demands of the ADC in the data acquisition system with respect to resolution and noise, because the flux-to-output-voltage relation becomes less steep. Thus, a second method to increase the dynamic range is often used: The feedback range and the corresponding ADC input range are set to Φ_0. Then, when the flux exceeds this range, the integrator is reset, the working point of the flux-locked loop is shifted by Φ_0. The number of flux quanta is counted and together with the output voltage (ADC value) gives the total output of the data acquisition system.
In the set-up that has been described above, the SQUID acts directly as a magnetic flux sensor, e. g. it measures the flux at the SQUID position or the strength of the magnetic field perpendicular to the SQUID plane. A second method to measure magnetic fields uses SQUIDs as current detectors: An external pickup loop made of superconducting niob wire can be flux-transformer-coupled to the SQUID via an input coil (see Fig. 2.6). The SQUID is in a niob capsule shielding it from any external magnetic field. Changes in the external field cause a current in the pickup loop which generates a magnetic field at the SQUID position via the input coil. The feedback mechanism stays the same and the resulting change in the flux of the feedback loop also sets the current in the pickup loop (and input coil) back to zero. The big advantage of the pickup loop set-up, is the higher magnetic flux due to the larger area of several cm^2. Thus a signal with a fixed magnetic field strength results in a higher amplitude, while the internal SQUID noise stays the same, substantially improving the signal-to-noise ratio. Furthermore, wire-wound axial gradiometers can be constructed with the external pickup loop: Two loops with opposite winding orientations are placed on top of each other at a distance b, called baseline length. The resulting flux that is coupled into the SQUID via the input coil is proportional to the flux difference of the two loops. Thus, a homogeneous magnetic field (or field change) does not give a measurement signal. This principle can be used to strongly suppress noise (statistical noise from sources that a far away compared to the gradiometer baseline length, e. g. the current sources and coils or the mu-metal shielding) or common mode vibrations due to mechanical resonances (e. g. vibration of the dewar or the whole building). However, point-like signal sources next to the lower gradiometer loop, that have a typical dipole field distribution, are attenuated very little. For a gradiometer baseline length b and a distance between the lower loop and the source d the expected measurement signal is proportional to

$$S \propto \frac{1}{d^3} - \frac{1}{(d+b)^3} . \tag{2.40}$$

To give an example, for typical values $b = 7$ cm and $d = 7$ cm the measurement signal is reduced by 12.5 % compared to a single magnetometer at the position of the lower loop, whereas common mode noise is almost totally eliminated.

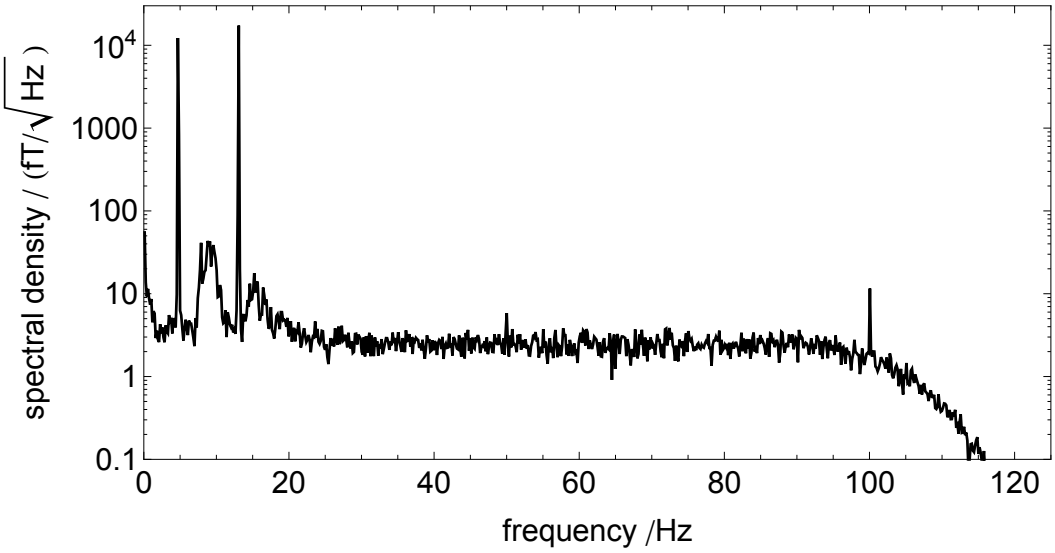

Figure 2.7: The typical spectrum (amplitude spectral density) of the measurement signal detected by a single SQUID magnetometer. The peaks at the ^{129}Xe (5 Hz) and ^{3}He (13 Hz) Larmor frequencies are prominent. The white noise level is about 3 fT/$\sqrt{\text{Hz}}$ for frequencies above 1 Hz. For lower frequencies the 1/f noise (flicker noise) is dominant. For frequencies above 100 Hz the anti-aliasing low pass filter roll-off can be seen (sampling frequency 250 Hz). The broader peaks around 10 Hz and 15 Hz are caused by mechanical vibrations of the building.

The first set-up method (using the SQUIDs directly as magnetic flux sensors) was used for Lorentz invariance measurements (Chapter 3) in a 304 channel magnetometer system designed for bio-magnetism measurements at the Physikalisch-Technische Bundesanstalt Berlin. The noise level of the whole set-up (including the internal SQUID noise and all external noise sources) during the measurements reached the 3 fT/$\sqrt{\text{Hz}}$ level at the relevant frequencies (see Fig. 2.7). For the ^{129}Xe EDM experiment, a system was designed and tested that uses the second method with external wire-wound magnetometers and gradiometers (Chapter 4).

Many more details concerning configuration and performance have to be considered (like constraints on inductances, magnetic coupling, manufacturing of the SQUIDs, selection of noise free materials, etc.) to construct SQUID systems that can be used as measurement devices. Much effort has been put into optimizing components (especially with respect to preamplifier noise) and measurement methods, e. g. flux modulation (switching periodically between two working points), additional positive feedback (resulting in a strongly asymmetric flux-voltage relation with a steeper working point), further amplification stages with series SQUID arrays, "Q-spoilers" to protect the SQUIDs from high currents, and much more that is beyond the scope of this dissertation. An detailed description can be found for example in "The SQUID Handbook" [91, 92].

Special care has to be taken during the construction of the dewar that houses the SQUIDs and in the selection of the materials for both the dewar and for the carriers on which the SQUIDs are mounted with respect to magnetic impurities. Magnetic materials (especially ferromagnetic materials) would lead to additional gradients and a worse noise level. The performance of the total experimental set-up (including the SQUID system, magnetic shielding, current sources and coils, the measurement cell and all the supportive structures) with respect to noise can be seen in Fig. 2.7.
To operate the SQUID system the usual cryogenic equipment is needed: for example, a device to refill liquid helium and a helium level meter.

2.4.4 Further Components

Besides the components that have been described, many more "supportive" structures are needed to perform measurements. Most of them have been developed, designed and constructed at the Institut für Physik at Mainz University in the group of W. Heil [39, 42, 86]:

- Transport vessel for polarized ^{3}He: The polarized ^{3}He is produced via MEOP at Mainz. Due to its large longitudinal relaxation time in GE-180 glass vessels ($T_1 \approx 300$ h at a pressure of a few bars), it can be transported by ordinary parcel services to the location where the experiment is performed. To do so, special transport and storage vessels have been constructed with permanent magnets that generate a magnetic guiding field stronger than the Earth's magnetic field. In that way, zero crossings of the total magnetic field can be avoided which would lead to a fast depolarization of the ^{3}He gas.

- Filling station: To prepare the measurement cell with the right mixture of gases (polarized ^{3}He and ^{129}Xe, and N_2) outside the magnetically shielded room, a place surrounded by a large pair of Helmholtz coils was set up. The homogeneous magnetic field generated by these coils is larger than the Earth's magnetic field, and thus, defines the quantization axis for the ^{3}He and ^{129}Xe spins. The whole filling system contains the storage vessels for ^{3}He, ^{129}Xe and N_2, the port for a vacuum pump, the port to connect the measurement cell, a pressure sensor, connections between these parts with different volumes (to adjust the pressure) and different sluice valves that allow to fill different gas quantities into the measurement cell. [42]

- Transport coil: In order to transport the measurement cell from the filling station into the magnetically shielded room under controlled magnetic conditions, a special transport coil was constructed. It consists of two solenoids of equal length $L = 60$ cm, but with different diameters. The smaller coil is placed inside the bigger coil. With the correct number of windings, one can cancel the magnetic moments of the two coils, so that the outside field falls off very steep, and the resulting field inside the inner coil is homogeneous. A special switch for turning on and off the transport coil smoothly ramps up and down the current through the coils with a time constant of about 7 s, so that the spins can follow adiabatically.

2.5 Deterministic Phase Shifts

In section 2.1.3 on page 32, the basic principle of comagnetometry was discussed. This principle is applied to become insensitive to fluctuations and drifts of the magnetic field. Two different spin species (nuclear spin polarized ^{3}He and ^{129}Xe atoms) are located in the same volume, so that the mean magnetic field is the same for both spin species. Then, the weighted difference of the two Larmor frequencies given by

$$\Delta\omega = \omega_{He} - \frac{\gamma_{He}}{\gamma_{Xe}} \cdot \omega_{Xe} \quad , \tag{2.41}$$

should vanish in the case of a pure magnetic interaction of the spins. In other words: The weighted frequency difference is independent of the strength (and drifts or variations) of the magnetic guiding field as the Zeeman term drops out. However, additional interactions, that are of non-magnetic type, do not drop out. Therefore, the weighted frequency difference is the appropriate observable to trace tiny frequency shifts stemming from non-magnetic interactions. Alternatively, one can consider the integral over time, the weighted phase difference

$$\Delta\Phi = \Phi_{He} - \frac{\gamma_{He}}{\gamma_{Xe}} \cdot \Phi_{Xe} \tag{2.42}$$

that is expected to be constant if there are no additional effects.
However, strictly speaking, this is no longer true, as there are several effects that lead to a deviation from a constant value for the weighted phase difference. Such effects may have different time dependencies. These deterministic phase shifts have to be considered and taken into account during the data evaluation. In the ideal case, all effects are already considered when the experiment is performed, so that the parameters of the experiment (e. g. the modulation frequency of the hypothetical additional interaction) can be chosen in order to minimize the influence of deterministic phase shifts on the final result.
The different effects leading to deterministic phase shifts, their origins and time dependencies are described in the following sections.

2.5.1 Chemical Shift and the Contribution of Earth's Rotation

The two effects of chemical shift and Earth's rotation both give a shift that is linear in time (if one considers the weighted phase difference).

The Chemical Shift

The literature values for the gyromagnetic values are $\gamma_{He} = 20.37894730(56)\cdot 10^7$ rad/(Ts) and $\gamma_{Xe} = 7.39954378(50)\cdot 10^7$ rad/(Ts) given by [45, 46] for the isolated ^{3}He and ^{129}Xe nuclei without their electron shells. The ratio of these literature values is

$$\frac{\gamma_{He}}{\gamma_{Xe}} \quad = \quad 2.75408159(20) \tag{2.43}$$

and can be used as a first estimate of the actual ratio.
In case of the whole ^{3}He and ^{129}Xe atoms, the electron shells shield the nuclei against the external magnetic guiding field (diamagnetic shielding). The strength of the magnetic field at the position of the nucleus is smaller than expected, resulting in a slightly lower

Larmor frequency. This effect, that is well-known from NMR experiments, is called chemical shift. The shielding factor depends on the actual electronic configuration, which can be exploited in NMR spectroscopy: The actual electron distribution of atoms in a molecule depends on the bond type and length to different binding partners etc. which gives rise to slightly (ppm level) different resonance frequencies of atoms that are of the same type (e. g. ^{1}H) but at different positions in the molecule.[4] This can be used to identify substances or to investigate the structure of molecules.
In the case of the ^{3}He-^{129}Xe comagnetometer, the chemical shift depends on the partial pressures of ^{3}He, ^{129}Xe and N_2 as they influence the formation rate and lifetime of dimers (mostly Xe-Xe van-der-Waals molecules) with the corresponding change in the electron configuration. Thus, the chemical shift may vary from run to run (each time the measurement cell is filled anew), but stays constant during a single measurement run. A deviation of the assumed value from the actual value γ_{He}/γ_{Xe} leads to a linear increase or decrease in time of the weighted phase difference if the magnetic guiding field is constant.[5]

The Contribution of Earth's Rotation

The experiments that are presented here are all performed on the surface of the Earth and rotate with the sidereal frequency

$$\begin{aligned} \Omega_E &= 2\pi/86164.101\ \mathrm{s}^{-1} \\ &= 7.2921150 \cdot 10^{-5}\ \mathrm{s}^{-1} \quad . \end{aligned} \tag{2.44}$$

Thus, the laboratory reference system is not an inertial frame of reference. The SQUID detectors rotate with a frequency ω_{det} with respect to the precessing spins and so the measured precession frequencies of ^{3}He and ^{129}Xe are the actual Larmor frequencies shifted by ω_{det}. In the weighted phase difference, this contribution is

$$\begin{aligned} \Delta\Phi_{\mathrm{Earth}} &= \left(\gamma_{\mathrm{He}} B_0 - \omega_{\mathrm{det}} - \frac{\gamma_{He}}{\gamma_{Xe}} \cdot (\gamma_{\mathrm{Xe}} B_0 - \omega_{\mathrm{det}})\right) \cdot t \\ &= \left(\frac{\gamma_{He}}{\gamma_{Xe}} - 1\right) \omega_{\mathrm{det}} \cdot t \quad . \end{aligned} \tag{2.45}$$

The sign and magnitude of ω_{det} depend on the orientation of the magnetic guiding field and the Earth's rotation axis, but stay constant during a measurement run. For a horizontal magnetic guiding field with an angle ρ to the north direction at a latitude Θ this is[6]

$$\omega_{\mathrm{det}} = \Omega_E \cos(\rho) \cos(\Theta) \ . \tag{2.46}$$

However, the exact determination of ρ is difficult and only possible with an uncertainty of about 1°.

[4] The proton (^{1}H) is used the most for NMR spectroscopy due to its large natural abundance in combination with the vast occurrence of hydrogen in organic materials and a high NMR sensitivity (large gyromagnetic ratio), besides ^{13}C, ^{15}N, ^{19}F and ^{31}P and others.

[5] The magnetic guiding field is constant on the 10^{-4} level during a measurement run. A small linear drift leads to a heavily suppressed quadratic drift in the weighted phase difference, which is so far not visible in the measurement data.

[6] Further information on the coordinate systems and transformations can be found in Appendix A.1 on page 127 .

Thus, the contributions of the chemical shift and Earth's rotation are combined in a single linear term. Then the coefficient of this term is fitted during data evaluation.

2.5.2 The Ramsey-Bloch-Siegert Shift

In 1940 F. Bloch and A. Siegert [48] described a shift in the spin precession frequency in NMR experiments due to the irradiation of an off-resonant oscillating magnetic field: In NMR experiments the spins are usually manipulated (e. g. 90° or 180° pulses) by switching on a linearly polarized magnetic field perpendicular to the magnetic guiding field oscillating at the Larmor frequency ω_L for a certain time. The linearly polarized field can be decomposed into two circularly polarized components, one at the Larmor frequency and one counter-rotating component with the frequency $-\omega_L$. Thus, the counter-rotating component is off-resonant by $2\omega_L$. This leads to the well-known Bloch-Siegert shift $\delta\omega_{\mathrm{BS}}$ in NMR experiments that depends quadratically on the magnitude B_1 of the oscillating field. If one assumes $\gamma B_1 \ll \omega_L$ the Bloch-Siegert shift is:

$$\delta\omega_{\mathrm{BS}} \quad = \quad \frac{(\gamma B_1)^2}{4\omega_L} \ . \tag{2.47}$$

This result was generalized by Ramsey [49]: The Ramsey-Bloch-Siegert shift gives the shift in Larmor frequency ω_L due to a rotating field with arbitrary amplitude B_1 and an arbitrary frequency ω_D:

$$\delta\omega_{\mathrm{RBS}}(t) = \pm\left(\sqrt{\Delta\omega^2 + \gamma^2 B_1^2(t)} - \Delta\omega\right) \quad \text{with} \quad \Delta\omega = |\omega_L - \omega_D| \ . \tag{2.48}$$

The plus sign applies to $\frac{\omega_D}{\omega_L} < 1$, the minus sign to $\frac{\omega_D}{\omega_L} > 1$, respectively (see Fig. 2.8). Eq. (2.47) is a special case of Eq. (2.48) with $\omega_D = -\omega_L$ and $\gamma B_1 \ll \omega_L$, which can be easily shown by expanding the square root.
In the case of the comagnetometer, B_1 is generated by the precessing magnetization of the polarized gas. Due to the exponential decay of the magnetization (with relaxation time constant T_2^*), $B_1(t)$ and consequently $\delta\omega_{\mathrm{RBS}}(t)$ is time dependent. The Ramsey-Bloch-Siegert shift in this case has two different manifestations that have to be taken into account, i. e. cross-talk and self-shift.

Cross-talk

The cross-talk emerges if there are two or more different spin species co-located in the same volume. In this case, the cross-talk describes the shift due to the influence of the precessing magnetization of the ^{3}He nuclei (with $\omega_D = \omega_{\mathrm{He}}$) on the ^{129}Xe precession frequency (and vice-versa). In this case, $\omega_1 = \gamma B_1 \ll \omega_L = \gamma B_0$ is fulfilled ($B_0 \approx 400$ nT

and $B_1 \approx 100$ pT), thus

$$\begin{aligned}
\delta\omega_{\mathrm{RBS}} &= \pm\sqrt{(\omega_L-\omega_D)^2+\omega_1^2} \mp |\omega_L-\omega_D| \\
&= \pm\sqrt{\Delta\omega^2+\omega_1^2} \mp \Delta\omega \\
&= \pm\Delta\omega\cdot\sqrt{1+\left(\frac{\omega_1}{\Delta\omega}\right)^2} \mp \Delta\omega \\
&\approx \pm\Delta\omega\cdot\left(1+\frac{1}{2}\left(\frac{\omega_1}{\Delta\omega}\right)^2\right) \mp \Delta\omega \quad (\omega_1 \ll \Delta\omega) \\
&= \pm\Delta\omega\cdot\frac{1}{2}\left(\frac{\omega_1}{\Delta\omega}\right)^2 \\
&= \pm\frac{\gamma^2 B_1^2}{2\Delta\omega}\ . \qquad (2.49)
\end{aligned}$$

In this case, $\Delta\omega = |\omega_{\mathrm{He}} - \omega_{\mathrm{Xe}}| = |\omega_{\mathrm{Xe}} - \omega_{\mathrm{He}}| \approx 2\pi \cdot 7$ Hz. The plus sign applies to $\omega_L < \omega_r$, which is the case if one considers the shift in the ^{129}Xe frequency. The minus sign applies to the shift in the ^{3}He frequency.
Thus, the shift in the ^{129}Xe frequency is:

$$\delta\omega_{\mathrm{RBS,\ Xe}}(t) = +\frac{\gamma_{Xe}^2 B_{1,He}(t)^2}{2\Delta\omega} = +\frac{\gamma_{Xe}^2 B_{1,He}(0)^2}{2\Delta\omega}\cdot e^{-\frac{2\cdot t}{T^*_{2,He}}}\ . \qquad (2.50)$$

To get the accumulated phase, one integrates over time:

$$\begin{aligned}
\delta\Phi_{\mathrm{RBS,\ Xe}}(t) &= \int_0^t \delta\omega_{\mathrm{RBS,\ Xe}}(t')dt' \qquad (2.51) \\
&= const. - \frac{\gamma_{Xe}^2 B_{1,He}(0)^2}{2\Delta\omega}\cdot\frac{T^*_{2,He}}{2}\cdot e^{-\frac{2\cdot t}{T^*_{2,He}}}\ . \qquad (2.52)
\end{aligned}$$

The constant term can be neglected (it can be absorbed into a final constant term in the description of all deterministic phase shifts).
In the weighted phase difference $\Delta\Phi = \Phi_{He} - \frac{\gamma_{He}}{\gamma_{Xe}}\cdot\Phi_{Xe}$ the sign of the effect changes:

$$\Delta\Phi_{\mathrm{RBS,\ Xe}}(t) = \frac{\gamma_{He}\gamma_{Xe}B_{1,He}(0)^2}{2\Delta\omega}\cdot\frac{T^*_{2,He}}{2}\cdot e^{-\frac{2\cdot t}{T^*_{2,He}}}\ . \qquad (2.53)$$

For the effect on ^{3}He, the procedure is the same, but here the sign in the weighted phase difference does not change:

$$\begin{aligned}
\delta\omega_{\mathrm{RBS,\ He}}(t) &= -\frac{\gamma_{He}^2 B_{1,Xe}(t)^2}{2\Delta\omega} = -\frac{\gamma_{He}^2 B_{1,Xe}(0)^2}{2\Delta\omega}\cdot e^{-\frac{2\cdot t}{T^*_{2,Xe}}} \qquad (2.54) \\
\delta\Phi_{\mathrm{RBS,\ He}}(t) &= \int_0^t \delta\omega_{\mathrm{RBS,\ He}}(t')dt' \\
&= const. + \frac{\gamma_{He}^2 B_{1,Xe}(0)^2}{2\Delta\omega}\cdot\frac{T^*_{2,Xe}}{2}\cdot e^{-\frac{2\cdot t}{T^*_{2,Xe}}} \qquad (2.55)
\end{aligned}$$

$$\Delta\Phi_{\mathrm{RBS,\ He}}(t) = \frac{\gamma_{He}^2 B_{1,Xe}(0)^2}{2\Delta\omega}\cdot\frac{T^*_{2,Xe}}{2}\cdot e^{-\frac{2\cdot t}{T^*_{2,Xe}}}\ . \qquad (2.56)$$

The cross-talk term of the Ramsey-Bloch-Siegert shift has the same sign for helium and xenon if one considers the weighted phase difference. The time evolution is described by the two exponential terms with time constants $\frac{1}{2}T^*_{2,Xe}$ and $\frac{1}{2}T^*_{2,He}$. This is a direct result of the quadratical dependence on B_1.
This shift is small compared to the other deterministic phase shifts, as B_1 is in the range of 10...100 pT, typically. The actual measurements in recent times achieved such a high sensitivity that it has to be considered during the data evaluation procedure with the term:

$$\Delta\Phi^{\mathrm{ct}}_{\mathrm{RBS}}(t) \;=\; F_{He}\cdot e^{-\frac{2\cdot t}{T^*_{2,Xe}}} + F_{Xe}\cdot e^{-\frac{2\cdot t}{T^*_{2,He}}} \quad .$$

For the cross-talk, not only the time evolution of the phase shift is known, but also the amplitudes can be determined if the strength of the magnetic field B_1 inside the measurement cell is known according to:

$$\begin{aligned} F_{He} &= \frac{\gamma^2_{He}B^2_{1,Xe}(0)\cdot T^*_{2,Xe}}{4\Delta\omega} \\ F_{Xe} &= \frac{\gamma_{He}\gamma_{Xe}B^2_{1,He}(0)\cdot T^*_{2,He}}{4\Delta\omega} \quad . \end{aligned} \tag{2.57}$$

In practice, the magnetic field inside the sample cell $B_1(t=0)$ can be determined by analyzing the signal of the SQUID magnetometers which directly measure the magnetic dipole field outside the spherical sample cell at their respective positions. The uncertainty in the determination of $B_1(0)$ is in the order of 5%, resulting in uncertainties of $\Delta\Phi^{\mathrm{ct}}_{\mathrm{RBS}}$ of about 10%. Due to these large uncertainties on F_{He} and F_{Xe}, they do not enter as fixed values, but are treated as fit parameters. This method of determining $B_1(0)$ via the external field and the treatment of fit parameters with additional and independent information on them are described in Chapter 3 (data evaluation of the Lorentz invariance violation measurements). In contrast, the characteristic time constants T^*_2 of the exponential decay of the precession signals, as well as the Larmor frequencies, could be determined with high precision, so that they enter as fixed values into the fitting procedure.

Self-shift

In contrast to the cross-talk, where two or more co-located spin species are necessary to generate an effect, the self-shift occurs even when there is only one spin species present. The self-shift is a result of the coupling of the precessing magnetic moments of the same spin species among each other in the presence of an inhomogeneous magnetic field.
The gradients of the magnetic guiding field $\boldsymbol{B_0}$ are in the order of pT/cm and amplitude of the magnetic field B_1 produced by the precessing magnetization is in the order of 10...100 pT, typically. Thus, $\Delta\omega < \gamma B_1$ (but not in every case $\Delta\omega \ll \gamma B_1$) holds.

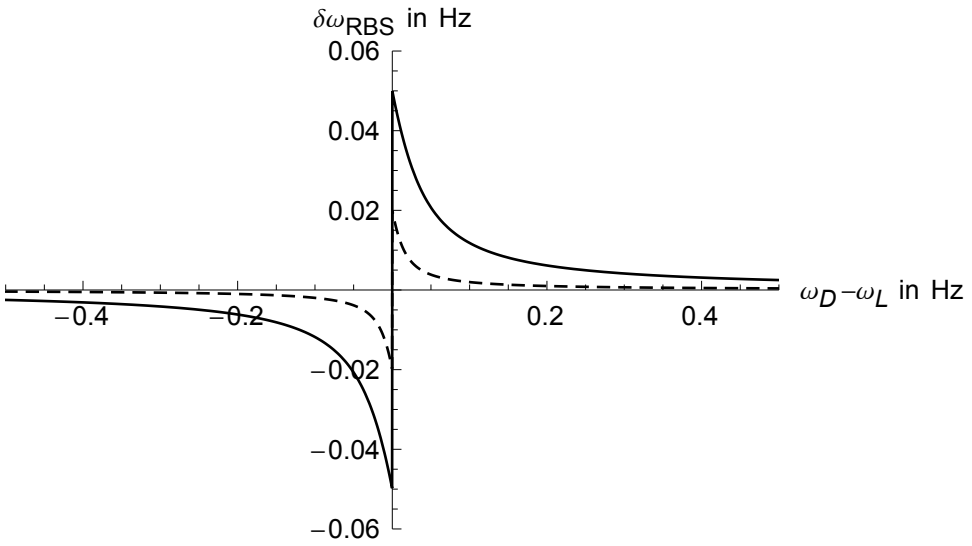

Figure 2.8: The Ramsey-Bloch-Siegert shift $\delta\omega_{\mathrm{RBS}}$ as a function of the difference between the driving frequency ω_D and the Larmor frequency of the undisturbed system ω_L for different amplitudes of the driving field $\gamma \cdot B_1 = 0.05$ Hz (black) and 0.02 Hz (dashed). At $\omega_D - \omega_L \approx 0$ the absolute value of the Ramsey-Bloch-Siegert shift $|\delta\omega_{\mathrm{RBS}}|$ reaches the maximum γB_1. The shift averages out to zero for small fluctuations around $\omega_D - \omega_L \approx 0$.

Therefore, by expanding in a Taylor's series one gets:

$$\begin{aligned}
\delta\omega_{\mathrm{RBS}} &= \pm\sqrt{(\omega_L - \omega_D)^2 + \omega_1^2} \mp |\omega_L - \omega_D| \\
&= \pm\sqrt{\Delta\omega^2 + \omega_1^2} \mp \Delta\omega \\
&= \pm\left(\omega_1\sqrt{1 + \left(\frac{\Delta\omega}{\omega_1}\right)^2} - \Delta\omega\right) \\
&= \pm\left(\omega_1\left[1 + \frac{\Delta\omega^2}{2\omega_1^2} - \frac{\Delta\omega^4}{8\omega_1^4} + \frac{\Delta\omega^6}{16\omega_1^6} - ...\right] - \Delta\omega\right) \\
&= \pm\left(\omega_1 - \Delta\omega + \frac{\Delta\omega^2}{2\omega_1} - \frac{\Delta\omega^4}{8\omega_1^3} + \frac{\Delta\omega^6}{16\omega_1^5} - ...\right) \ . \qquad (2.58)
\end{aligned}$$

In first-order approximation the time evolution of the self-shift is $\delta\omega_{\mathrm{RBS}}(t) \propto \gamma B_1(t) = B_1(0)\exp\left(-\frac{t}{T_2^*}\right)$. This is the regime of $\omega_D - \omega_L \approx 0$ (see Fig. 2.8) where $|\delta\omega_{\mathrm{RBS}}|$ reaches the maximum value γB_1.
However, in general, there is no precise model to determine the amplitudes of this effect. Some simple examples will be explained with the help of Fig. 2.9:
a) Two separate spherical cells with volumes V_1 and V_2 containing polarized spins are placed next to each other. Due to a gradient in the magnetic guiding field $\boldsymbol{B_0}$ the Larmor frequencies ω_{L1} and ω_{L2} differ in the two volumes. The self-shift $\delta\omega_{\mathrm{RBS1}}$ of

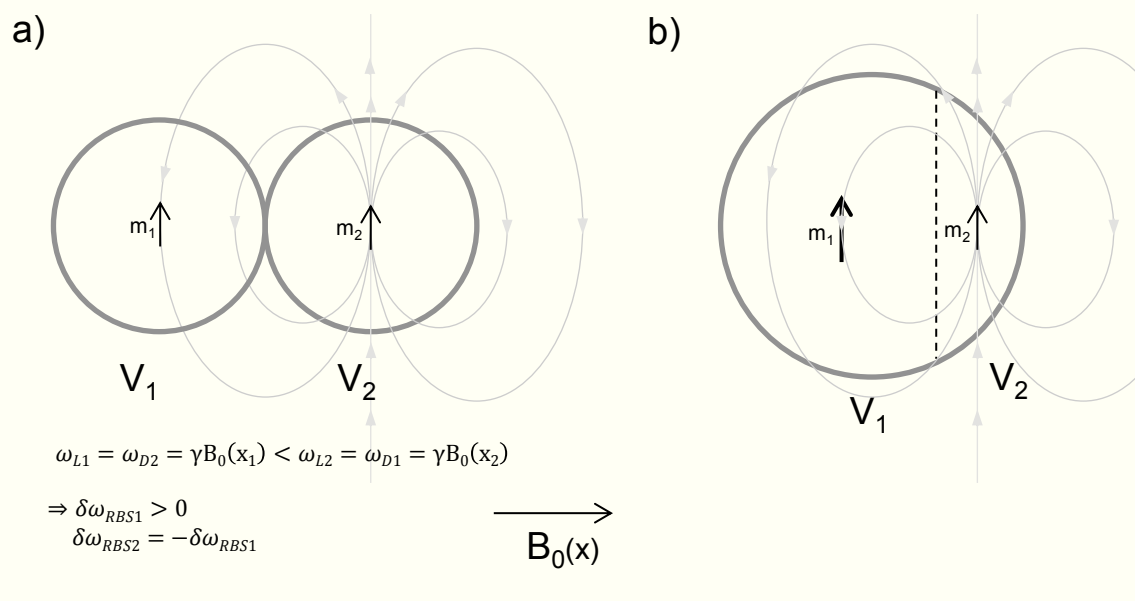

Figure 2.9: Illustration of the self-shift in an inhomogeneous magnetic field (a) for the symmetric case with two separate spherical volumes, (b) for a single spherical cell with two volumes with different Larmor frequencies. For a detailed description see text.

the Larmor frequency in the first volume is produced by the rotating dipole field of the second volume. If one assumes $\omega_{L1} < \omega_{L2}$, then $\delta\omega_{\mathrm{RBS1}} > 0$. In contrast, the rotating dipole field of the first volume causes a negative shift in the precession frequency of the second volume: $\delta\omega_{\mathrm{RBS2}} < 0$. If the magnetizations of the two volumes are equal, then $\delta\omega_{\mathrm{RBS2}} = -\delta\omega_{\mathrm{RBS1}}$.
If there is a connection between the two volumes, so that the spins can randomly move between the two volumes, the self-shift averages to zero (even if $V_1 \neq V_2$).
b) A single spherical cell in the presence of an inhomogeneous magnetic guiding field can be (mentally) divided into two volumes V_1 and V_2 with different Larmor frequencies ω_{L1} and ω_{L2}. As in example a), if one assumes $\omega_{L1} < \omega_{L2}$, then $\delta\omega_{\mathrm{RBS1}} > 0$ and $\delta\omega_{\mathrm{RBS2}} < 0$. So the Ramsey-Bloch-Siegert shift has opposite signs in the two volumes. However, the resulting frequency shift does not have to be zero in the general case, as one has to consider the different dwell times of spins in the two volumes, the strength of the rotating $\boldsymbol{B_1}$ fields (that are not necessarily dipole fields anymore), higher order gradients etc..
In general, the self-shift strongly depends on the field gradients across the sample cell, the resulting diffusion coefficients for ^{3}He and ^{129}Xe in the gas mixture, and the shape of the sample cell [38].
Finally, the self-shift has to be accounted for in the fitting procedure. The corresponding expression in the fit-function for the weighted phase difference is

$$\Delta\Phi^{\mathrm{ss}}_{\mathrm{RBS}}(t) = E_{He} \cdot e^{-\frac{t}{T^*_{2,He}}} + E_{Xe} \cdot e^{-\frac{t}{T^*_{2,Xe}}} \ . \tag{2.59}$$

The time-dependence of the self-shift is known. However, the proportionality factors E_{He} and E_{Xe} strongly depend on experimental parameters that can hardly be determined (gradients, shape of the sample cell, etc.). During the duration of a single run, these parameters are sufficiently constant, so that only the time dependence of $B_1(t)$ that is proportional to the signal amplitude enters. Since there is no precise enough model to calculate the self-shift amplitudes, E_{He} and E_{Xe} must be kept as free fit parameters.

2.5.3 Minor Phase Shifts

The phase shifts, that have been described above, contribute at a significant level and have to be accounted for explicitly in the analysis of the weighted-phase-difference data. Some minor additional phase shifts, that are too small to give a significant contribution at the current sensitivity level of the comagnetometer, are described in the following section.

Field gradient induced shifts

On page 35 the relaxation of transverse magnetization due to magnetic field gradients was described. Additionally, gradients lead to a small shift in the Larmor frequency which was shown by Cates et al. [78]. Gradients in the static magnetic guiding field $\boldsymbol{B_0}$ (which is aligned parallel to the z axis in this case) contribute. For a spherical sample cell with radius R and a diffusion coefficient of the gas D the frequency shift is given by

$$\delta\omega_{\text{grad}} \;=\; R^2\gamma^3|B_0|\left(|\boldsymbol{\nabla}B_{0,x}|^2+|\boldsymbol{\nabla}B_{0,y}|^2\right)\sum_n\left[x_{1n}^2\left(x_{1n}^2-2\right)\left(D^2x_{1n}^4R^{-4}+\gamma^2B_0^2\right)\right]^{-1} \tag{2.60}$$

Here x_{1n} are the zero points of the derivative of the spherical Bessel function ($\frac{d}{dx}j_1(x_{1n})=0,\ n=1,2,3,...$).
Cates showed that a similar term occurs for gradients in an oscillating magnetic field $\boldsymbol{B_1}(t)\propto\sin(\omega\cdot t)$. This effect is smaller and can be neglected.
The gradients in the magnetic guiding field are constant during a single measurement run, and thus, $\delta\omega_{\text{grad}}$ is constant. This gives a contribution to the linear term describing the weighted phase difference (which already includes the chemical shift and the contribution of Earth's rotation).

Gravitational shift

The functional principle of the comagnetometer is to become independent of drifts or variations in the magnetic guiding field by using two co-located spin species in the same measurement cell, so that the mean magnetic field is the same for both spin species. However, on closer examination, that is not exactly true if one considers the difference in the center of mass for ^{3}He and ^{129}Xe due to their different molar masses ($M_{3He}=3.016\ \frac{\text{g}}{\text{mol}}$ and $M_{129Xe}=128.955\ \frac{\text{g}}{\text{mol}}$).
The difference in the center of masses can be calculated using the barometric height formula that gives the pressure p at height z with $z=0$ at the center of the cell:

$$p(z) \;=\; p_0\exp\left(-\frac{z}{c}\right) \quad\text{with}\quad c=\frac{RT}{Mg} \tag{2.61}$$

with the pressure at the center of the cell p_0, the gas constant $R = 8.3\ \frac{\mathrm{J}}{\mathrm{mol\ K}}$, the temperature T (room temperature $T \approx 300$ K), and the gravitational acceleration at the Earth's surface $g = 9.81\ \frac{\mathrm{m}}{\mathrm{s}^2}$. For ^{3}He and ^{129}Xe the scale heights are:

$$\begin{aligned} c_{3He} &= 85305 \text{ m} \\ c_{129Xe} &= 1995 \text{ m} \end{aligned} \tag{2.62}$$

For a spherical cell with radius R the center of mass $\overline{z}$ is

$$\overline{z} \;=\; \frac{\int_{-R}^{R} dz\ z\ p(z)\left(R^2 - z^2\right)}{\int_{-R}^{R} dz\ p(z)\left(R^2 - z^2\right)}\ .$$

With $R = 0.05$ m the centers of mass are:

$$\begin{aligned} \overline{z}_{3He} &= -6 \cdot 10^{-9} \text{ m} \\ \overline{z}_{129Xe} &= -2.5 \cdot 10^{-7} \text{ m}\ . \end{aligned} \tag{2.63}$$

As expected, both centers of mass are below the center of the spherical glass cell. The difference in height for the two center of masses is

$$\Delta\overline{z} \;=\; \overline{z}_{3He} - \overline{z}_{129Xe} = 2.5 \cdot 10^{-7} \text{ m} = 0.25\ \mu\text{m}\ . \tag{2.64}$$

Correspondingly, for a cylindrical cell (cylinder axis perpendicular to the gravitational force) with radius R the center of mass is:

$$\overline{z} \;=\; \frac{\int_{-R}^{R} dz\ z\ p(z)\sqrt{R^2 - z^2}}{\int_{-R}^{R} dz\ p(z)\sqrt{R^2 - z^2}}$$

resulting in

$$\begin{aligned} \overline{z}_{3He} &= -7 \cdot 10^{-9} \text{ m} \\ \overline{z}_{129Xe} &= -3.1 \cdot 10^{-7} \text{ m}\ . \end{aligned} \tag{2.65}$$

and

$$\Delta\overline{z} \;=\; \overline{z}_{3He} - \overline{z}_{129Xe} = 3.1 \cdot 10^{-7} \text{ m} = 0.31\ \mu\text{m}\ . \tag{2.66}$$

The distance in the centers of mass for the two gases leads to a shift in the weighted frequency difference in the presence of z-gradients in the magnetic guiding field:

$$\begin{aligned} \delta\omega_{\mathrm{grav}} &= \omega_{\mathrm{He}} - \frac{\gamma_{\mathrm{He}}}{\gamma_{\mathrm{Xe}}}\omega_{\mathrm{Xe}} = \gamma_{\mathrm{He}} \cdot \left(B_{0,\mathrm{Xe}} + \frac{\partial B_0}{\partial z} \cdot \Delta\overline{z}\right) - \gamma_{\mathrm{He}} \cdot B_{0,\mathrm{Xe}} \\ &= \gamma_{\mathrm{He}} \cdot \frac{\partial B_0}{\partial z} \cdot \Delta\overline{z} \end{aligned} \tag{2.67}$$

If the gradients in the magnetic guiding field are constant during a single measurement run then $\delta\omega_{\mathrm{grad}}$ is constant and typically in the order of

$$\delta\omega_{\mathrm{grav}} \;=\; \gamma_{\mathrm{He}} \cdot \frac{\partial B_0}{\partial z} \cdot \Delta\overline{z} \approx 2 \cdot 10^8 \frac{\mathrm{rad}}{\mathrm{Ts}} \cdot 30 \frac{\mathrm{pT}}{\mathrm{cm}} \cdot 0.3\ \mu\text{m} = 186 \text{ nrad/s}\ . \tag{2.68}$$

In the weighted phase difference, this gives a contribution to the linear term. However, time-dependent gradients would immediately lead to a structure in the weighted phase difference. Special care has to be taken to avoid fluctuations of the gradients that have the same time structure as the fundamental effect under investigation. To give an example, an electric field has to be switched periodically for the search of the ^{129}Xe-EDM. If such an EDM is present this would manifest in a signal in the weighted phase difference with the periodical structure of the switching. However, high-voltage induced leakage currents generate inhomogeneous magnetic fields that have the same periodical structure and therefor could mimic a false EDM or mask a true EDM; a potential systematic error that has to be considered.

Interaction of the polarized gas with SQUIDs

When SQUIDs are used as direct magnetic flux detectors (see page 42), the screening and feedback currents produce magnetic fields (typically only the dipole fields are relevant if the distance to the SQUIDs is large compared to the extension of the SQUIDs). The 304-channel SQUID system in BMSR-2 at PTB Berlin uses this set-up. The influence of the magnetic dipole fields produced by the SQUIDs on the spins in the measurement cell was estimated by investigating the coupling of different SQUIDs among each other (e. g. correlation in the SQUID noise) and was found to be of no concern.
The SQUID system that has been developed for the ^{129}Xe-EDM experiment uses the set-up with SQUIDs as current sensors (see Fig. 2.6) where the current in the pick-up loop is always kept at zero by a feedback mechanism. Therefore no external field is produced and the spins in the measurement cell are not affected by the SQUID system.

3 Limit on Lorentz Invariance and CPT Violating Neutron Spin Interactions

In this chapter, I will describe the experiments that have been performed as a part of this thesis in order to put a limit on a Lorentz invariance and CPT violating coupling of the neutron spin $\boldsymbol{\sigma^n}$ to a hypothetical background field $\tilde{\boldsymbol{b}}^{\boldsymbol{n}}$. Such a coupling of the form

$$V = -\tilde{\boldsymbol{b}}^{\boldsymbol{n}} \cdot \boldsymbol{\sigma^n} \tag{3.1}$$

is motivated in Section 1.2.1 on page 12 within the minimal Standard Model Extension. The background field has a distinct direction is space that is constant in time (on the time scale of the experiment). As the laboratory frame of reference rotates with the Earth, a coupling of such a kind (Eq. (3.1)) would lead to a variation of the Larmor frequencies with the period of the sidereal day. Comparing the Larmor frequencies of co-located nuclear polarized ^{3}He and ^{129}Xe spin samples (comagnetometry) is the method of choice to get independent of magnetic field drifts, as explained above.
The components and methods, that have been utilized in this experiment, are described in the following section. Then, the general data evaluation procedure from raw data to the weighted phase difference (and other important intermediate data like signal amplitudes, relaxation time constants) is presented. Subsequently, two different types of measurement strategies, that have been applied, are discussed: Firstly, measurements using a slowly rotating magnetic guiding field are described. Though the results of these measurements did not flow into the final limits on Lorentz invariance violation, a lot of knowledge about the behavior of the comagnetometer, the mu-metal shielding and the measurement system etc. could be derived. Thereafter, the measurements using a static magnetic guiding field and method of data evaluation with the extraction of limits on Lorentz invariance violation are described in detail. Finally, the phase stability of the comagnetometer and systematic uncertainties are discussed.

3.1 Experimental Technique

The experiments were performed inside the strongly magnetically shielded room *BMSR-2* at the *Physikalisch-Technische Bundesanstalt* at Berlin (latitude $\Theta = 52.52°$) in the year 2012. It is the best shielded room worldwide with shielding factors of 10^6 at 1 Hz and 10^9 at 10 Hz [90]. With seven layers of mu-metal with a total thickness of 30 mm, an aluminum Faraday cage (10 mm), active shielding, and an additional HF-shield the magnetic noise level inside is reduced to about 3 fT/$\sqrt{\text{Hz}}$ for frequencies of a few Hz (above about 1 Hz the noise spectrum becomes white). The gradients reach a level of a few pT/cm at the center of the shielded room. A schematic view and an image of the room can be found in Fig. 2.3 on page 40 with general information about magnetic

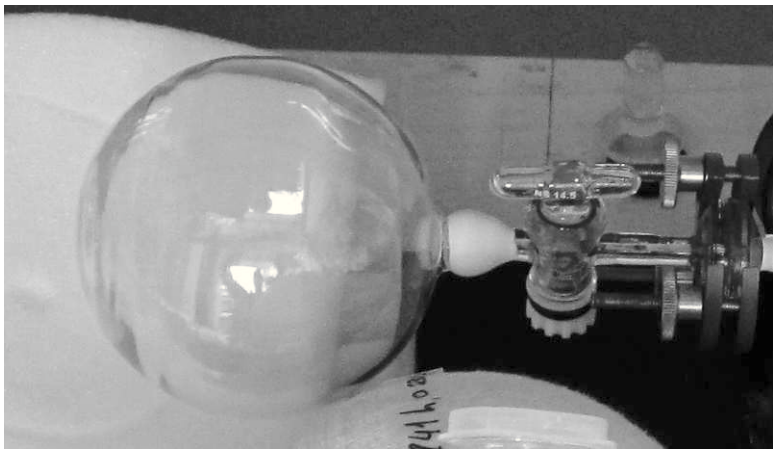

Figure 3.1: The spherical sample cell with a radius $R = 5$ cm attached to the filling station on the right side.

shielding on the same page. The room has a cubic shape with an inner edge length of 2.9 m.
Two square Helmholtz coil pairs (B_x- and B_y-coils) were installed inside the room. They were mounted perpendicular to each other, so that any horizontal direction of the magnetic guiding field could be chosen by adjusting the currents through the coils. The edge lengths of the B_x- and B_y-coils were 180 cm and 175 cm and the distances between the individual coils were 97 cm and 94 cm, respectively. Each coil had 20 windings. Thus, a current of 20 mA through a Helmholtz coil pair produced a field of about 400 nT in the center of the room.
The adjustable, low-noise two-channel current source, that was developed for these measurements (see p. 41), was placed inside the HF-shield and active shield, but outside the seven layers of mu-metal, and connected to the two coil pairs.
The ^{3}He and ^{129}Xe nuclear spins were polarized outside the shielding by means of optical pumping. Polarized ^{3}He gas was produced at Mainz using MEOP and then send to Berlin via regular parcel service in the special transport boxes. Due to its fast depolarization, ^{129}Xe was polarized by SEOP on site by W. Kilian [88].
The measurement cells have to be prepared with care in order to get a low longitudinal relaxation rate. Previous experiments have proven that GE-180 glass shows very low wall relaxation rates. The cells are of a spherical shape with a radius $R = 5$ cm with a stem to fill the cell. To get rid of ferromagnetic contaminations on the inner surface, the cells were cleaned with a two percent solution of Mucasol and afterwards with distilled water. Then a glass valve was glued to the stem of the cell (see Fig. 3.1). After the cleaning process the cells were evacuated and demagnetized. To do so, the cells were put into a strong oscillating magnetic field ($f \approx 3$ Hz) with an initial strength of about 0.2 T. The field amplitude was decreased linearly to zero in about 20 minutes. This procedure demagnetizes microscopic ferromagnetic particles which - especially if in direct contact with the polarized gas - otherwise would lead to a fast depolarization. Several cells were manufactured and prepared, so that finally the ones with the highest $T_{1,\,\mathrm{He}}$

(for good cells values of up to 300 hours) could be chosen for the experiment.
An existing NMR setup in Mainz was used to measure $T_{1,\,\mathrm{He}}$. Polarized ^{3}He (about 200 mbar) was filled into the cell which was kept in a magnetic guiding field of about 0.8 mT. Every 15 minutes the spins were flipped by a small angle $\alpha < 3°$ and the Free Induction Decay (FID) signal of the transverse magnetization was detected. The amplitude of the FID signal as a function of time allows the extraction of $T_{1,\,\mathrm{He}}$.
The low-relaxation spherical glass vessel was prepared inside the filling station. Typically, the optimum conditions in terms of long transverse relaxation times (T_2^*) and high signal-to-noise ratio were met at a gas mixture with pressures of $p_{He} = 3$ mbar, $p_{Xe} = 5$ mbar, $p_{N2} = 25$ mbar. The Xe gas was enriched to 91% ^{129}Xe, and the He gas was pure ^{3}He. Nitrogen suppresses spin-rotation coupling in bound Xe-Xe van-der-Waals molecules (see page 37). The sample cell was placed in the deactivated transport coil, and then the magnetic field of the transport coil was slowly ramped up. It was ensured that the field of filling station and transport coil were aligned to avoid spin flipping. Then the transport coil (with the cell inside) was brought into the shielded room. Then the cell was placed in the center of the room below the dewar that houses the SQUID sensors. The field inside the room was aligned in the y-direction, so that the field of the transport coil (which was brought through the door in a horizontal position) pointed into the same direction. Subsequently, the transport coil was ramped down and removed. After shutting the doors, the sample spins could be manipulated by changing the magnetic guiding field, e. g. spin flip by non-adiabatic switching.
The sinusoidal change in magnetic flux due to the spin precession of the gas atoms was detected by a 304-channel low-temperature SQUID-system with its corresponding high resolution data acquisition unit. This system was originally designed and installed by the PTB for biomagnetic and related applications (e. g. magnetocardiogram) [93]. The SQUIDs are placed in a liquid-helium dewar that is attached to the ceiling of BMSR-2. The dewar has a flat bottom with an inner diameter of 250 mm and houses 19 identical modules. Each module consists of 16 SQUIDs that measure the x, y, and z-component of the magnetic field at four different heights (0, 30, 70 and 140 mm) above the dewar bottom. No external pick-up loops are used, so the SQUIDs measure the field directly at their positions. The output signals of the SQUIDs are digitalized with $f_{\mathrm{sampling}} = 250$ Hz and recorded. Usually, only the data of a few (about 16) magnetometers in the proximity of the sample cell are saved to avoid large data files.

3.2 Data Evaluation

In this section, the general data evaluation procedure with the different steps from raw data to the weighted phase difference and other important intermediate data (like signal amplitudes, relaxation time constants, etc.) is discussed.

Gradiometers

The recorded SQUID signals were processed off-line after the measurement was finished. The typical raw signal can be seen in Fig. 3.2 with the sinusoidal change in the magnetic flux at the SQUID position due to the precessing magnetization (at the Larmor frequencies ≈ 13 Hz and 5 Hz for $B_0 = 400$ nT). The measured signal amplitudes for the lowest SQUIDS (the ones that are next to the sample cell) were up to 20 pT and

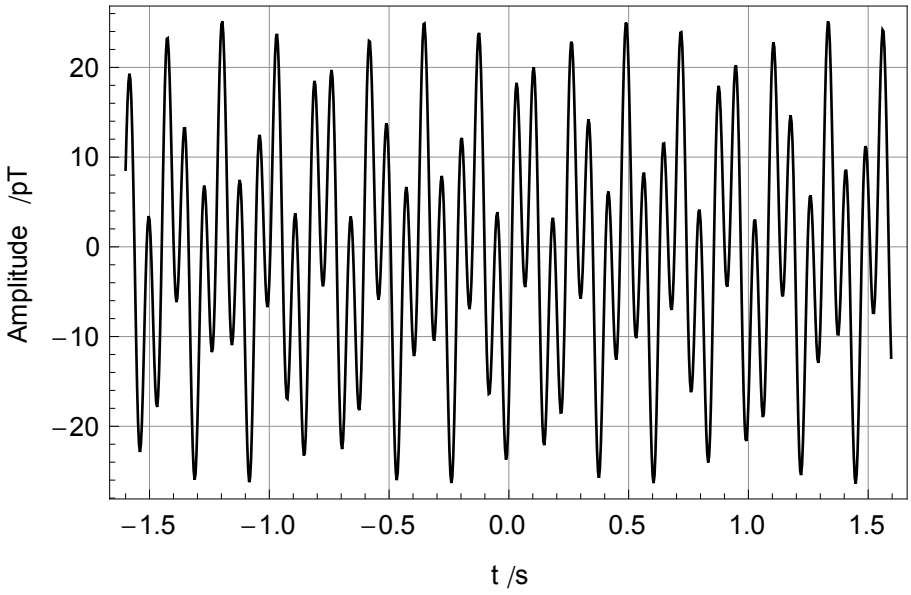

Figure 3.2: A single magnetometer raw signal with the prominent beating of the ^{3}He and ^{129}Xe precession signal at the Larmor frequencies $\approx$ 13 Hz and 5 Hz (this corresponds to $B_0 = 400$ nT).

8 pT for ^{3}He and ^{129}Xe, respectively. The corresponding spectrum of the raw signal for a single magnetometer can be seen in Fig. 3.3 (top). The prominent sharp peaks at around 5 Hz and 13 Hz correspond to the precession frequencies of ^{3}He and ^{129}Xe. The single magnetometer spectrum shows large and broad structures around 10 Hz and 15 Hz stemming from mechanical vibrations of the building and of the dewar itself in the (slightly inhomogeneous) magnetic guiding field. The narrow peaks at 50 Hz and 100 Hz are caused by irradiation from power lines. Noise from these sources can be greatly reduced by using gradiometry, in this case "software gradiometry": One chooses a magnetometer in the proximity of the sample cell and subtracts the signal of a magnetometer at a larger distance (in this case a gradiometer baseline length of $b = 70$ mm was chosen). Thus, a homogeneous magnetic field (or field change) does not give a resulting signal. However, point-like signal sources next to the lower magnetometer, that have a typical dipole field distribution, are attenuated very little (12.5 % for $d = b$, see Eq. (2.40) on page 45). The spectrum of such a gradiometer signal is shown in Fig. 3.3 (bottom). Thus, always gradiometer data was used in the following evaluation.

Fit to sub-cut data

To extract the ^{3}He and ^{129}Xe amplitudes, frequencies and phases the method of piecewise fitting to the gradiometer signal data was applied: The data of the gradiometer was split into packages (sub-cuts) with the length of $\Delta t = 3.2$ s. This corresponds to 800 data points at the sampling frequency 250 Hz. For a measurement run that lasted about one day, the resulting number of sub-cuts was about $N = 3 \cdot 10^4$. In Fig. 3.2 one of these

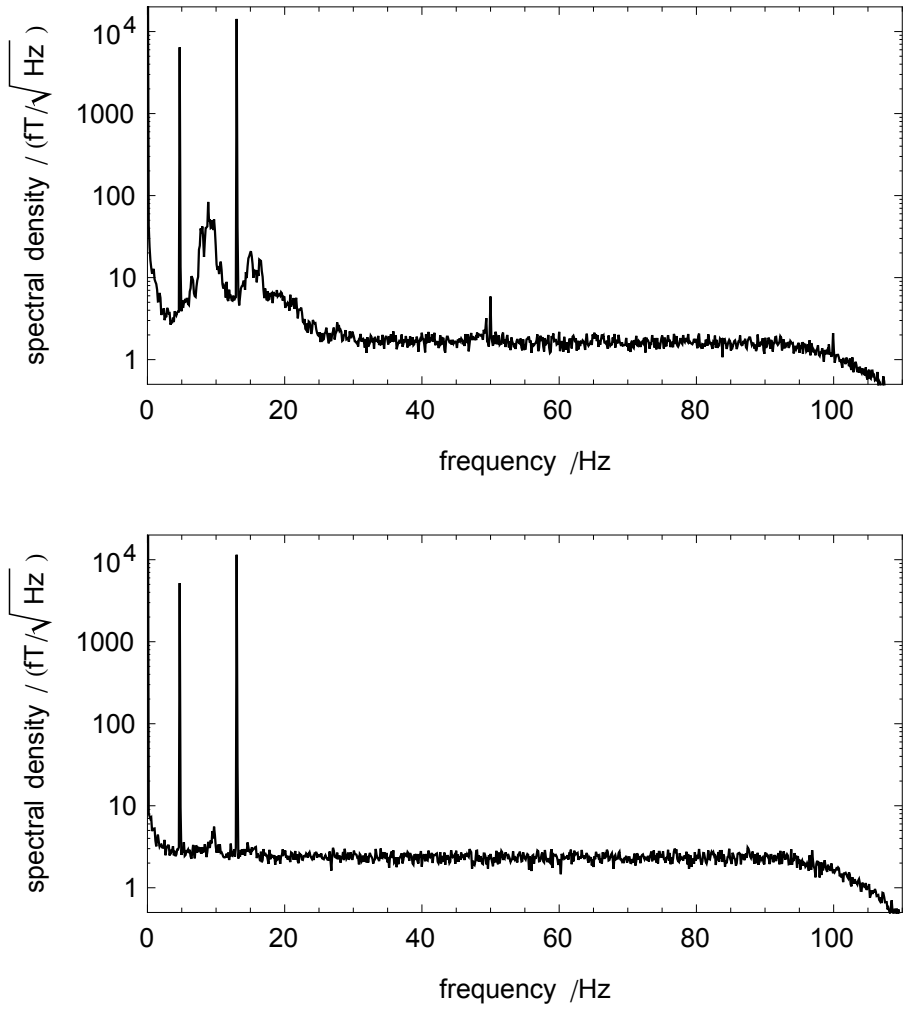

Figure 3.3: The spectrum (amplitude spectral density) of a single magnetometer (top) and a gradiometer (bottom). The gradiometer signal was calculated using the signal of a magnetometer next to the sample cell and subtracting the signal of a magnetometer that is 70 mm above ("software gradiometer"). The prominent sharp peaks at around 5 Hz and 13 Hz correspond to the precession frequencies of ^{3}He and ^{129}Xe. The single magnetometer spectrum shows large and broad structures around 10 Hz and 15 Hz stemming from mechanical vibrations, and narrow peaks at 50 Hz and 100 Hz (irradiation from power lines). These undesired signals are extremely reduced in the gradiometer signal. For frequencies above 100 Hz the anti-aliasing low pass filter roll-off can be seen (sampling frequency 250 Hz). The white noise level of the gradiometer is increased by a factor $\sqrt{2}$ compared to the single magnetometer due to the addition of uncorrelated noise of two SQUIDs.

sub-cuts can be seen.
The system noise was estimated by integrating over the noise spectrum from ≈ 0.3 Hz to 100 Hz. This value was determined for each gradiometer individually and for each measurement run anew. Typical values were in the range of $\sigma = 25$ ... 40 fT. This value was used as an uncertainty of the data points. Subsequently, the function

$$\begin{aligned} f^i_{\mathrm{raw}}(t') &= A^i_{\mathrm{He}} \cdot \cos\left(\omega^i_{\mathrm{He}} t'\right) + B^i_{\mathrm{He}} \cdot \sin\left(\omega^i_{\mathrm{He}} t'\right) + A^i_{\mathrm{Xe}} \cdot \cos\left(\omega^i_{\mathrm{Xe}} t'\right) + B^i_{\mathrm{Xe}} \cdot \sin\left(\omega^i_{\mathrm{Xe}} t'\right) \\ &\quad + c^i_0 + c^i_1 \cdot t' \end{aligned} \tag{3.2}$$

was fitted to the data of each individual sub-cut, denoted by (i). The sin- and cos-terms describe the ^{3}He and ^{129}Xe precession signals at the corresponding Larmor frequencies ω_{Xe} and ω_{Xe}, while the linear term accounts for the SQUID offset and a small drift of this offset in time. To minimize the correlation between the sin- and cos-terms, and the correlation between c_0 and $c_1 \cdot t'$, $t' = 0$ was chosen to be in the middle of the sub-cut, so that the data points laid symmetrically around zero from $t' = -\Delta t/2 = -1.6$ s to $t' = \Delta t/2 = 1.6$ s. The length of the sub-cuts was chosen so that the number of data points (800) was high enough for a statistical analysis on the one hand, but the length of a sub-cut ($\Delta t = 3.2$ s) was short enough, so that the drift of the SQUID offset could be described by the linear term on the other hand. The non-linear fit parameters ω_{Xe} and ω_{Xe} are very sensitive to the start values for the fit (the chances that the fit won't converge are high if one uses start values that are too far away from the actual values of ω_{Xe} and ω_{Xe}), so that the fit results of the previous sub-cut were used as start values.
Finally, for each sub-cut, one gets a set of estimations for the eight fit parameters $A_{\mathrm{He/Xe}}$, $B_{\mathrm{He/Xe}}$, $\omega_{\mathrm{He/Xe}}$, c_0 and c_1 and their uncorrelated and correlated uncertainties, and additionally, χ^2 as a measure of the goodness of the fit. The residuals (the measured data after subtraction of the fitted function in Eq. (3.2)) can be seen in Fig. 3.4 for a single magnetometer (top) and a gradiometer (bottom). The fit model is well suited for the gradiometer data, whereas for the magnetometer data the mechanical vibrations, that have been mentioned earlier, can not be neglected.

As the number of sub-cuts is very high for a measurement run lasting one day (about $N = 3 \cdot 10^4$), the distribution of the χ^2 values can be compared to the expected χ^2-distribution: The number of data points per sub-cut is 800 and the number of free fit parameters is 8, resulting in 792 degrees of freedom (d.o.f.). For this large number the χ^2-distribution can be approximated by a Gaussian probability distribution very well. Conveniently, one considers the χ^2/d.o.f. with an expected mean of one and a standard deviation $\sigma = \sqrt{\text{d.o.f.} - 1}/\text{d.o.f.} \approx 2/\sqrt{\text{d.o.f.}} \approx 0.050$. In Fig. 3.5 the observed $\chi 2$/d.o.f.-distribution of the sub-cut data fits is displayed, which is consistent with the expected values. This shows that the estimation of the uncertainty of the amplitude of each data point (stemming from the integral over the noise spectrum) is reasonable and the fit function describes the data well.[1]
In earlier measurements [39, 42] for about 5% of the sub-cuts χ^2/d.o.f. was larger than

[1] On a closer look, the observed standard deviation $\sigma' = 0.073$ is slightly larger than the expected one $\sigma = 0.050$ and the observed mean $\mu' = 1.012$ is also slightly larger than the expected mean $\mu = 1$. The total noise amplitude has been estimated correctly; however the noise is not pure Gaussian (white) noise, but has some correlation (e. g. vibrations, $1/f$-noise at low frequencies, etc.), which is consistent with the spectrum (Fig. 3.3). The non-Gaussian noise has not been included in the fit model.

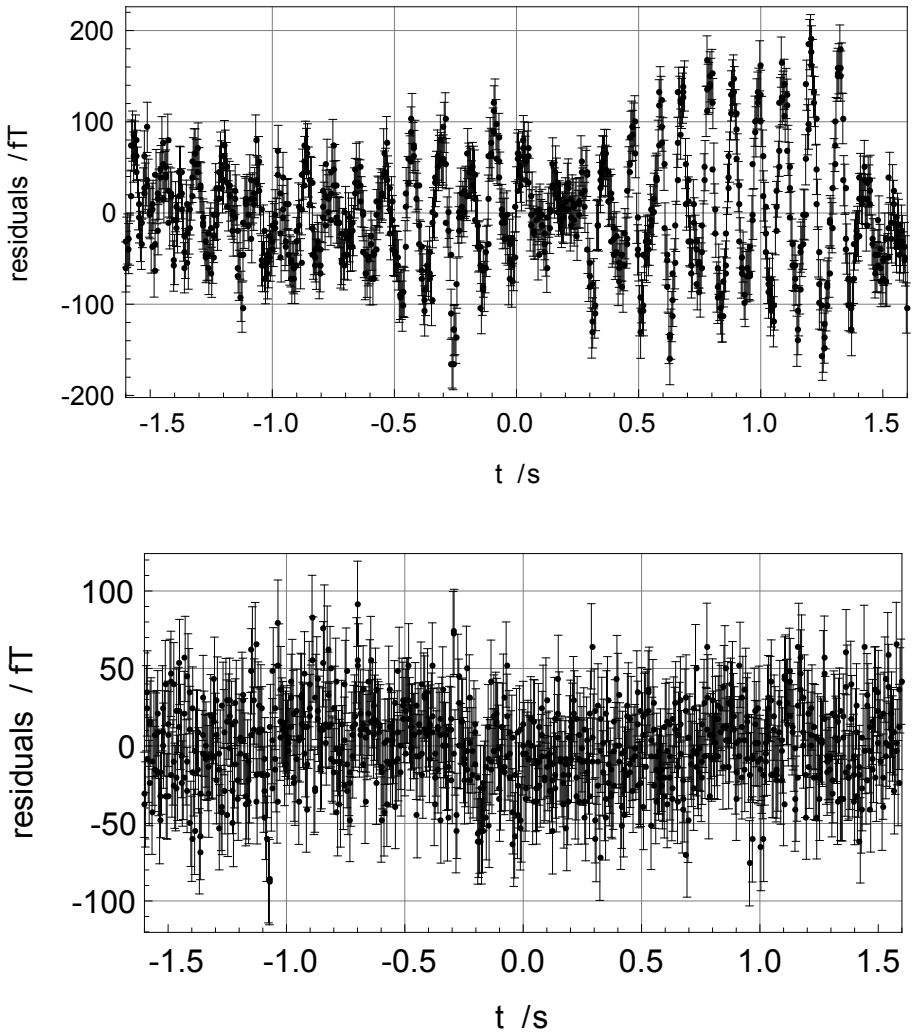

Figure 3.4: Residuals of the magnetometer data (top) and gradiometer data (bottom) after subtraction of the fitted function in Eq. (3.2) from the measured data for a single sub-cut. There is a clear structure in the magnetometer residuals stemming from vibrations. The residuals of the gradiometer seem to be Gaussian distributed.

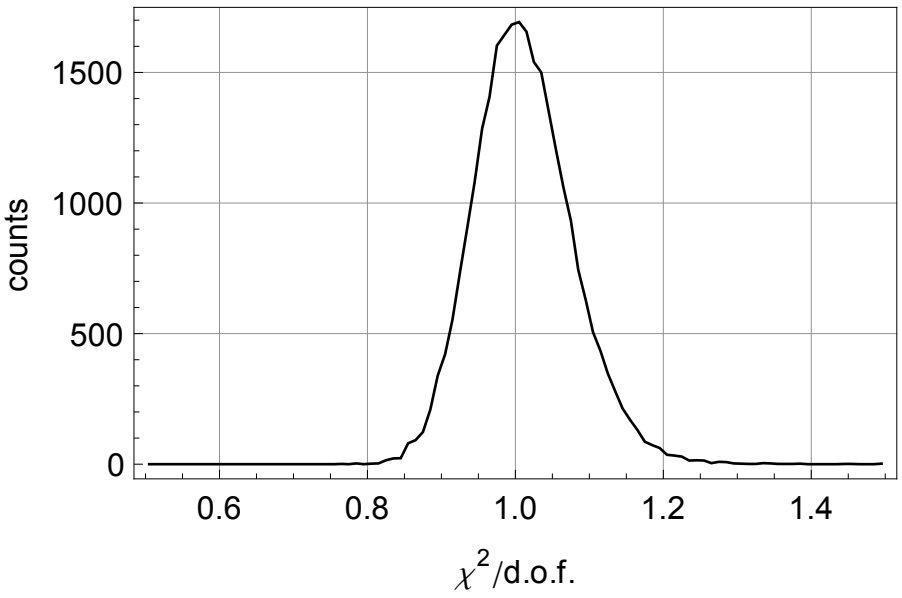

Figure 3.5: The observed $\chi 2$/d.o.f.-distribution of the sub-cut data fits with $N = 27695$ with mean $\mu' = 1.012$ and standard deviation $\sigma' = 0.073$. For d.o.f. = 792 the expected $\chi 2$/d.o.f. distribution has a Gaussian shape with a mean value $\mu = 1$ and a standard deviation $\sigma = 0.050$.

2 and could reach values of a few hundred. These sub-cuts had to be discarded and could not be used for the further analysis. On a closer inspection, a jump in the SQUID signal with an amplitude in the order of 1 pT arose in the corresponding sub-cuts. The origin of these jumps was not clear. A possible explanation is an slight instability of the old current sources which have been substituted by the new ones (p. 41). In these new measurements (testing Lorentz invariance), no such jumps occurred and all sub-cuts could be used for the further analysis.

Determination of Amplitudes and Phases

In the previous step of the data analysis (fit to the sub-cuts), a set of estimations for the eight fit parameters $A_{\mathrm{He/Xe}}$, $B_{\mathrm{He/Xe}}$, $\omega_{\mathrm{He/Xe}}$, c_0 and c_1 and their uncorrelated and correlated uncertainties for each sub-cut was obtained. The Larmor frequencies ω_{He} and ω_{Xe} are directly proportional to the strength of the magnetic guiding field B_0, and thus, can be used as a measure for the stability of B_0. In Fig. 3.6 (right) the measured Larmor frequencies are plotted as a function of time for a measurement run lasting about one day with a constant current through the coils. In the first two to three hours, the relative drift of the magnetic guiding field is in the order of 10^{-5} per hour, corresponding to an absolute drift of 4 pT per hour due to the relaxation of the mu-metal shielding.

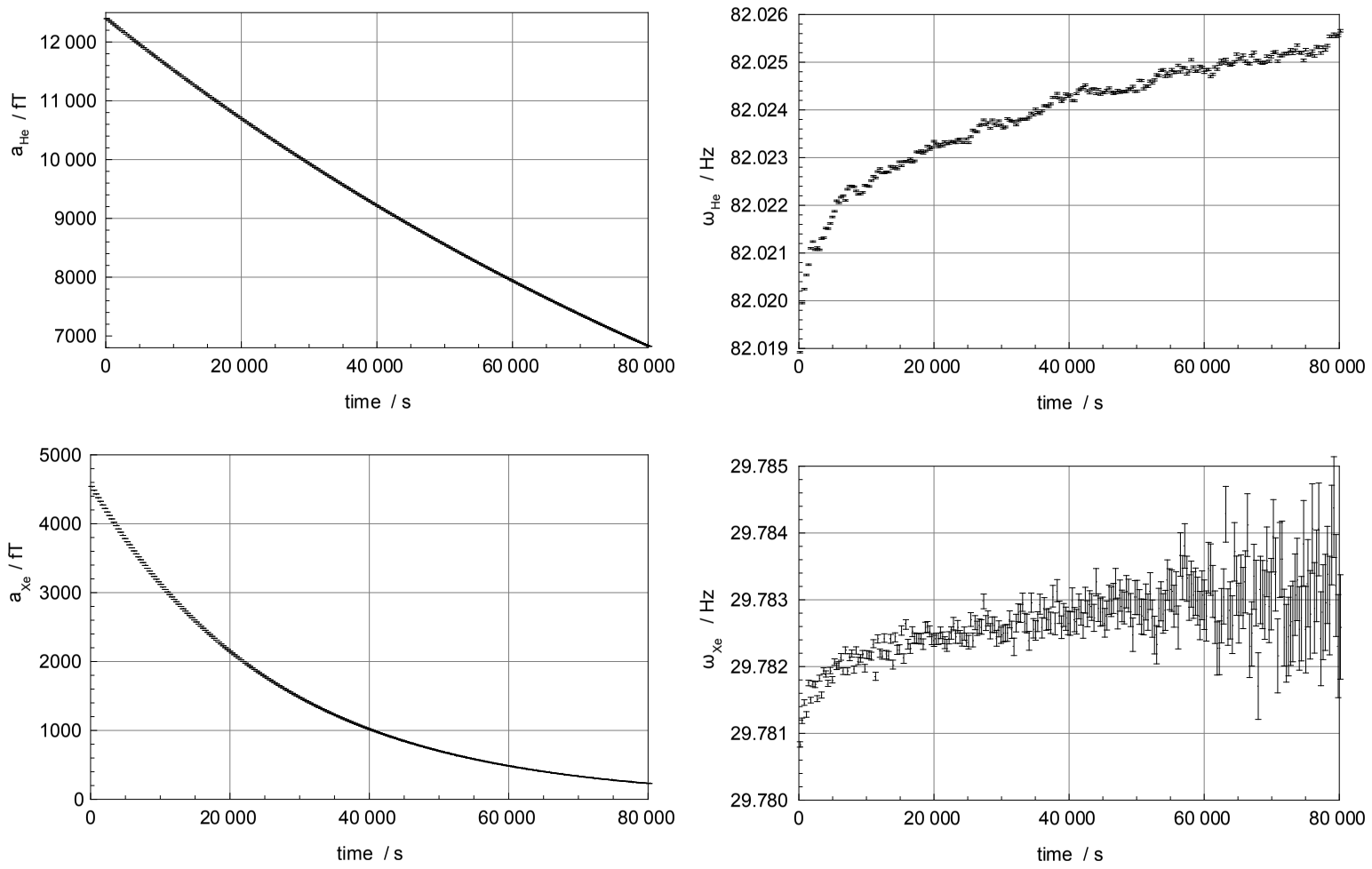

Figure 3.6: The measured signal amplitudes (left) and Larmor frequencies ω (right) of ^{3}He (top) and ^{129}Xe (bottom) as a function of time (for a single measurement run lasting about one day). Here the current through the coils was kept constant after the initial non-adiabatic switching (spin flip).

The mu-metal adapts to the Earth magnetic field, that penetrates through the open doors when the sample cell is brought into the room and pushed out when the doors are closed, as well as to the magnetic guiding field that is switched at the beginning of the measurement. After about 10 hours the drift reaches small values in the order of 10^{-6} per hour (corresponding to 0.4 pT per hour) when the mu-metal has settled and is in equilibrium. The Larmor frequency uncertainty is much larger for ^{129}Xe as the signal is smaller, especially towards the end of the measurement run due to the shorter transverse relaxation time.
The amplitudes $a_{\mathrm{He/Xe}}$ of the ^{3}He and ^{129}Xe signals are calculated from the fit parameters $A_{\mathrm{He/Xe}}$ and $B_{\mathrm{He/Xe}}$ according to

$$a_{\mathrm{He/Xe}} \;=\; \sqrt{A^2_{\mathrm{He/Xe}} + B^2_{\mathrm{He/Xe}}}\,. \tag{3.3}$$

The uncertainties of $a_{\mathrm{He/Xe}}$ are determined from the uncertainties of $A_{\mathrm{He/Xe}}$ and $B_{\mathrm{He/Xe}}$ via Gaussian uncertainty propagation. In Fig. 3.6 (left) the signal amplitudes are plotted as a function of time. The transverse relaxation times $T^*_{2,\,\mathrm{He/Xe}}$ can be extracted by exponential fits to the amplitude data:

$$a_{\mathrm{He/Xe}}(t) = a_{0,\,\mathrm{He/Xe}} \cdot e^{-\frac{t}{T^*_{2,\,\mathrm{He/Xe}}}}\,. \tag{3.4}$$

As mentioned earlier, T_2^* strongly depends on the gradients of the magnetic field. These gradients are sufficiently constant over the period of a single measurement run, so that the transverse relaxation times can be considered as constant, too.
For the further evaluation, the phases of the ^{3}He and ^{129}Xe signals are of main interest as they can be determined very precisely. The phases $\varphi^{(i)}_{\mathrm{He}}$ and $\varphi^{(i)}_{\mathrm{Xe}}$ (in the range of $[0,\ 2\pi)$) for each sub-cut (i) at the middle of the sub-cut (at $t' = 0$) are determined by

$$\varphi^{(i)}_{\mathrm{He/Xe}} \;=\; \mathrm{arctan2}(B^{(i)}_{\mathrm{He/Xe}},\ A^{(i)}_{\mathrm{He/Xe}}) + \pi\ \ . \tag{3.5}$$

Here "arctan2$(B,\ A)$" with two arguments automatically chooses the right quadrant for the phases (unlike arctan(B/A)). The function arctan2$(B,\ A) + \pi$ instead of arctan2$(A,\ B)$ is used so that φ lies in the range of $[0,\ 2\pi)$ instead of $[-\pi,\ \pi)$.
These phases $\varphi^{(i)}_{\mathrm{He}}$ and $\varphi^{(i)}_{\mathrm{Xe}}$ at the times $t^{(i)} = (i - 1/2) \cdot \Delta t$ are the accumulated phases modulo 2π. Thus, to determine the accumulated phases $\Phi^{(i)}_{\mathrm{He}}$ and $\Phi^{(i)}_{\mathrm{Xe}}$ at $t^{(i)}$, one has to add the appropriate multiples of 2π (see Fig. 3.7):

$$\Phi^{(i)}_{\mathrm{He/Xe}} \;=\; n^{(i)}_{\mathrm{He/Xe}} \cdot 2\pi + \varphi^{(i)}_{\mathrm{He/Xe}} \tag{3.6}$$

with the numbers $n^{(i)}_{\mathrm{He}}$ and $n^{(i)}_{\mathrm{Xe}}$ of revolutions of the ^{3}He and ^{129}Xe magnetization from the beginning of the measurement run at $t = 0$ till $t^{(i)}$ (which is the center of the i-th sub-cut). $n^{(i)}_{\mathrm{He/Xe}}$ is calculated by taking $n^{(i-1)}_{\mathrm{He/Xe}}$ and adding $\Delta n^{(i)}_{\mathrm{He/Xe}}$ which is defined by

$$\Delta n^{(i)}_{\mathrm{He/Xe}} \;=\; \left[\frac{\omega^{(i)}_{\mathrm{He/Xe}} \cdot \Delta t - \left(\varphi^{(i)}_{\mathrm{He/Xe}} - \varphi^{(i-1)}_{\mathrm{He/Xe}}\right)}{2\pi}\right]\ \ . \tag{3.7}$$

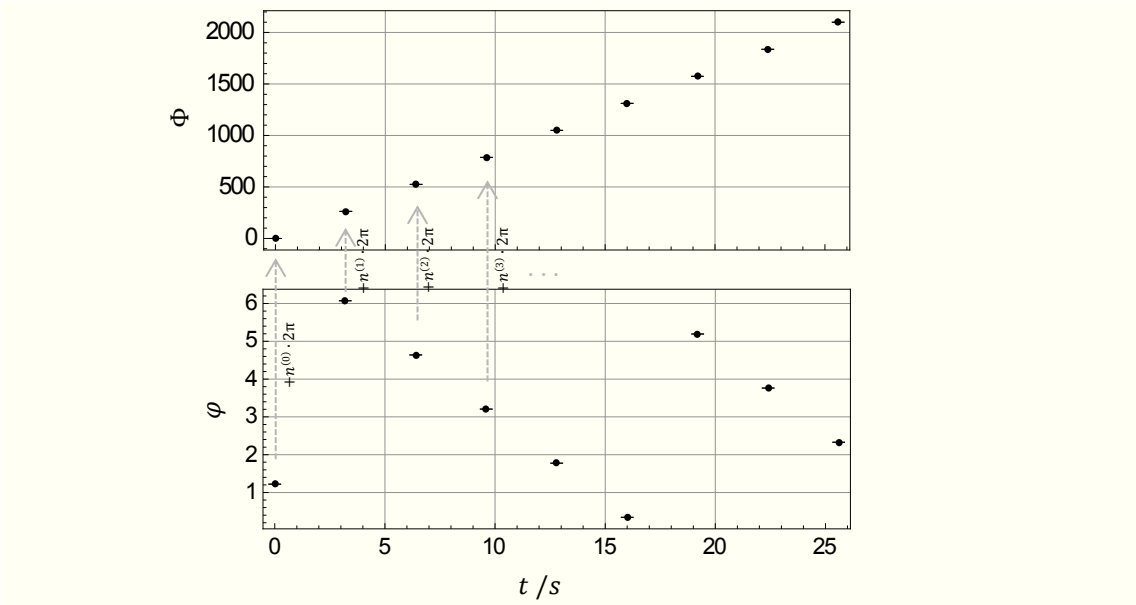

Figure 3.7: The accumulated phases $\Phi^{(i)}$ at $t^{(i)}$ are determined by adding the appropriate multiples of 2π to $\varphi^{(i)}$.

Here $[\cdot]$ is the "nearest-integer function" (rounding to the nearest integer). As ω is very constant, so that the argument within the brackets on the right side of Eq. (3.7) is already very close to an integer (e. g. 41.9997 for ^{3}He at $B_0 = 400$ nT), a false mapping does not occur[2]. In other words: The number of revolutions of the magnetization is estimated by the Larmor frequency, which is known precisely enough. The accumulated phases Φ_{He} and Φ_{Xe} increase almost linearly in time (as the Larmor frequencies are almost constant) and after one day of measurement reach about $\Phi_{\mathrm{He}}(t = 1\mathrm{day}) \approx 82\ \mathrm{Hz} \cdot 86400\ \mathrm{s} \approx 7 \cdot 10^6$ rad and $\Phi_{\mathrm{Xe}}(t = 1\mathrm{day}) \approx 30\ \mathrm{Hz} \cdot 86400\ \mathrm{s} \approx 2.6 \cdot 10^6$ rad, respectively. The uncertainties of the accumulated phases for ^{3}He are on the 10^{-4} rad level, while the corresponding uncertainties for ^{129}Xe vary from $5 \cdot 10^{-4}$ rad at the beginning to 10^{-2} rad at the end of the measurement run due to the faster decay of the ^{129}Xe amplitude.

In the next step, the weighted phase difference can be computed:

$$\Delta\Phi^{(i)} \quad = \quad \Phi_{\mathrm{He}}^{(i)} - \frac{\gamma_{\mathrm{He}}}{\gamma_{\mathrm{Xe}}} \Phi_{\mathrm{Xe}}^{(i)} \ . \tag{3.8}$$

As mentioned before, in principle, $\Delta\Phi$ is constant and independent of B_0 if there are no other sources of systematic shifts or additional interactions. But before explaining in detail the further evaluation of the weighted phase difference for a constant magnetic guiding field, the measurements using a slowly rotating magnetic guiding field are described. Though the results of these measurements did not flow into the final limits on Lorentz invariance violation, a lot of knowledge about the behavior of the comag-

[2]Even if it would occur, a jump of multiples of 2π would be easily detected later in the weighted phase difference evaluation.

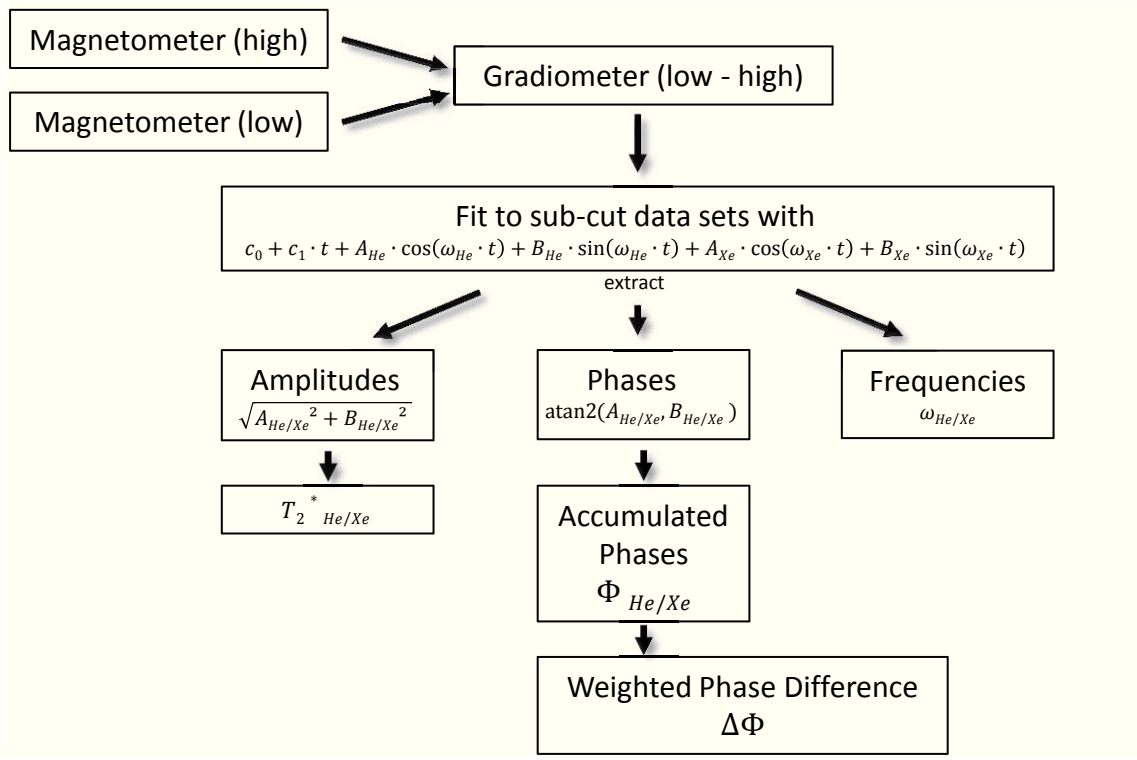

Figure 3.8: Summary of the data evaluation procedure from the SQUID raw data to the weighted phase difference $\Delta\Phi$ and other important intermediate data like signal amplitudes and relaxation time constants.

netometer, the mu-metal shielding and the measurement system etc. could be derived. Thereafter, the measurements using a static magnetic guiding field and method of data evaluation with the extraction of limits on Lorentz invariance violation are described in detail.

3.3 Evaluation and Results for a Rotating Magnetic Guiding Field

The ^{3}He-^{129}Xe comagnetometer is only sensitive if the new spin-dependent interaction in question is varying in time. In case of the search for a coupling of spins to a relic background field, the Earth's daily rotation leads to a modulation of the spin orientation in space with the sidereal frequency $\Omega_s = 2\pi/86164.101\ \mathrm{s}^{-1}$ if the direction of the magnetic guiding field is kept constant (i. e. $V = -\tilde{\boldsymbol{b}}^{\boldsymbol{n}} \cdot \boldsymbol{\sigma}^{\boldsymbol{n}} \propto \sin(\Omega_s \cdot t)$). The frequency of this modulation is unfavorably low, as the single run measurement time is comparable to the sidereal period (or even smaller). This leads to large correlations between the linear and exponential terms describing deterministic phase shifts (see p. 48) and the sinusoidal term describing the Lorentz invariance violating effect. Consequently, the correlated uncertainties on $\tilde{\boldsymbol{b}}^{\boldsymbol{n}}$ are large compared to the uncorrelated uncertainties.

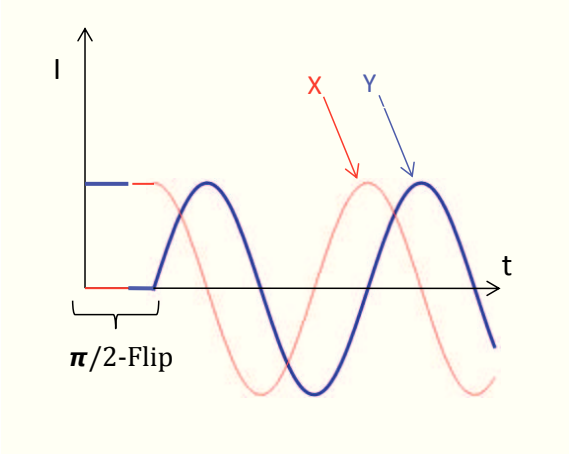

Figure 3.9: After the $\pi/2$-flip (non-adiabatic spin flip) the currents through the coils have a sinusoidal time-dependence resulting in a slow (adiabatic) rotation of the direction of the magnetic guiding field.

Therefore, it is useful to have a system that can adiabatically rotate the magnetic guiding field (for instance $\Omega_{rot} \approx 2\pi/(20\text{ min})$) in order to have a much more preferable modulation frequency ($V = -\tilde{\boldsymbol{b}}^{\boldsymbol{n}} \cdot \boldsymbol{\sigma}^{\boldsymbol{n}} \propto \sin\left((\Omega_{\text{rot}} \pm \Omega_s) \cdot t\right)$) that may help to get rid of the correlated uncertainties that limited the overall sensitivity at earlier measurements. The freely programmable current sources (see p. 41), that have been developed for the generation of the magnetic guiding field for the comagnetometer, can be used to manipulate the spins in a well-defined way. A magnetic guiding field can be generated that points into any user-defined direction in the horizontal plane with the two perpendicular Helmholtz coil pairs. In particular, the magnetic guiding field can be rotated slowly by driving two sinusoidal currents $I_x \propto \cos(\Omega_{\text{rot}} \cdot t)$ and $I_y \propto \sin(\Omega_{\text{rot}} \cdot t)$ through the x- and y-coils (see Fig. 3.9). Then the angle $\alpha = \Omega_{\text{rot}} \cdot t$ between the direction of the magnetic guiding field and the x-axis grows linearly in time.
The experiment is performed this way: The longitudinal polarized gases are brought into the magnetically shielded room while the magnetic guiding field points into the y-direction. Then the field is switched non-adiabatically into the x-direction ($\pi/2$-flip by non-adiabatic switching), which causes the magnetization to precess in the y-z-plane. Subsequently the direction of the magnetic guiding field is slowly (adiabatically) rotated by driving the corresponding sinusoidal currents through the coils. The precessing magnetization is detected by the SQUID system.

However, it turned out that the noise level inside the magnetically shielded room increases dramatically, especially at low frequencies, while the magnetic guiding field rotates. This is most likely due to the relaxation process of the innermost mu-metal shielding that adapts itself to the varying guiding field and thus can never reach equilibrium. Therefore, the measurement procedure was modified to a **step-by-step rotation** scheme: The magnetic guiding field rotates slowly for a certain amount $\Delta\alpha$ (e. g. 45° in 5 min) and then stays constant for a while (e. g. $\Delta T = 25$ min). These measurements provided a deeper insight into the behavior of the comagnetometer, the mu-metal shield-

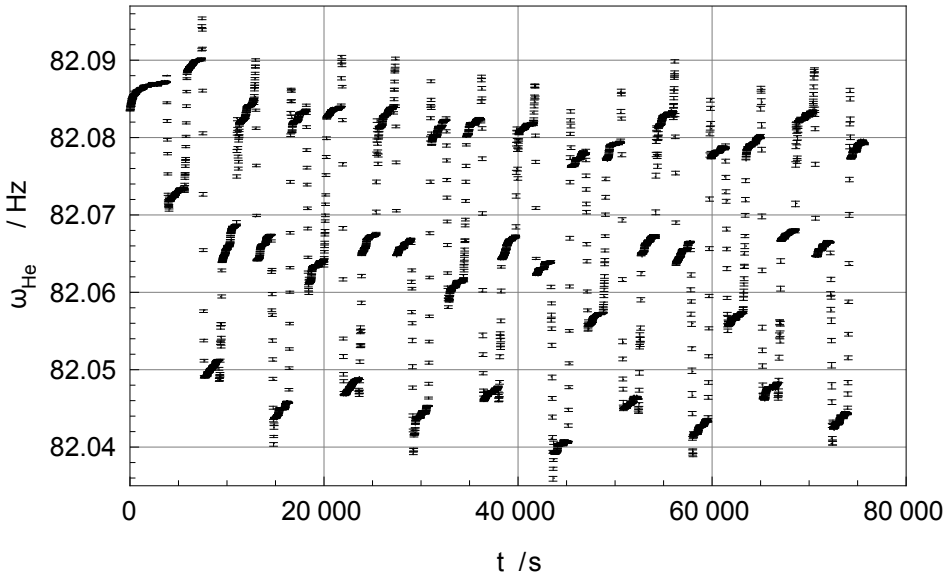

Figure 3.10: The ^{3}He Larmor frequency for a step-by-step rotating magnetic guiding field. The Larmor frequency changes faster while the magnetic guiding field rotates (almost vertical lines) and drifts slowly while the current through the coils is kept constant.

ing, and the whole measurement system that gave the possibility to derive optimization strategies for the measurements with the constant magnetic field.

3.3.1 Evaluation and Results

The first step of the data evaluation for the step-by-step rotation (the magnetic guiding field repeatedly rotates slowly for a certain amount $\Delta\alpha = 45°$ in 5 min and then stays constant for $\Delta T = 25$ min) are as described above: piecewise fitting to the sub-cuts of the gradiometer data with the extraction of Larmor frequencies, amplitudes and phases. While the magnetic guiding field rotates, the noise level is increased by a factor of 30 compared to the static case. This leads to larger uncertainties in the frequency, amplitude and phase determination.

Frequency

In Fig. 3.10 the extracted ^{3}He Larmor frequency is shown. Variations of ω_{He} are in the order of $5 \cdot 10^{-4}$ with larger drifts during the rotation. This is due to the imperfect matching of the two currents through the two coils. The Larmor frequency drifts slowly, while the current through the coils is kept constant, because the mu-metal shielding relaxes. The mu-metal adapts to the magnetic guiding field with a time constant in the order of minutes to hours.

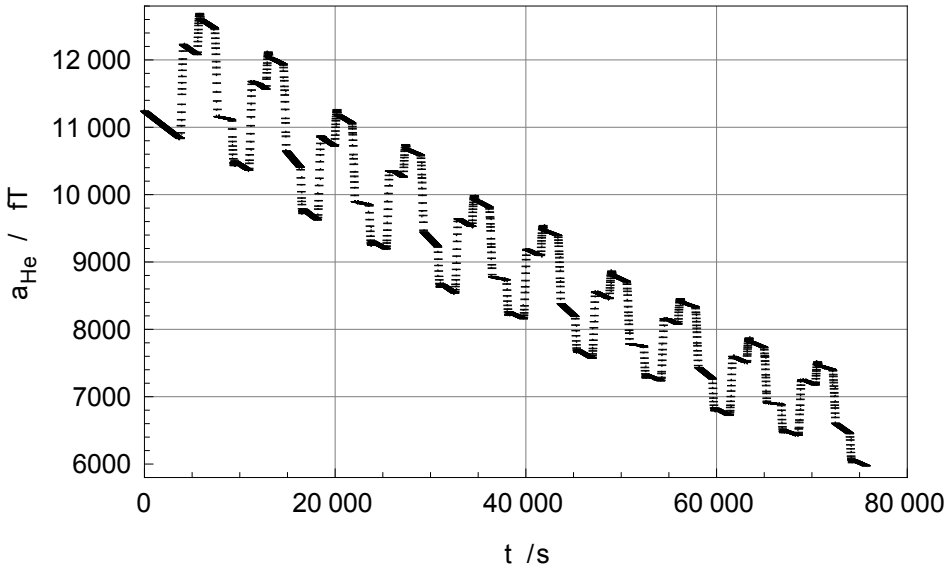

Figure 3.11: The measured ^{3}He signal amplitude for a step-by-step rotating magnetic guiding field.

Amplitude

The measured signal amplitude is shown in Fig. 3.11. The complex structure can be investigated and described as follows: During the periods of the static magnetic guiding field (about 25 minutes), the amplitude decays exponentially and the corresponding decay times $T^*_{2,\,\mathrm{He/Xe}}$ for the angles $\alpha = 0,\ \pi/4,\ \pi/2, ..., 5 \cdot 2\pi$ for five revolutions can be extracted by exponential fits to the amplitude data. The relation can be seen in Fig. 3.12, and the finding is astonishing:

The transverse relaxation time strongly depends on the direction of the magnetic guiding field and varies between 20 h and 100 h for Helium, and between 6 h and 8.5 h for Xenon (not shown). The characteristic pattern in Fig. 3.12 for $T^*_{2,He}$ repeats itself after every revolution and is reproduced in all successive runs over a period of at least two weeks. For $T^*_{2,Xe}$, the characteristic pattern is similar [40]. This effect of "incidental shimming" [61] has the following explanation: The presence of magnetic field gradients across a sample cell causes an increased transverse relaxation rate. The origin of this relaxation mechanism is the loss of phase coherence. For a spherical sample cell of radius R the relaxation rate $1/T^*_2$ is [77]

$$\frac{1}{T^*_2} = \frac{1}{T_1} + \frac{4R^4\gamma^2}{175D}\left(|\vec{\nabla}B_y|^2 + |\vec{\nabla}B_z|^2 + 2|\vec{\nabla}B_x|^2\right) \tag{3.9}$$

with the guiding field pointing into the x-direction. γ is the gyromagnetic ratio and D is the diffusion coefficient of the gas. It is useful to measure at low fields in order to minimize the absolute field gradients, which are of order pT/cm inside BMSR-2. There are two main sources of gradients: Residual field gradients from the mu-metal shielding

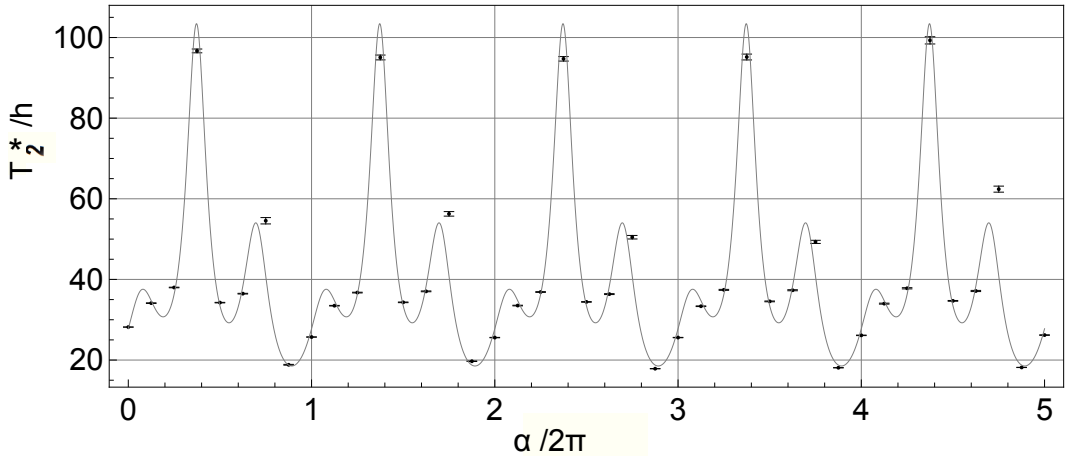

Figure 3.12: The transverse relaxation time of helium as a function of the direction α of the magnetic guiding field in the horizontal plane, measured in steps of $\Delta\alpha = 45°$ for 5 turns. In total, the measurement took about 20 hours with ∼30 min for each field setting to extract the T_2^* from the decay of the signal amplitude. Solid line: Fit of a Fourier series to the relaxation rates $1/T_2^*$.

and gradients produced by the Helmholtz coils. The latter ones will change, as the magnetic guiding field is rotated. At some angle α, the gradients from the chamber and coils almost cancel each other and T_2^* is maximized. At other angles the cancellation is less distinct with a minimum in T_2^* at a field orientation where the gradients add up constructively. This is consistent with the observation that by rotating the magnetic guiding field by 180° the transverse relaxation time goes from the global maximum to the global minimum. That result gives the possibility to choose the direction of the static magnetic guiding field accordingly in order to achieve long measurement times of coherent spin precession.
To come back to the investigation and description of the complex shape of the structure in Fig. 3.11: The magnetization M (proportional to the polarization) inside the sample cell decreases with time due to the exponential decay with a rate that depends on the angle $\alpha(t)$:

$$M(t) = M_0 \cdot \exp\left[\int_0^t \frac{dt'}{T_2^*(\alpha(t'))}\right] . \tag{3.10}$$

In practice, $T_2^*(\alpha)$ can be estimated by fitting a Fourier series to the relaxation rates $1/T_2^*(\alpha = 0,\ \pi/4,\ \pi/2, ..., 5 \cdot 2\pi)$ (see Fig. 3.12).
The measured amplitude (the magnetic flux through the SQUID area) $a(t)$ can be expressed by

$$a(t) = a_0 \cdot S(\alpha(t)) \cdot \exp\left[\int_0^t \frac{dt'}{T_2^*(\alpha(t'))}\right] \tag{3.11}$$

with a factor $S(\alpha(t))$ that takes into account geometric effects depending on the position of the SQUID with respect to the center of the sample cell and the direction of the magnetic guiding field. In general, the SQUID sensor is not exactly on top of the center of the cell, but displaced to an off-center position. The position can be parameterized in cylindrical coordinates: The vertical distance from the center of the sample cell to the SQUID is z_S, the horizontal distance r_S and the angle in the horizontal plane between the x-axis and the line connecting cell center and SQUID φ_S.
The influence of the SQUID position and α on the measured amplitude $a(t)$ can be explained with the help of Fig. 3.13: A SQUID with $r_S = 0$ measures the maximal signal when the magnetization vector $\boldsymbol{M}$ is parallel to the z-axis (directly pointing at the detector), and correspondingly a minimal signal when $\boldsymbol{M}$ is anti-parallel to the z-axis. This occurs for every direction α of the magnetic guiding field in the x-y-plane, so $S(\alpha) = const.$ for a SQUID with $r_S = 0$ (directly above the center of the sample cell). However, for an off-centered SQUID the magnetization vector $\boldsymbol{M}$ can only point directly at the SQUID if it lies in the precession plane.[3] This is the case for $\alpha - \varphi_S = \pm\pi/2$ (for SQUID 1 and SQUID 2 on the left side of Fig. 3.13; and for SQUID 3 on the right side of Fig. 3.13). For other angles, the measured amplitude is smaller and reaches a minimum for $\alpha - \varphi_S = 0, \pi$.

In principle $S(\alpha)$ can be calculated if the SQUID position with respect to the center of the sample cell is known (see Appendix B on page 141). On the other hand, if $S(\alpha)$ is known precisely enough by measurements, then the relative SQUID position can be deduced. Rewriting Eq. (3.11) leads to:

$$\begin{aligned} a_{\mathrm{corr}}(\alpha) &:= a_0 \cdot S(\alpha) \\ &= a(t) \cdot \exp\left[- \int_0^t \frac{dt'}{T_2^*(\alpha(t'))} \right] . \end{aligned} \tag{3.12}$$

On the right side of this equation there are measured quantities, so that $a_{\mathrm{corr}}(\alpha) = a_0 \cdot S(\alpha)$ can be calculated from the experimental data and plotted. The result is shown in Fig. 3.14 for an almost centered SQUID and two strongly off-centered SQUIDs. As expected, the almost centered SQUID shows the maximum amplitude with only little dependence on α. For the off-centered SQUIDs a_{corr} strongly depends on α (with opposing trends, similar to SQUID 1 and SQUID 3 in Fig. 3.13). This can be used to measure the position of the sample cell with respect to the SQUID system and subsequently the magnitude of $\boldsymbol{M}$. In the next section this information is used to estimate phase shifts due to the Ramsey-Bloch-Siegert shift ("cross-talk").

The weighted phase difference

The measured weighted phase difference is shown in Fig. 3.15. The complex structure can be described as follows: The influence of Earth's rotation (see Eq. (2.46) on p. 49) in this case is not a simple linear drift, but changes with the angle ρ between the

[3] On a closer look the signal is not maximal when the magnetization vector points directly at the off-centered SQUID, but for a slightly shifted angle. This is discussed in detail in Appendix B on page 141.

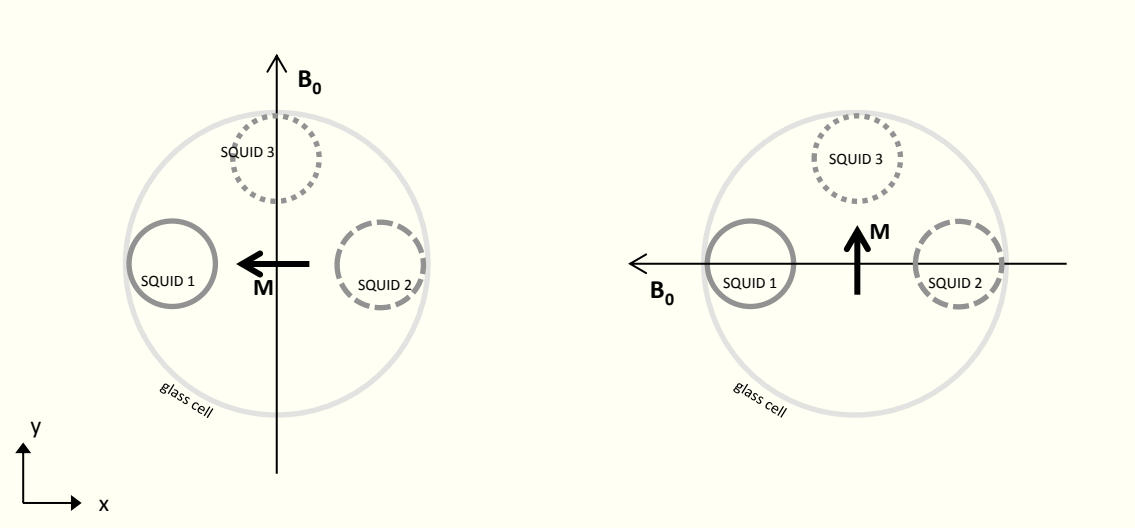

Figure 3.13: Illustration of geometric effects concerning the measured amplitudes (subsumed in $S(\alpha)$) and phases. Top-view onto the spherical sample cell with three off-centered SQUIDs with positions $r_S \neq 0$ at $\varphi_{S,1} = \pi$ for SQUID 1, $\varphi_{S,2} = 0$ for SQUID 2 and $\varphi_{S,3} = \pi/2$ for SQUID 3 with $\alpha = \pi/2$ (left) and $\alpha = \pi$ (right). Left: The magnetic guiding field is aligned parallel to the y-axis and thus the magnetization $\boldsymbol{M}$ precesses in the x-z-plane and SQUIDs 1 and 2 measure a higher signal (but different phases). Right: The magnetic guiding field is aligned anti-parallel to the x-axis and thus the magnetization $\boldsymbol{M}$ precesses in the y-z-plane and SQUID 3 measures a higher signal (but now SQUID 1 and 2 measure the same phase).

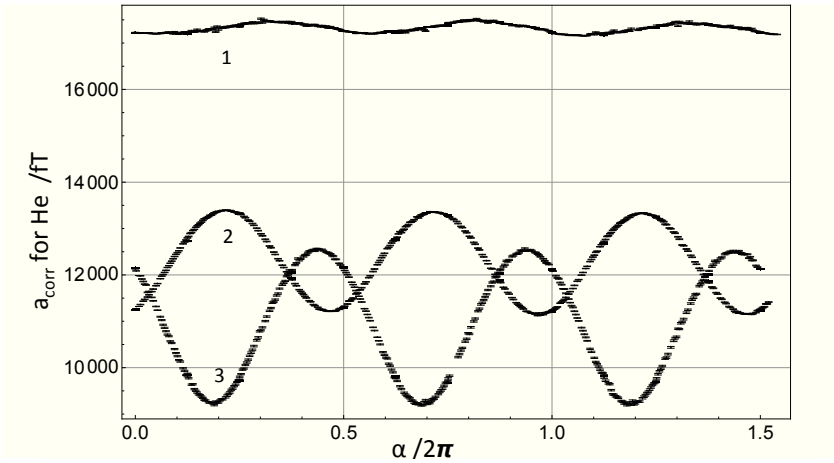

Figure 3.14: $a_{\mathrm{corr}}(\alpha) = a_0 \cdot S(\alpha)$ calculated from the measurement data according to Eq. (3.12) for (1) an almost centered SQUID and (2, 3) two strongly off-centered SQUIDs, arranged at $(\varphi_{S,2} - \varphi_{S,3} \approx \pi/2)$. As expected, the almost centered SQUID shows the maximum amplitude with only little dependence on α. For the off-centered SQUIDs a_{corr} strongly depends on α.

direction of the magnetic guiding field and the North-South-direction:

$$\begin{aligned} \omega_{\mathrm{det}}(t) &= \Omega_E \cos(\Theta)\cos(\rho(t)) \\ \Rightarrow \Delta\Phi_{\mathrm{det}}(t) &= \left(1 - \frac{\gamma_{\mathrm{He}}}{\gamma_{\mathrm{Xe}}}\right) \Omega_E \cos(\Theta) \int_0^t \cos(\rho(t'))dt' \ . \end{aligned} \tag{3.13}$$

$\rho(t)$ in turn depends on $\alpha(t)$ and has to be known very precisely in order to correct for Earth's rotation.
Similar to the geometric effects concerning the measured amplitude, the measured phase depends on the SQUID position and α and has to be accounted for:
The effect can be explained using Fig. 3.13: If the magnetic guiding field is aligned parallel to the y-axis (left side of the figure), then the magnetization $\boldsymbol{M}$ precesses in the x-z-plane and SQUIDs 1 and 2 measure different phases. SQUID 2 measures the maximum signal earlier in time than SQUID 1. The difference in phases is roughly $\Delta\varphi = \varphi_{S,2} - \varphi_{S,1} = \arctan(r_{S,2}/z_{S,2}) + \arctan(r_{S,1}/z_{S,1})$. Inverting $\boldsymbol{B_0}$ changes the sign of $\Delta\varphi$. However, if the magnetic guiding field is aligned anti-parallel to the x-axis (right side of the figure), then the magnetization $\boldsymbol{M}$ precesses in the y-z-plane and SQUID 1 and 2 measure the same phase.
The general case is discussed in Appendix B on page 141 and leads to a Fourier series (with the additional term describing the Earth's rotation):

$$\begin{aligned} \Delta\Phi_{\mathrm{c}}(t) = \Delta\Phi_{\mathrm{det}}(t) + a_0 + a_1 \cdot t &+ c_1 \cdot \sin(\alpha(t)) + d_1 \cdot \cos(\alpha(t)) \\ &+ c_2 \cdot \sin(2\alpha(t)) + d_2 \cdot \cos(2\alpha(t)) \\ &+ \ ... \end{aligned} \tag{3.14}$$

If $r_S \ll z_S$, then only the $c_1 \cdot \sin(\alpha(t)) + d_1 \cdot \cos(\alpha(t))$ term of the Fourier series contributes. In Fig. 3.16 the residuals of the weighted phase difference after subtraction of the

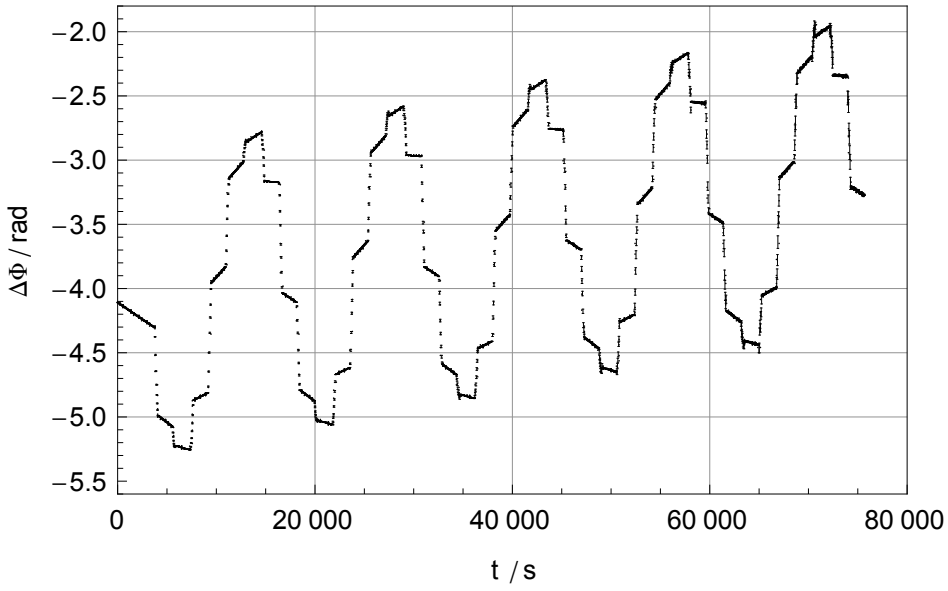

Figure 3.15: The weighted phase difference $\Delta\Phi$ for a step-by-step rotating magnetic guiding field.

Earth's rotation and geometric effects are shown. The structures are reduced by many orders of magnitude, but obviously the residuals are not Gaussian distributed. The main reason for the structure in the order of a few mrad is the large uncertainty on $\rho(t)$ as the alignment of the experimental setup within the magnetically shielded room with respect to the North-South-direction could only be measured with an accuracy of about 1°. Additionally, the currents through the two Helmholtz coil pairs do not fully determine the direction of the magnetic guiding field, as the innermost mu-metal layer reacts to the field configuration. In this case the total magnetic field (superposition of the field produced by the coils and by the mu-metal) drags behind the field produced by the coils. This effect can be seen in Fig. 3.10 on p. 72: The magnetic guiding field (and the Larmor frequency) increases while the currents through the coils are kept constant.

3.3.2 Conclusion

Due to these large uncertainties in deterministic phase shifts, no competitive limits on Lorentz invariance violation were extracted. Besides the proof of principle that a coherent measurement of spin precession with a slowly rotating guiding field is possible (i.e. the phase information is conserved), the results have an unexpected impact on the measurements with static guiding fields: The results gave the possibility to optimize T_2^* and thus the observation time for the search for a Lorentz violating coupling of spins to a hypothetical background field. In the present experiments coherent spin precession can be monitored for more than 24 hours ($\approx 3 \cdot T_{2,Xe}^*$). Longer observation times T cause a

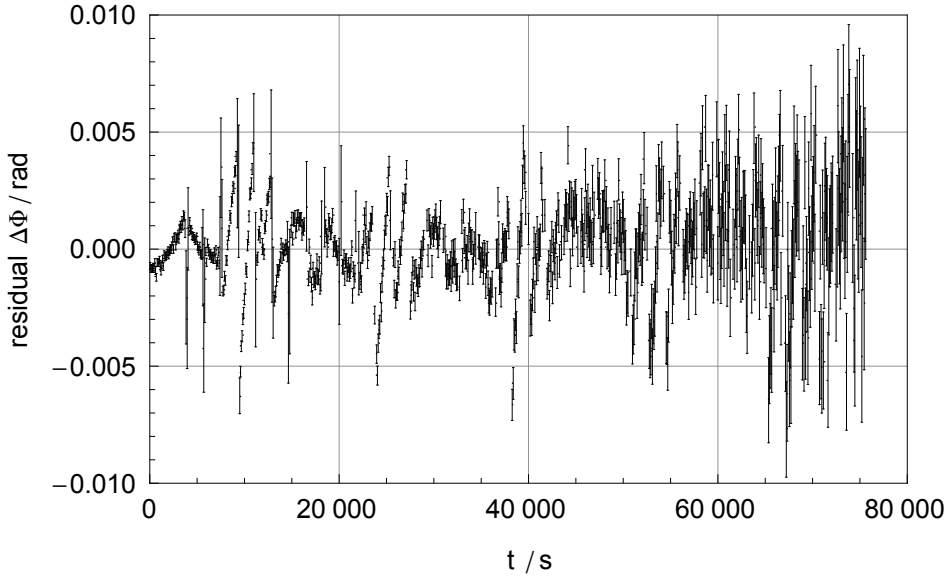

Figure 3.16: The residuals of the weighted phase difference after subtraction of the Earth's rotation and geometric effects according to Eq. (3.14).

higher sensitivity in frequency measurement ($\sigma \propto T^{-3/2}$) according to the Cramer-Rao Lower Bound (see next section) and, furthermore, greatly reduce the correlated errors, especially if runs of coherent spin precession are substantially longer than the period of a sidereal day.

3.4 Evaluation and Results for a Static Magnetic Guiding Field

The results of the measurements with a step-by-step rotating magnetic guiding field gave the possibility to choose a direction α with low gradient relaxation and thus a large T_2^* (see Fig. 3.12) with $T^*_{2,\,\mathrm{He}} \approx 100$ h and $T^*_{2,\,\mathrm{Xe}} \approx 8.5$ h. In total 7 measurement runs ($j = 1, \ldots, 7$) with free spin precession of ^{3}He and ^{129}Xe and a static magnetic guiding field were performed, each lasting about one day ($\approx 3 \cdot T^*_{2,\,\mathrm{Xe}}$). The direction of the magnetic guiding field was $\alpha = 0$ for runs j=1, 2, 3 and $\alpha = 3/4\pi$ for runs $j = 4, \ldots, 7$. The corresponding angle between the magnetic guiding field and the north-south direction was $\rho_1 = 208°$ for runs j=1, 2, 3 and $\rho_2 = 73°$ for runs $j = 4, \ldots, 7$.
The first steps of the data evaluation are described in Section 3.2 on page 61: piecewise fitting to the sub-cuts of the gradiometer data with the extraction of Larmor frequencies, amplitudes and phases. The data of four independent gradiometers have been used to finally extract the limits on Lorentz invariance violation. The lower SQUIDs of these gradiometers were in the proximity of the sample cell and, thus, had the strongest signals. The correlation of the gradiometer noise was close to zero, so that by using four gradiometers the overall signal-to-noise ratio improved by a factor of two.[4]
In the following sections, the data evaluation procedure and the final extraction of the parameters describing the Lorentz invariance violating effect will be presented.

3.4.1 Estimation of the Cross-Talk Amplitude

In Section 2.5.2 on p. 50 the Ramsey-Bloch-Siegert shift was described with the cross-talk as a special case. The cross-talk emerges if there are two ore more different spin species co-located in the same volume. In this case the cross-talk describes the shift due to the influence of the precessing magnetization of the ^{3}He nuclei on the ^{129}Xe precession frequency (and vice-versa). The ^{3}He and ^{129}Xe magnetizations produce homogeneous rotating magnetic fields B_1 inside the spherical glass cell that influence the other spin species. The time evolution is described by the two exponential terms with time constants $\frac{1}{2}T^*_{2,Xe}$ and $\frac{1}{2}T^*_{2,He}$. This shift is small compared to the other deterministic phase shifts, as B_1 is about 100 pT, typically. The actual measurements in recent times achieved such a high sensitivity that it has to be considered during the data evaluation procedure with the term:

$$\Delta\Phi^{\mathrm{ct}}_{\mathrm{RBS}}(t) \;=\; F_{He} \cdot e^{-\frac{2\cdot t}{T^*_{2,Xe}}} + F_{Xe} \cdot e^{-\frac{2\cdot t}{T^*_{2,He}}} \quad .$$

The amplitudes of the cross-talk

$$\begin{aligned} F_{He} &= \frac{\gamma^2_{He} B^2_{1,Xe}(0) \cdot T^*_{2,Xe}}{4\Delta\omega} \\ F_{Xe} &= \frac{\gamma_{He}\gamma_{Xe} B^2_{1,He}(0) \cdot T^*_{2,He}}{4\Delta\omega} \end{aligned} \tag{3.15}$$

can be estimated if the the field inside the cell at the beginning of the measurement $B_1(t = 0)$ is known. The estimated values (expectation values) are denoted by $\hat{F}_{\mathrm{He}}$ and

[4] This is investigated in Appendix A.2 on p. 129.

$\hat{F}_{\mathrm{Xe}}$. In practice, the magnetic field inside the sample cell can be determined by measuring the magnetic dipole field outside the spherical sample cell at different positions and then using the well-known result from magneto-statics:
A uniformly magnetized sphere of radius R and magnetization $\boldsymbol{M}$ produces a homogeneous magnetic field $\boldsymbol{B}_{in} = \frac{2\mu_0}{3}\boldsymbol{M}$ inside the sphere. The field outside the sphere is the field of a dipole $\boldsymbol{m} = \frac{4\pi R^3}{3}\boldsymbol{M}$ at the center of the sphere. This result can be found in [50], for example. The strength of the homogeneous field within the spherical sample cell corresponds to the strength of the dipole field at the intersection point of the dipole axis with the surface of the sphere.
For example, if there are two magnetometers exactly above the center of the sphere (aligned along the z-axis) the determination is simple, even with an unknown distance x from the lower magnetometer to the center of the sample cell, if the distance b (usually $b = 7$ cm) between those magnetometers is known: The lower magnetometer measures a field B_{low} at a distance x to the center of the sample cell, and the higher magnetometer measures a field B_{high} at a distance $x + b$ to the center of the sample cell. Due to the $B \sim 1/r^3$ relation of the dipole field:

$$\begin{aligned} \frac{B_{\mathrm{low}}}{B_{\mathrm{high}}} &= \frac{(b+x)^3}{x^3} \\ \Rightarrow x &= \frac{b}{\left(\frac{B_{\mathrm{low}}}{B_{\mathrm{high}}}\right)^{1/3} - 1} \,. \end{aligned} \tag{3.16}$$

Subsequently, the strength of the field inside the cell B_{in} can be calculated according to

$$B_{\mathrm{in}} = B_{\mathrm{low}} \cdot \frac{x^3}{R^3} \tag{3.17}$$

where R is the radius of the spherical sample cell. For magnetometers that are not exactly above the center of the cell the calculation can be found in Appendix B.
This procedure can be repeated for different pairs of magnetometers. The resulting values for B_1 vary in the range of 5%. Thus, 5% is used as an uncertainty estimation on B_1, resulting in uncertainties σ_{F} on F_{He} and F_{Xe} in the order of 10%. The transverse relaxation times and the difference in Larmor frequencies can be determined very precisely and therefore do not contribute to the uncertainties on F_{He} and F_{Xe}.
The strength of the homogeneous magnetic field inside the cell B_1 and transverse relaxation times with the corresponding cross-talk amplitudes can be found in Tab. 3.1.
Those values $\hat{F}_{\mathrm{He}}$ and $\hat{F}_{\mathrm{Xe}}$ together with their uncertainties $\sigma_{\mathrm{F,\,He}}$ and $\sigma_{\mathrm{F,\,Xe}}$ are later used as an estimate for the actual cross-talk amplitudes F_{He} and F_{Xe}.

3.4.2 Fitting Procedure and Results

The seven sequential measurement runs are evaluated in a combined fit. Therefore the weighted phase difference data of the individual runs was merged into a single data set with the corresponding timing information. $t_{0,j}$ is the starting time of the run (j) (with t=0 at 15:35 UT on March 7th, 2012)[5]. The combined weighted phase difference data

[5] At $t = t_{0,1} = 0$ the local sidereal time was 2.5 h, which results in a sidereal phase of $\varphi_s = 0.104 \cdot 2\pi$. Further information on sidereal time, on the coordinate systems and transformations that are used in this work can be found in Appendix A.1 on p. 127.

Run j	$\hat{F}_{\mathrm{Xe}}$ /mrad	T_2^{He} /s	B_1^{He} /pT	$\hat{F}_{\mathrm{He}}$ /mrad	T_2^{Xe} /s	B_1^{Xe} /pT
1	360	94660	229	8	25180	77
2	620	134000	252	5	26730	64
3	70	98300	99	2.3	25260	22
4	1130	271500	239	2.7	28230	22
5	320	284340	124	1.0	25600	15
6	2140	303730	311	7	26250	72
7	740	291980	187	5	24690	70

Table 3.1: The amplitudes F_{He} and F_{Xe} of the Ramsey-Bloch-Siegert shift (cross-talk). The uncertainties on F_{He} and F_{Xe} are about 10% due to the 5% uncertainties on B_1^{Xe} and B_1^{He}. The relaxation times and the difference in Larmor frequencies can be determined very precisely ($\delta T_2^* = 10$ s and $\delta\Delta\omega < 10^{-5}$ Hz).

after subtraction of estimated linear terms $\Delta\Phi_{\mathrm{lin}}$ can be found in Fig. 3.17 (top). These estimated linear terms are dominated by the Earth's rotation (several rad per day) and have been subtracted for better representation of the occurring structures in the weighted phase difference. The remaining parabolic structure is caused by the Ramsey-Bloch-Siegert shift (mainly the self-shift, after subtraction of the linear term from an exponential term, the quadratic and higher order terms remain). Note the change of sign of the self-shift from run $j = 4$ on where the direction of the magnetic guiding field was changed (with major differences in the resulting field gradients).
If there is no sidereal variation of the ^{3}He and ^{129}Xe frequencies induced by Lorentz invariance violating couplings, then the time dependence of the weighted phase difference can be described best by the fit model

$$\Delta\Phi_{\mathrm{c}}(t) = \begin{cases} \Delta\Phi_{\mathrm{d}}^{(1)}(t) & \text{for } t_{0,1} \le t \le (t_{0,1} + N_1 \cdot \tau) \\ \qquad\vdots & \\ \Delta\Phi_{\mathrm{d}}^{(7)}(t) & \text{for } t_{0,7} \le t \le (t_{0,7} + N_7 \cdot \tau) \end{cases} \tag{3.18}$$

with

$$\begin{aligned} \Delta\Phi_{\mathrm{d}}^{(j)}(t) \;=\; & \Phi_0^{(j)} + \Delta\omega_{\mathrm{lin}}^{(j)} \cdot (t - t_{0,j}) + E_{\mathrm{He}}^{(j)} \cdot e^{\frac{-\left(t-t_{0,j}\right)}{T_{2,\mathrm{He}}^{*\,(j)}}} + E_{\mathrm{Xe}}^{(j)} \cdot e^{\frac{-\left(t-t_{0,j}\right)}{T_{2,\mathrm{Xe}}^{*\,(j)}}} \\ & + F_{\mathrm{Xe}}^{(j)} \cdot e^{\frac{-2\left(t-t_{0,j}\right)}{T_{2,\mathrm{He}}^{*\,(j)}}} + F_{\mathrm{He}}^{(j)} \cdot e^{\frac{-2\left(t-t_{0,j}\right)}{T_{2,\mathrm{Xe}}^{*\,(j)}}} \end{aligned} \tag{3.19}$$

where N_j is the number of sub-cuts in run j (thus, $N_j \cdot \tau$ is the measurement time of run j).

So far, the fitting of the combined fit function in Eqs. (3.18) and (3.19) to the combined data would decompose into single fits of $\Delta\Phi_{\mathrm{d}}^{(j)}(t)$ to the data of individual runs, as the parameters describing the constant, the linear and the four exponential terms ($\Phi_0^{(j)}$, $\Delta\omega_{\mathrm{lin}}^{(j)}$, $E_{\mathrm{He/Xe}}^{(j)}$ and $F_{\mathrm{He/Xe}}^{(j)}$) have to be adjusted for each run anew. These parameters may vary, because the partial pressures of the gas mixture, and gradients and exact orientation of the magnetic guiding field may vary from run to run.
However, the combined fit to the combined data is necessary for the extraction of the hypothetical background field which would be the same for all seven measurement runs. The combined fit to the data of all 7 runs now including the parameterization of the sidereal phase modulation due to the Lorentz invariance violating interaction was performed with

$$\Delta\Phi_{\mathrm{fit}}(t) = \Delta\Phi_{\mathrm{c}}(t) + \begin{cases} \sin\chi_1 \left(e_x \cdot \sin(\Omega_s t + \varphi_1) + e_y \cdot \cos(\Omega_s t + \varphi_1)\right), \text{for } j \leq 3 \\ \sin\chi_2 \left(e_x \cdot \sin(\Omega_s t + \varphi_2) + e_y \cdot \cos(\Omega_s t + \varphi_2)\right), \text{for } j \geq 4 \end{cases} . \tag{3.20}$$

Here e_x and e_y are global fit parameters, whereas $\sin\chi_{1/2}$ and $\varphi_{1/2}$ are constants that account for the different measurement sensitivities and phases (with respect to the x- and y-components of the hypothetical background field) for the two directions of the magnetic guiding field (the corresponding angle between the magnetic guiding field and the north-south direction was $\rho_1 = 208°$ for runs j=1, 2, 3 and $\rho_2 = 73°$ for runs j = 4, ..., 7, while the latitude $\Theta = 52.52°$ was constant). The usual choice of coordinate frames and transformations was made as recommended in Ref. [27, pp. 7-9] and the corresponding calculations can be found in Appendix A.1 on p. 127, resulting in:

$$\begin{aligned} \chi &= \arccos(\cos\Theta\cos\rho) \\ \sin\chi_1 &= 0.84 \\ \sin\chi_2 &= 0.98 \end{aligned} \tag{3.21}$$

and with the sidereal phase of $\varphi_s = 0.104 \cdot 2\pi$ at $t = 0$:

$$\begin{aligned} \varphi &= \arctan(-\tan\rho/\sin\Theta) + \varphi_s \\ \varphi_1 &= 0.103 \\ \varphi_2 &= -0.677 \ . \end{aligned} \tag{3.22}$$

Fitting Procedure

To simplify the explanation, first the fitting procedure to the data of a single gradiometer will be discussed. Later this will be expanded to the simultaneous fitting to the data of several gradiometers.
The fit function in Eqs. (3.20) together with (3.19) and (3.20) has the four free fit parameters $\Phi_0^{(j)}, \Delta\omega_{\mathrm{lin}}^{(j)}, E_{\mathrm{He}}^{(j)}, E_{\mathrm{Xe}}^{(j)}$ for each run, and the two fit parameters $F_{\mathrm{He}}^{(j)}$ and $F_{\mathrm{Xe}}^{(j)}$ per run with independently determined expectation values $\hat{F}_{\mathrm{He}}^{(j)}$ and $\hat{F}_{\mathrm{Xe}}^{(j)}$ and uncertainties $\sigma_{\mathrm{F,\,He}}^{(j)}$ and $\sigma_{\mathrm{F,\,Xe}}^{(j)}$ from the amplitude measurements, and additionally the two free

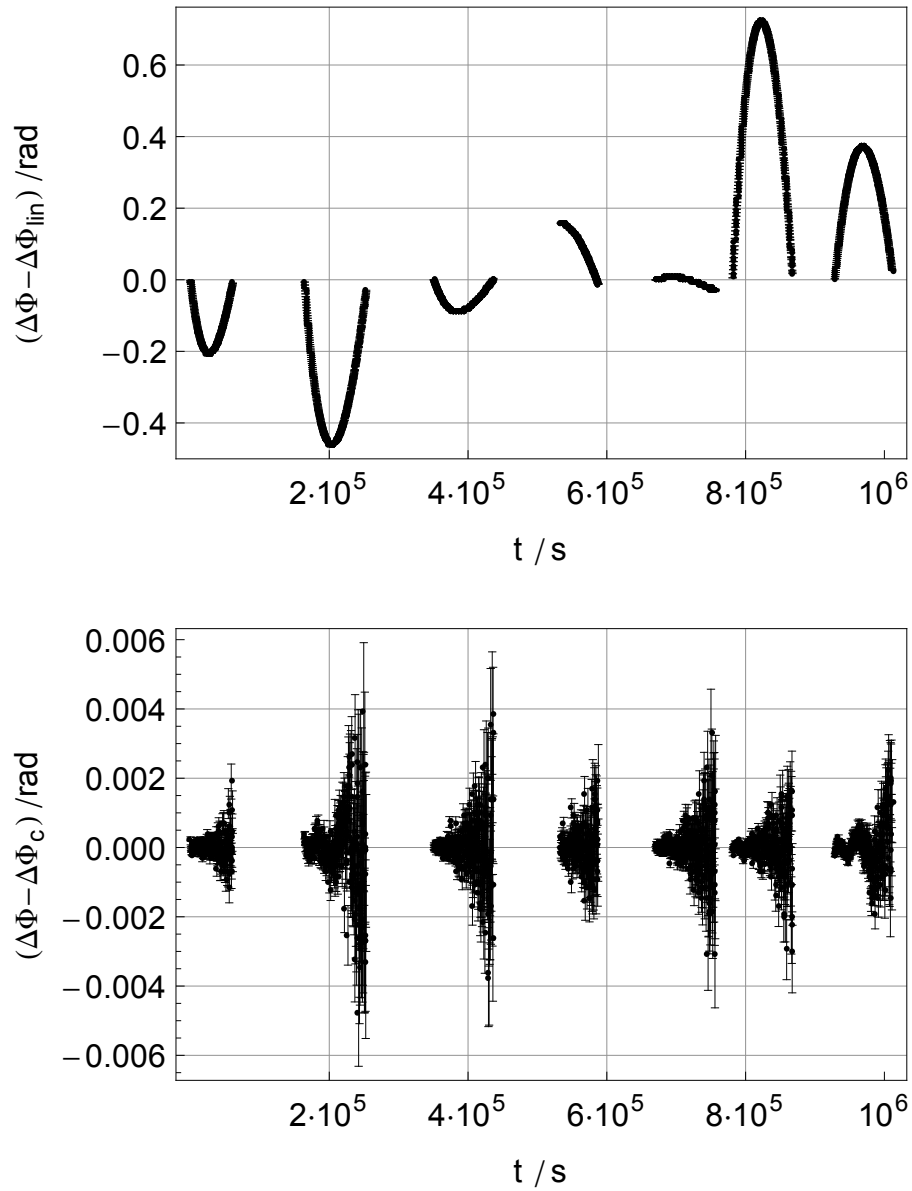

Figure 3.17: Top: Weighted phase difference $\Delta\Phi$ (data-bin: 320 s) for all seven runs (single gradiometer data) after subtraction of estimated linear terms $\Delta\Phi_{\text{lin}}$ (dominated by the Earth's rotation) for better representation. The remaining parabolic shaped structure is the contribution of the RBS-shift (in particular the self-shift). Note that the phase noise is much less than the symbol size.
Bottom: The phase residuals after subtraction of the entire fit-model $\Delta\Phi_c$ according to Eqs. (3.18),(3.19) and (3.20). The increase of the phase noise is caused by the exponential decay of the signal amplitudes.

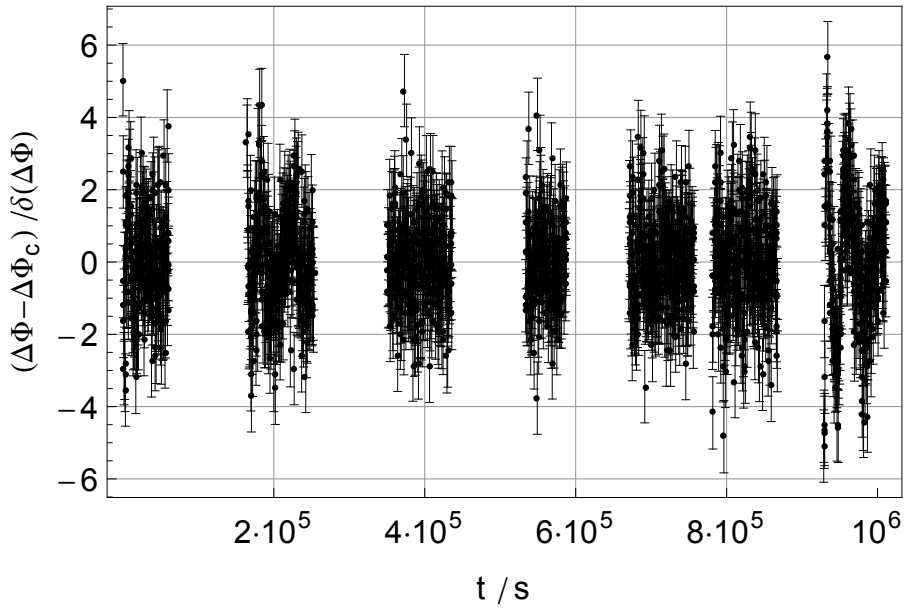

Figure 3.18: Weighted phase difference after subtraction of the entire fit-model $\Delta\Phi_c$ according to Eqs. (3.18), (3.19) and (3.20) divided by the phase uncertainty to detect possible structures in the residuals. The normalized residuals should be Gaussian distributed around zero with $\sigma = 1$.

global fit parameters e_x and e_y. In contrast, the transverse relaxation times $T_2^{*(j)}$ can be determined independently with high precision for both spin species from the experiment by fits to the decaying amplitudes.
In total these are $p = 44$ fit parameters. On 14 of these parameters there is additional information available. Taking into account the additional information on $F_{\mathrm{He}}^{(j)}$ and $F_{\mathrm{Xe}}^{(j)}$, the fitting procedure was not a basic χ^2-minimization, but a maximization of the likelihood $L(\boldsymbol{a})$ including the Gaussian probability distributions for $F_{\mathrm{He}}^{(j)}$ and $F_{\mathrm{Xe}}^{(j)}$:

$$L(\boldsymbol{a}) \;=\; \text{Norm.} \cdot \exp\left[-\frac{1}{2}\chi^2(\boldsymbol{a})\right] \cdot \prod_{\substack{j \\ s=\mathrm{He,Xe}}} \exp\left[-\frac{1}{2}\left(\frac{F_{\mathrm{s}}^{(j)} - \hat{F}_{\mathrm{s}}^{(j)}}{\sigma_{\mathrm{F,\,s}}^{(j)}}\right)^2\right], \tag{3.23}$$

with the vector $\boldsymbol{a}$ including all the 44 fit parameters and

$$\text{Norm.} \;=\; \prod_{i=1}^{N} \frac{1}{\sigma_i \cdot \sqrt{2\pi}} \cdot \prod_{\substack{j \\ s=\mathrm{He,Xe}}} \frac{1}{\sigma_{F,s}^{(j)} \cdot \sqrt{2\pi}} \tag{3.24}$$

is the proper normalization factor, which is of no further importance.
Here χ^2 is defined as usual as

$$\chi^2(\boldsymbol{a}) \;=\; \sum_{i=1}^{N} \left[\frac{1}{\sigma_{y,i}}\left(y_i - f(t_i;\boldsymbol{a})\right)\right]^2 \tag{3.25}$$

with the fit function f and the data-points (t_i, y_i) with an uncertainty $\sigma_{y,i}$ on y_i. N is the number of data-points (in this experiment: $N \approx 2 \cdot 10^5$).
In the case of Eq. (3.23), the maximization of $L(\boldsymbol{a})$ is equivalent to the minimization of

$$\chi'^2(\boldsymbol{a}) \;=\; \chi^2(\boldsymbol{a}) + \sum_j \left[\left(\frac{F_{\mathrm{He}}^{(j)} - \hat{F}_{\mathrm{He}}^{(j)}}{\sigma_{\mathrm{F,\,He}}^{(j)}}\right)^2 + \left(\frac{F_{\mathrm{Xe}}^{(j)} - \hat{F}_{\mathrm{Xe}}^{(j)}}{\sigma_{\mathrm{F,\,Xe}}^{(j)}}\right)^2\right] . \tag{3.26}$$

In words, the additional information on $F_{\mathrm{He/Xe}}^{(j)}$ can be treated similar to 14 additional data-points included in the calculation of χ^2. Thus, the fit parameter $F_{\mathrm{He/Xe}}^{(j)}$ can be adjusted to the actual value of the cross-talk amplitude (driven by the $N \approx 2 \cdot 10^5$ data-points), even if the estimations $\hat{F}_{\mathrm{He/Xe}}^{(j)}$ are not precise.
The main advantage of using the additional information on $F_{\mathrm{He}}^{(j)}$ and $F_{\mathrm{Xe}}^{(j)}$ is the great reduction of correlation in the fitting results, especially between the amplitudes of the four exponential terms.
As the signal-to-noise ratio can be increased by using multiple gradiometers with uncorrelated noise, the final data evaluation was performed with the data of four independent gradiometers to extract limits on the Lorentz invariance violating coefficients. The individual data sets were merged into a single one, now containing all seven runs and four gradiometers. To do so, a pseudo-dimension g was added as an independent variable to denote the gradiometer number ($g = 1, 2, 3, 4$), so that the data points now have the form $(t_i, g, \Delta\Phi_i, \delta\Delta\Phi_i)$, i. e. the weighted phase difference $\Delta\Phi$ and the corresponding

uncertainty $\delta\Delta\Phi$ as a function of time t_i and gradiometer number g. Then parameters had to be added to the fit model: The constant term $\Phi_0^{(j)}$ accounts for a general phase offset that depends on the exact position of the gradiometer with respect to the sample cell. Thus, the single constant term had to be substituted by four gradiometer dependent terms $\Phi_0^{(g,j)}$. The linear and exponential terms in the fit model account for effects that do not depend on the SQUID position (i. e. Ramsey-Bloch-Siegert shift, Earth rotation, etc.) and, thus, must be the same for all gradiometers (but, of course, may change from run to run). All in all these are $9 \cdot 7 + 2 = 65$ free parameters in the fit model.
Finally, a fit of the function in Eqs. (3.20) together with (3.19) and (3.20) to the combined data of all seven runs and four gradiometers was performed, i.e. minimizing χ'^2 by varying the 65-dimensional vector $\boldsymbol{a}$, in this case with $\approx 8 \cdot 10^5$ data points. The fit was performed using Mathematica with the "DatFit" package of U. Schmidt (which was originally developed for the data evaluation of Neutron Resonance Spin Echo experiments, and later for the torsion pendulum experiment [22, 23] with a similar data evaluation procedure and corresponding requirements). Here the challenge is to guarantee numerical stability with the large number of data points, and valid estimates of parameters that are highly correlated in this case (especially the exponential terms have a high correlation). As a result, values for the fit parameters together with their correlated and uncorrelated uncertainties are extracted. Additionally, $\chi'^2/d.o.f.$ as a measure of the goodness of the fit, and the correlations of the fit parameters (in the form of a 65×65 matrix) can be evaluated. In this case $\chi'^2/d.o.f. = 1.51$, and the largest correlations occur between the four exponential terms of a single run. These correlations are typically -0.999 if one neglects the additional information on $F_{\mathrm{He}}^{(j)}$ and $F_{\mathrm{Xe}}^{(j)}$, but can be brought to -0.92 by including this information.
In Fig. 3.17 (top) the weighted phase difference for a single gradiometer is shown and in (bottom) the corresponding residuals after subtraction of the fitted function. The structures are reduced by more than three orders of magnitude. As the phase noise increases with time, it is easier to find structures in the residuals by looking at the "normalized residuals" in Fig. 3.18 (the residuals divided by the corresponding uncertainty).

Results

From the fit, the sidereal phase amplitudes e_x and e_y together with their correlated and uncorrelated uncertainties were finally extracted:

$$\begin{aligned} e_x &= (30 \pm 34 \pm 4)\,\mu\mathrm{rad} \\ e_y &= (21 \pm 45 \pm 3)\,\mu\mathrm{rad}\ . \end{aligned} \tag{3.27}$$

Note that the correlated uncertainties are one order of magnitude larger than the uncorrelated uncertainties. The results of the sidereal phase amplitudes can be expressed in terms of the SME coefficients [27, 37]

$$\tilde{b}_{X,Y}^{\mathrm{n}} = \frac{1}{2}\frac{\hbar\Omega_s}{\frac{\gamma_{He}}{\gamma_{Xe}} - 1} \cdot e_{x,y}\ , \tag{3.28}$$

assuming that the spins and the magnetic moments of the ^{3}He and ^{129}Xe nuclei are determined by the valence neutron according to the Schmidt model [58]. This simple

model results in estimations for the two components of the background field that are perpendicular to the Earth's axis:

$$\begin{aligned} \tilde{b}_X^{\mathrm{n}} &= (4.1 \pm 4.7) \cdot 10^{-34}\ \mathrm{GeV} \\ \tilde{b}_Y^{\mathrm{n}} &= (2.9 \pm 6.2) \cdot 10^{-34}\ \mathrm{GeV}\ . \end{aligned} \tag{3.29}$$

These results can be interpreted as a new upper limit of the equatorial component $\tilde{b}_\perp^{\mathrm{n}}$ of the background tensor field interacting with the spin of the bound neutron:

$$\begin{aligned} \tilde{b}_\perp^{\mathrm{n}} &< 6.7 \cdot 10^{-34}\ \mathrm{GeV}\ (68\%\ \mathrm{CL}) \\ \tilde{b}_\perp^{\mathrm{n}} &< 1.3 \cdot 10^{-33}\ \mathrm{GeV}\ (95\%\ \mathrm{CL})\ . \end{aligned} \tag{3.30}$$

The method for the determination of the equatorial component is explained in Appendix A.3 on p. 133.

There are nuclear models available that are more accurate than the simple Schmidt model: Theoretical calculations and experimental data indicate that the contribution of the neutron to the ^{3}He spin is 87% [59] (experimental data). Correspondingly, the contribution of the neutron to the ^{129}Xe spin is 75% [60] (theoretical calculations).
This results in more accurate values

$$\begin{aligned} \tilde{b}_X^{\mathrm{n}} &= (5.1 \pm 4.9) \cdot 10^{-34}\ \mathrm{GeV} \\ \tilde{b}_Y^{\mathrm{n}} &= (3.6 \pm 7.8) \cdot 10^{-34}\ \mathrm{GeV} \end{aligned} \tag{3.31}$$

with the corresponding upper bounds on the equatorial component

$$\begin{aligned} \tilde{b}_\perp^{\mathrm{n}} &< 8.4 \cdot 10^{-34}\ \mathrm{GeV} \quad (68\%\ \mathrm{Confidence\ Level}) \\ \tilde{b}_\perp^{\mathrm{n}} &< 1.6 \cdot 10^{-33}\ \mathrm{GeV} \quad (95\%\ \mathrm{Confidence\ Level})\ . \end{aligned} \tag{3.32}$$

3.5 Corresponding Limits on Proton Interactions

The assumption that the spins and the magnetic moments of the ^{3}He and ^{129}Xe nuclei are determined by the valence neutron (Schmidt model, [58]) is not correct. The Schmidt model overestimates the magnetic moment for most nuclei. In [5] Y. Stadnik and V. Flambaum calculated the neutron and proton contributions to the nuclear spin for several nuclei of experimental interest. They showed that the ^{3}He and ^{129}Xe system is also very sensitive to the coupling of the proton spin to a hypothetical background field.
The different contributions to the nuclear magnetic moment μ can be expressed as

$$\frac{\mu}{\mu_N} = g_p < s_p^z > + g_n < s_n^z > + g_l < l_p^z > \tag{3.33}$$

with the nuclear magneton μ_N, the expectation values of the total neutron and proton spins $< s_n^z >$ and $< s_p^z >$, and the expectation value of the total proton orbital momentum $< l_p^z >$. The gyromagnetic factors are $g_p = 5.586$, $g_n = -3.826$ and $g_l = 1$.
Taking the experimental values of the magnetic moments of the nuclei (and neglecting spin-orbit interaction), Stadnik and Flambaum calculated the proton and neutron spin contributions. In particular with $< l_p^z >= 0$ for ^{3}He and ^{129}Xe:

$$\begin{aligned} < s_p^z >_{He} &= 0.000 \\ < s_n^z >_{He} &= 0.500 \end{aligned} \tag{3.34}$$

and

$$\begin{aligned} < s_p^z >_{Xe} &= 0.135 \\ < s_n^z >_{Xe} &= 0.365 \ . \end{aligned} \tag{3.35}$$

In words, for ^{3}He the Schmidt model is valid and the magnetic moment of ^{3}He is determined by the valence neutron. However, for ^{129}Xe the proton contribution is large. Therefore, the ^{3}He and ^{129}Xe system is also sensitive to the proton interaction parameters of the SME [5]:

$$\begin{aligned} \tilde{b}_X^{\mathrm{n}} + 0.74 \cdot \tilde{b}_X^{\mathrm{p}} &= (7.1 \pm 8.2) \cdot 10^{-34} \text{ GeV} \\ \tilde{b}_X^{\mathrm{n}} + 0.74 \cdot \tilde{b}_Y^{\mathrm{p}} &= (5.0 \pm 10.8) \cdot 10^{-34} \text{ GeV} \end{aligned} \tag{3.36}$$

with the corresponding upper limit of the equatorial component $\tilde{b}_\perp^{\mathrm{p}}$ of the background tensor field interacting with the spin of the bound proton:

$$\tilde{b}_\perp^{\mathrm{p}} < 1.6 \cdot 10^{-33} \text{ GeV} \quad (68\% \text{ Confidence Level}) \ . \tag{3.37}$$

This value improves the previously best limit by a factor 35.

3.6 Phase Stability, Sensitivity Estimation and Systematic Uncertainties

The obtained values in Eq. (3.31) including uncertainties are a direct result of the fitting procedure. Of course, it is necessary to check for possible systematic errors and to check the validity of the uncertainty estimates. In this case, the Lorentz invariance violating interaction would cause a sinusoidal phase shift with the period of a sidereal day and it has to be excluded that other effects with a similar time structure occur. Otherwise it would be possible that these effects mask the fundamental interaction under investigation leading to a false negative result - or produce a false positive result by a fake signal.
In this section the phase stability is investigated, finally leading to a statistical sensitivity estimation and upper bounds on systematic uncertainties.
A first (rough) step to check for the phase stability is to have a look at the phase residuals: The reduction of the structures in the weighted phase difference data by three orders of magnitude (see Fig. 3.17 and 3.18) indicates that the time structures of all deterministic phase shifts (linear shifts, cross-talk and self-shift) are well described by the fit model. An incorrect fit model would cause a structure in the residuals, meaning that the residuals are not Gaussian distributed. For example, Fig. 3.19 shows the residuals of the weighted phase difference data of a single run if one omits the cross-talk terms in the fit model.
In the following paragraphs a quantitative and very sensitive method to investigate the phase stability (and systematic effects) is discussed.

The Cramer-Rao Lower Bound

The goal of the ^{3}He-^{129}Xe comagnetometer is to find additional interactions that are of non-magnetic type by looking for tiny frequency or phase shifts. Thus, it is essential to

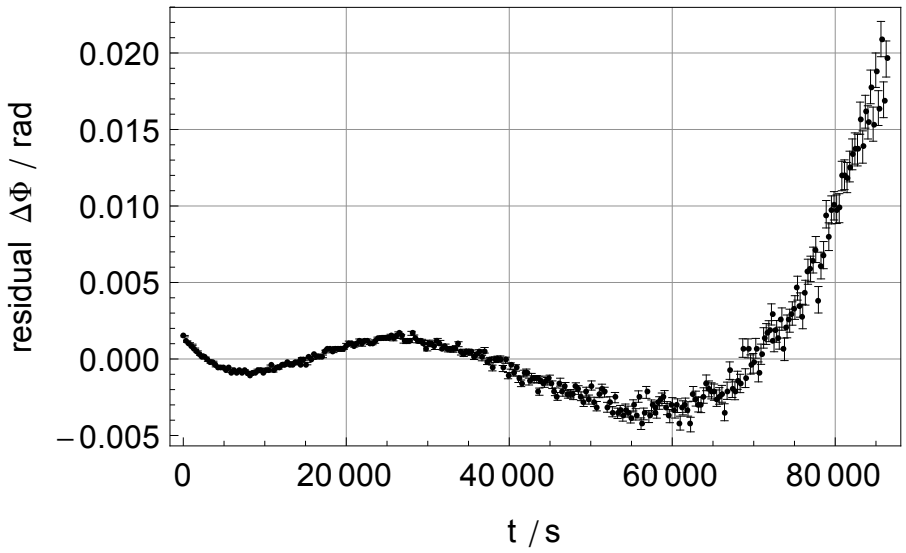

Figure 3.19: The residuals of the weighted phase difference data of a single run (j=6) with a fit model without the cross-talk terms. The residuals are clearly not Gaussian distributed around zero (unlike the residuals using the complete fit model, compare Fig. 3.17).

perform the data analysis in such a way that the phase or frequency estimator is the optimal estimator: unbiased and with the minimum variance.
The statistical methods in signal processing derived by Harald Cramer and Calyampudi Radhakrishna Rao have proven to be extremely useful in practice: The Cramer-Rao Lower Bound (CRLB) gives the minimum variance of an unbiased estimator of a deterministic parameter. Thus, the final experimental result (after all the data analysis has been performed) can be compared to the CRLB, providing a benchmark.
In this case, the sensitivity of phase or frequency measurements depends on the measurement time with coherent spin precession T, the signal amplitude at the beginning of the measurement A decaying with a time constant T_2^* and the noise level ρ (assuming white noise) [38, 40, 51]. The uncertainty in the frequency of the signal with a constant frequency is:

$$\sigma_f \quad \geq \quad \frac{\sqrt{3}}{\pi}\frac{\rho}{A} \cdot T^{-3/2} \cdot \sqrt{C(T, T_2^*)} \tag{3.38}$$

with the dimensionless factor $C(T, T_2^*)$ accounting for the exponential decay of the signal-to-noise ratio ($C(T, T_2^*) \approx 1.7$ for $T = T_2^*$, details in [38]). The remarkable result is that the uncertainty in frequency decreases with $T^{-3/2}$ for an optimal estimator.
Correspondingly, the uncertainty in phase determination of the signal with a constant frequency is:

$$\sigma_\Phi \quad \geq \quad \frac{\sqrt{3}}{\pi}\frac{\rho}{A} \cdot T^{-1/2} \cdot \sqrt{C'(T, T_2^*)}\ . \tag{3.39}$$

Here the uncertainty in phase decreases with $T^{-1/2}$.
The measurement results can be compared to these lower bounds. In particular, it can be tested if the results follow the power-laws $T^{-1/2}$ and $T^{-3/2}$.

The Allan Standard Deviation

The Allan Standard Deviation (ASD) [38, 55–57] (named after David W. Allan) is the most convenient measure to study the temporal characteristics of the ^{3}He-^{129}Xe comagnetometer with respect to phase or frequency determination. The ASD method is an established analysis technique for studying the low-frequency component of a time series and is a measure of phase and frequency stability in clocks, oscillators and amplifiers. For example, one can compare the stability of two oscillators by measuring the phase difference $\Delta\Phi_i$ of the two signals at equidistant times $t_i = i{\cdot}\Delta t$ $(i = 0, ..., N-1)$ with the total measurement time $N \cdot \Delta t$.
These samples $\Delta\Phi_i$ are then divided into S consecutive groups, so that each group has n consecutive samples $\Delta\Phi_i$. Then the corresponding averages over the time $\tau = n \cdot \Delta t$ are calculated:

$$\overline{\Delta\Phi}_j(\tau = n \cdot \Delta t) \;=\; \frac{1}{n} \sum_{i=n\cdot j}^{(n+1)j} \Delta\Phi_i \;. \tag{3.40}$$

The Allan Variance is now defined as

$$\sigma_\Phi^2(\tau) \;=\; \frac{1}{2S-2} \sum_{j=0}^{S} \left[\overline{\Delta\Phi}_{j+1}(\tau) - \overline{\Delta\Phi}_j(\tau)\right]^2 \tag{3.41}$$

and the Allan Standard Deviation $\sigma_\Phi(\tau)$ is the square-root of the Allan Variance.
Typically, τ is varied (by varying n) and the results are plotted as a function of the integration time τ to study the temporal characteristics of the oscillators and to identify the power-law model of the phase noise under study. Especially low-frequency noise and drifts can be evaluated.
In the case of the ^{3}He-^{129}Xe comagnetometer, the phase difference $\Delta\Phi_i$ is just the weighted phase difference after subtraction of all deterministic phase shifts, i.e. one compares the ^{3}He precession signal (the first oscillator) to the "scaled" ^{129}Xe precession signal (the second oscillator). These two oscillator frequencies are supposed to be the same if all deterministic phase shifts (chemical shift, Earth's rotation, Ramsey-Bloch-Siegert shift etc.) have been incorporated correctly. Taking the single run phase residuals from Fig. 3.17 (bottom), the behavior of the phase uncertainty in the ASD plot is shown in Fig. 3.20 (top) and the corresponding frequency uncertainty in the ASD plot in Fig. 3.20 (bottom). With increasing integration times τ the uncertainty in phase decreases with $\sigma_{\mathrm{ASD}} \propto \tau^{-\frac{1}{2}}$ down to the ≈ 10 μrad level and the uncertainty in frequency with $\sigma_{\mathrm{f,\,ASD}} \propto \tau^{-\frac{3}{2}}$ down to the ≈ 10 pHz level as expected by the CRLB in Eqs. (3.39) and (3.38). This indicates the presence of pure white (Gaussian) noise. In other words: All deterministic phase shifts (chemical shift, Earth's rotation, Ramsey-Bloch-Siegert shift etc.) have been incorporated correctly. This has been tested for all measurement runs with different experimental conditions (e.g. different sample cells, partial pressures, magnetic field directions, T_2^*) and the ASD plot shows the expected

behavior leading to the conclusion that the fit model in Eq. (3.19) describes the behavior of the comagnetometer correctly. An incorrect fit model would immediately lead to a deviation from the CRLB power law. This is demonstrated in Fig. 3.21 showing the ASD (phase and frequency) as a function of τ for the residuals of a fit model where the cross-talk term is omitted. Here the data of run $j = 6$ were used, the run with largest cross-talk term (compare Tab. 3.1). The large deviation from the CRLB power law above a few hundred seconds is impressive. For run $j = 3$ (the run with the smallest cross-talk term) the deviation in the ASD plot is smaller (Fig. 3.22).

Systematic Uncertainties

In this case, the Lorentz invariance violating interaction would cause a sinusoidal phase shift with the period of a sidereal day. It has to be excluded that other effects with a similar time structure occur. Otherwise it would be possible that these effects mask the fundamental interaction under investigation leading to a false negative result - or produce a false positive result by a fake signal. A possible source could be a temperature drift leading to small changes in the position of the SQUIDs with respect to the sampele cell. As the measured phase depends very sensitively on the SQUID position (see p. 76) this might cause such a periodical phase shift.
Different sources of deterministic phase shifts have been discussed above and were integrated into the fit model. Correlations between the fit parameters describing the Lorentz invariance violating effect and deterministic phase shifts due to a partly similar time structure have been accounted for during the fitting procedure and contribute to the correlated uncertainty. The absence of further systematic effects or deterministic phase shifts can be shown by looking at the runs individually. Especially runs with different magnetic field directions are of interest: The phase of the modulation due to the Lorentz invariance violating effect depends on the direction of the magnetic guiding field (see section 3.22 on p. 83 and Appendix A.1 on p. 127). However, it is very unlikely that the phase of temperature dependent shifts would change by the same amount. Therefore by looking at the ASD plots of runs with different magnetic guiding field directions one can exclude that other effects with a similar time structure occur. The absence of any deviation from the CRLB power law down to ≈ 10 μrad (see Fig. 3.20) indicates that the time structures of all phase shifts in the system are well described by the fit model. Possible systematic uncertainties are in the < 10 μrad range, i.e., the sensitivity range set by the uncorrelated uncertainty. The uncertainties in the parameters describing the Lorentz invariance violating effect are dominated by correlated statistical uncertainties (≈ 40 μrad in Eq. (3.27)) and are the result of the combined fit to all seven measurement runs. Thus, the systematic uncertainties are significantly smaller than the correlated uncertainty which sets the present upper limit on LV effects. The systematic checks have been performed with great care and include the use of different cells, the variation of the applied magnetic field direction as well as partial pressure (2-8 mbar ^{3}He), polarizations (factor 3) and T_2^* (from 26 h to 85 h for ^{3}He). The ASD follows the CRLB power law for all of the experimental configurations. Thus systematic effects have found to be of no concern at the current sensitivity limit of the ^{3}He-^{129}Xe comagnetometer which is clearly set by statistical uncertainties.

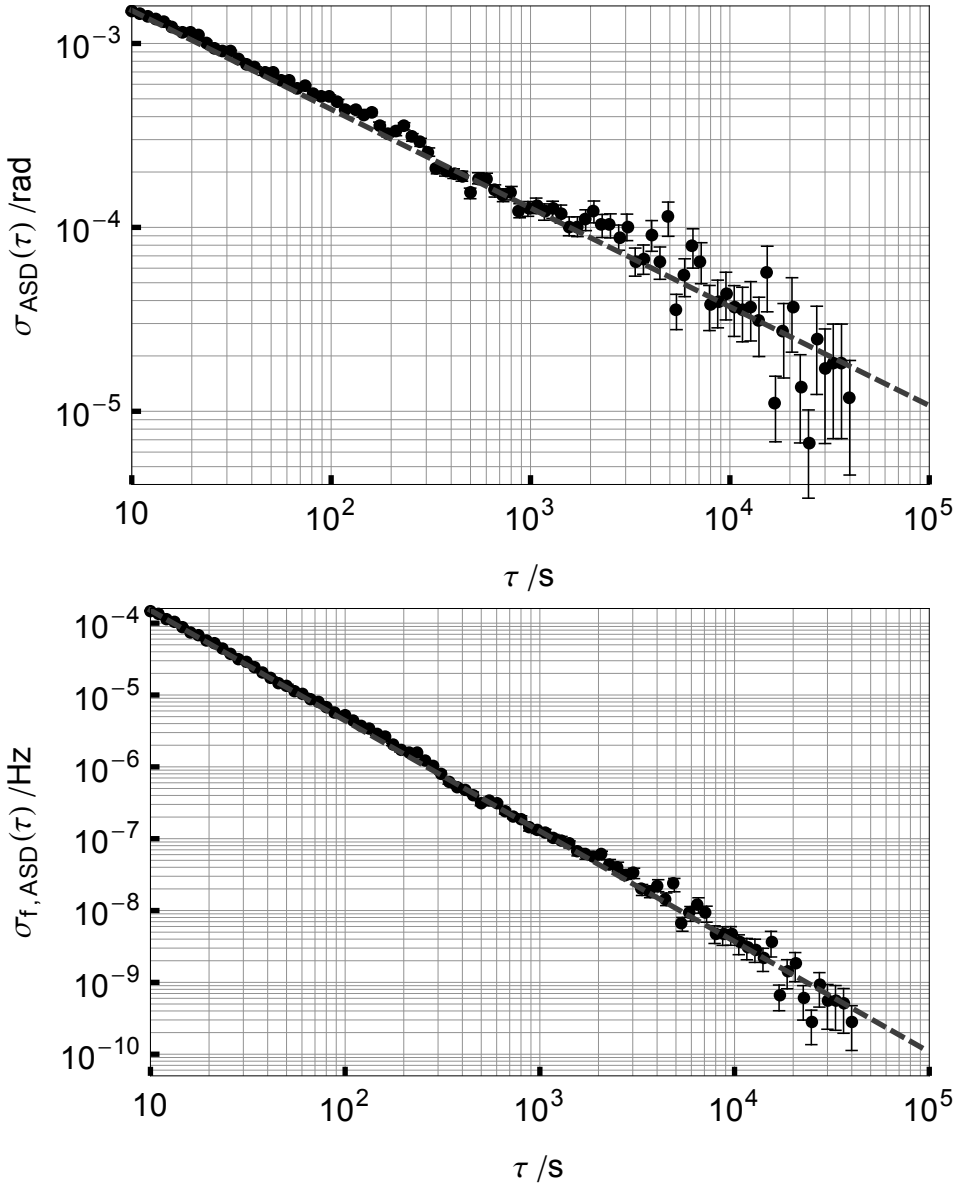

Figure 3.20: Allan Standard Deviations (ASD) of the residual phase noise (top) and the corresponding frequency noise (bottom) of a single run ($j = 6$). The total observation time was $T = 90000$ s. With increasing integration times τ the uncertainty in phase decreases with $\sigma_{\mathrm{ASD}} \propto \tau^{-\frac{1}{2}}$ and the uncertainty in frequency with $\sigma_{\mathrm{f,\ ASD}} \propto \tau^{-\frac{3}{2}}$ indicating the presence of white (Gaussian) noise.

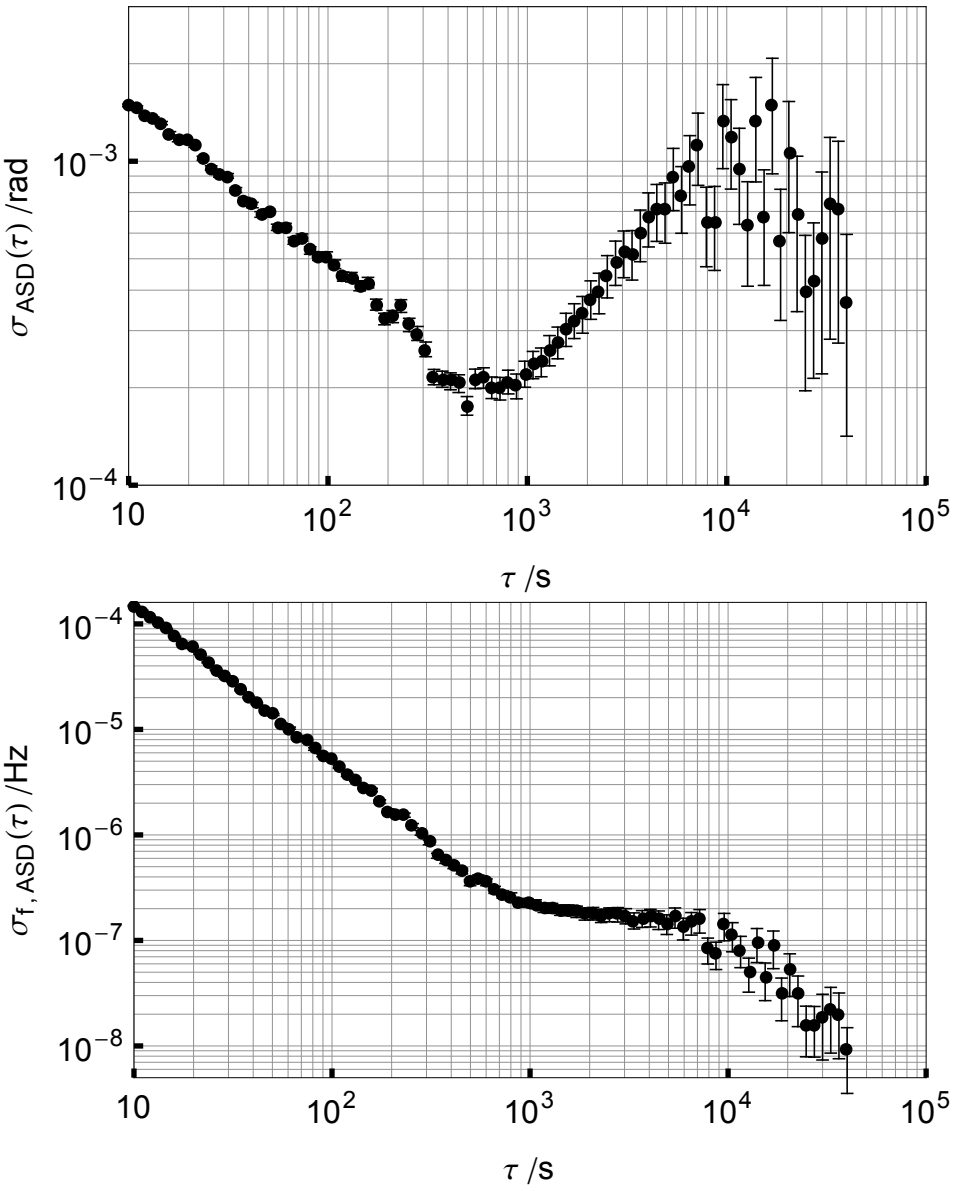

Figure 3.21: Allan Standard Deviations (ASD) of the residual phase noise of a single run ($j = 6$) if one does not integrate the Cross-Talk term into the fit model (see Fig. 3.19). For short integration times $\tau < 300$ s the uncertainties decrease according to the CRLB power law, but then strong deviations occur due to the Cross-Talk phase shift that has not been accounted for.

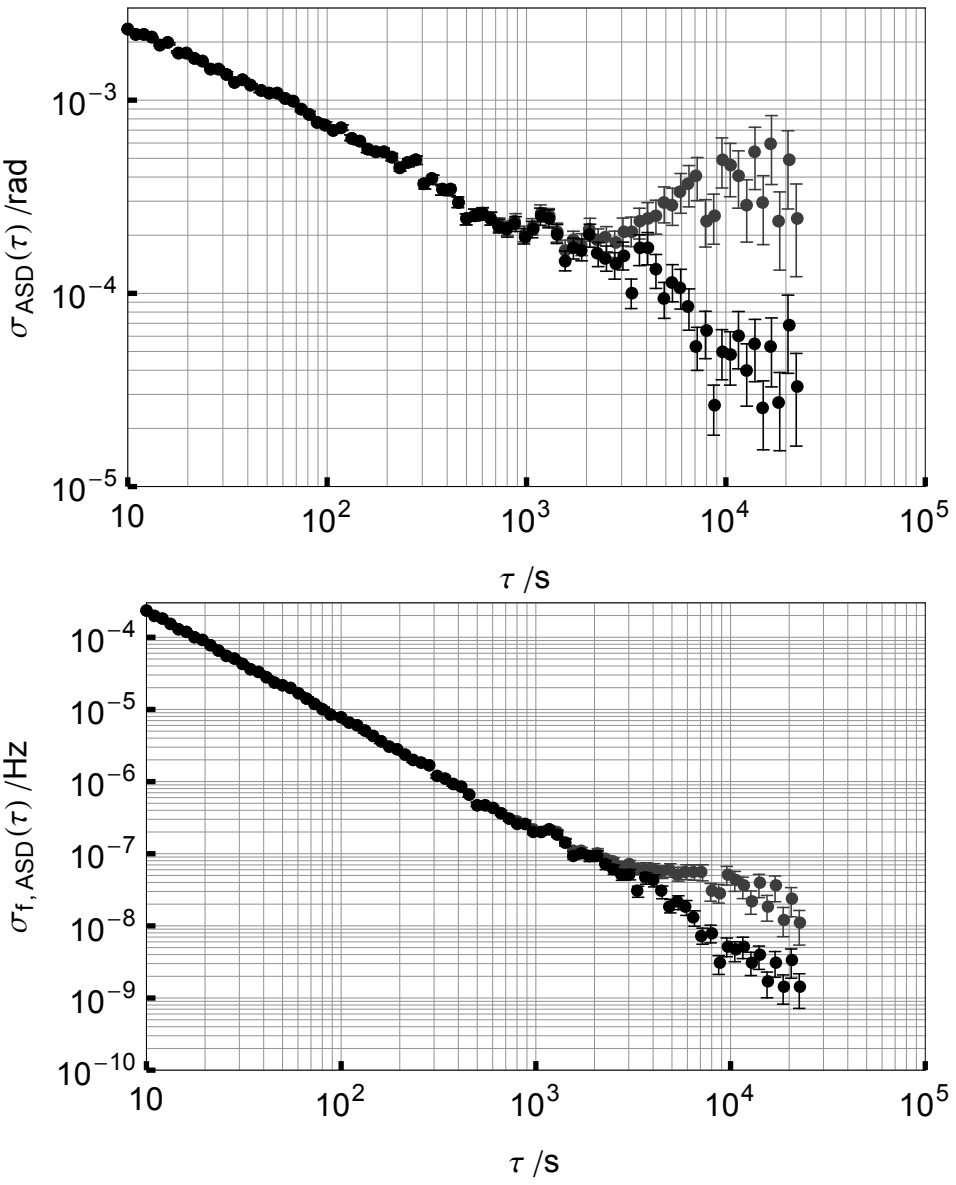

Figure 3.22: Comparison of the Allan Standard Deviations (ASD) of the residual phase noise (top) and frequency noise (bottom) of a single run ($j = 3$) for the correct fit model (black) and if one does not integrate the Cross-Talk term into the fit model (gray). In run $j = 3$ the influence of the Cross-Talk is smaller compared to Fig. 3.21.

3.7 Conclusion and Outlook

In the preceding sections, the experiments and methods of data evaluation have been described that put a limit on a Lorentz invariance and CPT violating coupling of the (bound) neutron spin $\boldsymbol{\sigma^n}$ to a hypothetical background field $\tilde{\boldsymbol{b}}^{\boldsymbol{n}}$. Such a coupling of the form

$$V = -\tilde{\boldsymbol{b}}^{\boldsymbol{n}} \cdot \boldsymbol{\sigma^n} \quad . \tag{3.42}$$

is motivated within the minimal Standard Model Extension. The experimental result was found to be compatible with zero

$$\begin{aligned} \tilde{b}_X^{\mathrm{n}} &= (5.1 \pm 4.9) \cdot 10^{-34} \text{ GeV} \\ \tilde{b}_Y^{\mathrm{n}} &= (3.6 \pm 7.8) \cdot 10^{-34} \text{ GeV} \ . \end{aligned} \tag{3.43}$$

The corresponding upper limits on the equatorial component are

$$\begin{aligned} \tilde{b}_\perp^{\mathrm{n}} &< 8.4 \cdot 10^{-34} \text{ GeV} \quad (68\% \text{ Confidence Level}) \\ \tilde{b}_\perp^{\mathrm{n}} &< 1.6 \cdot 10^{-33} \text{ GeV} \quad (95\% \text{ Confidence Level}) \ . \end{aligned} \tag{3.44}$$

This is an improvement by a factor of 50 compared to the year 2009 measurements with the ^{3}He-^{129}Xe comagnetometer [37] and an improvement by a factor of 4 compared to the former best limit measured by a ^{21}Ne-Rb-K comagnetometer [13].
Furthermore, the data can be used to extract the corresponding limits on proton interactions: $\tilde{b}_\perp^{\mathrm{p}} < 1.6 \cdot 10^{-33}$ GeV.
The gain in measurement sensitivity compared to the year 2009 measurements mainly arises from two improvements: Firstly, the SNR could be increased by a factor of 4 thanks to the higher xenon polarization of $P_{Xe} \approx 40\%$ and the use of four independent gradiometers. Furthermore, with the larger size of the spherical glass cells, the longitudinal wall relaxation time which scales like $T_{1,wall} \propto R$ could be improved by a factor of 2 for both gas species, i.e., $T_{1,wall}^{He} \approx 165$ h and $T_{1,wall}^{Xe} \approx 15$ h. Furthermore the gradients of the magnetic guiding field could be reduced. In particular for xenon, that resulted in a significant increase of the transverse relaxation time of $T_{2,Xe}^* \approx 8.5$ h compared to $T_{2,Xe}^* \approx 4.5$ h in 2009 [37]. Thus, coherent spin-precession could be monitored for more than 24 hours ($\approx 3 \cdot T_{2,Xe}^*$), whereas typical measurement times in 2009 were limited to 14 hours. The longer periods of coherent spin precession had another advantage, inasmuch as the correlated uncertainty which sets the present sensitivity limit of our ^{3}He-^{129}Xe comagnetometer could be drastically reduced. The large correlated uncertainty (σ_{corr}) on the sidereal phase modulation is caused by a partly similar time structure of $\Delta\Phi_{\mathrm{c}}(t)$ and the function describing the sidereal phase modulation.
Several future improvements are feasible. Presently, the relatively short $T_{2,Xe}^*$, essentially set by $T_{1,wall}$, limits the total observation time T of free spin-precession. Efforts to increase $T_{1,wall}$ considerably (e.g. by increasing the radius of the measurement cell) are therefore essential. Besides gain in phase sensitivity according to the $T^{-\frac{1}{2}}$ power law (CRLB), the still dominating correlated uncertainty will approach the uncorrelated one. Furthermore, successive measurement runs can be extended to a period of about 100 days. The long time span gives the possibility to measure an annual variation of a

daily sidereal modulation to extract limits on boost-dependent Lorentz invariance and CPT violating effects like in Ref. [21].
Furthermore, measurements using a slowly rotating magnetic guiding field have been described. Though the results of these measurements did not flow into the final limits on Lorentz invariance violation a lot of knowledge about the behavior of the comagnetometer, the mu-metal shielding and the measurement system etc. could be derived. Finally, this led to an optimization procedure with respect to gradient relaxation that will be also applied in future measurements. Spin coherence could be maintained for a very long time with $T^*_{2,Xe} \approx 8.5$ h and $T^*_{2,He} \approx 100$ h.

4 Preparations for the Measurements of the Electric Dipole Moment of ^{129}Xe

This experiment is an attempt to measure the atomic Electric Dipole Moment (EDM) of ^{129}Xe using a ^{3}He-^{129}Xe comagnetometer. The following chapter addresses the preparations and experimental efforts to measure the EDM of ^{129}Xe. Developments that have been made at Heidelberg as a part of this dissertation are described in detail, whereas contributions from other parts of the collaboration are shortly summarized.
To repeat the concept of measurement: A permanent EDM $\boldsymbol{d}$ of a fundamental or composite particle must be aligned parallel to the spin, as the spin is the only available vector for an eigenstate of the isolated particle. Thus, for a magnetic guiding field aligned along the z-direction, the Hamiltonian has the form $H = -\mu \cdot B_0 - d \cdot E_z$, with the corresponding frequency shift $\delta\omega_{\mathrm{EDM}} = \frac{2}{\hbar} d \cdot E_z$. By varying the z-component of the electric field E_z, the frequency shift is modulated correspondingly. As mentioned before, the principle of comagnetometry is applied to become insensitive to drifts of the magnetic guiding field. Subsequently, a non-zero EDM will manifest in a modulation of the weighted phase difference, and the corresponding value d can be extracted. In the case of a result that is compatible with zero, upper limits can be deduced. EDMs of particles are closely connected to CP-violation as described in the introduction, and therefore corresponding limits on CP-violation can be inferred. The goal of this experiment is to significantly improve the current limit on the ^{129}Xe-EDM. The best measurements up to now have been performed at the University of Michigan in the year 2000 by M. A. Rosenberry and T. E. Chupp [73, 74]: $d = (0.7 \pm 3.3_{\mathrm{stat}} \pm 0.1_{\mathrm{syst}}) \cdot 10^{-27}$ ecm. This value is a result of 125 runs, each lasting between eight hours and several days.
In the following sections, the technical developments and modifications of the experimental set-up will be presented first. Afterwards the sensitivity of the comagnetometer will be estimated based on the Lorentz invariance violation data (see Chapter 3). Then possible systematic effects and measurement strategies to detect or avoid them will be discussed. Finally, an outlook on future developments will be given.

4.1 Experimental Technique

Major changes of the experimental set-up have been performed and are still going on. Parts of the experiment that changed (compared to the Lorentz invariance violation measurements) will be presented at this point.

4.1.1 The Magnetically Shielded Room and the Generation of the Magnetic Guiding Field

To improve the current limit on the EDM of ^{129}Xe by many orders of magnitude (after first measurements as a proof-of-principle), subsequent runs with a total measurement

time in the order of 100 days will be required. Additionally, systematic tests have to be performed carefully (see below). This requires to have access to a magnetically shielded room for several months without interruption.
Such a room with two layers of mu-metal and a single layer aluminum is available at Forschungszentrum Jülich. The shielded room is used for high-temperature SQUID system development with the corresponding applications in biomagnetism and medicine (e.g. adult and fetal magnetocardiography and low-field NMR). An additional mu-metal cylinder is placed in the center of the room to reach the necessary conditions with respect to magnetic noise and field gradients. Subsequently, the measurement cell containing the polarized ^{3}He and ^{129}Xe gas and the SQUID measurement system have to be placed inside the cylinder, as well as the coils that produce the magnetic guiding field. Therefore, the large square Helmholtz coils, that have been used for the Lorentz invariance measurements, have to be replaced. A current density $\boldsymbol{j}(\varphi) \propto \cos(\varphi) \cdot \hat{\boldsymbol{z}}$ on the surface of a cylinder with infinite length (where φ is the azimuth angle and $\hat{\boldsymbol{z}}$ is a unit vector pointing along the cylinder axis) produces a homogeneous magnetic field inside the cylinder perpendicular to the cylinder axis. A coil with such a current density (approximated by currents through wires) is called a cosine-coil. The resulting homogeneity of the magnetic field depends on the number of wires and the precision of the manufacturing. In addition to the cosine-coil, conventional Helmholtz coils are installed to produce a magnetic field parallel to the cylinder axis in order to manipulate the sample spins (e.g. non-adiabatic switching). As these coils are only needed for a short period at the start of the experiment, the requirements concerning field homogeneity are not as high.
In order to reach long transverse relaxation times, it is necessary to minimize the magnetic field gradients (see Eq. (2.36)). This can be done by additional shimming coils that produce inhomogeneous fields (Anti-Helmholtz coils along the cylinder axis, and saddle coils perpendicular to the cylinder axis) to compensate the gradients.
The design of the coils, the corresponding calculations (e.g. influence of the mu-metal cylinder on the homogeneity) as well as the construction of the coils and the supporting structures was done by S. Zimmer (Institut für Physik, Uni Mainz) and O. Grasdijk (KVI, Uni Groningen).

4.1.2 The Design of the Sample Cell

For the EDM measurements, an electric field has to be applied in a controlled way. For example, it would not be possible to use the spherical sample cells and apply an electric field by using external capacitor plates, because the glass wall of the cell would charge up and reduce the field inside the sample cell in an uncontrollable way. Therefore, cylindrical cells have been developed with the end planes made of silicon wafers and the lateral surface made of the usual low-relaxation GE-180 glass. The distance between the electrodes is 6 cm and the maximum voltage that can be applied is 12 kV (see below). Thus, the maximum resulting electric field parallel (or anti-parallel) to the magnetic field is $E_z = 2$ kV/cm. The cell is surrounded by a housing made of conductive plastic at ground potential to protect the SQUID-system against flash-overs (see Fig. 4.1). This housing is filled with SF_6 to suppress flash-overs and to minimize leakage currents.

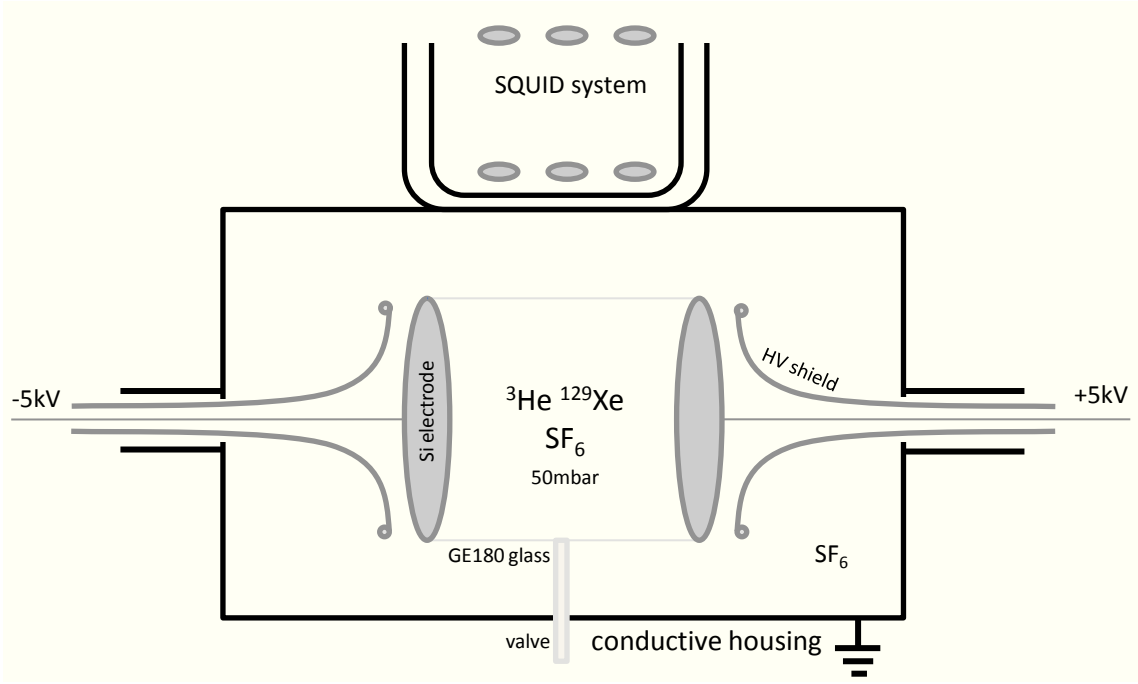

Figure 4.1: Principle drawing of the cylindrical sample cell with two silicon electrodes inside a conductive housing at ground potential. The housing is filled with SF_6 and the sample cell is filled with a mixture of ^{3}He, ^{129}Xe and SF_6. The housing is placed directly below the cryostat. For further information on the high voltage feed-through and shielding electrodes see p. 103.

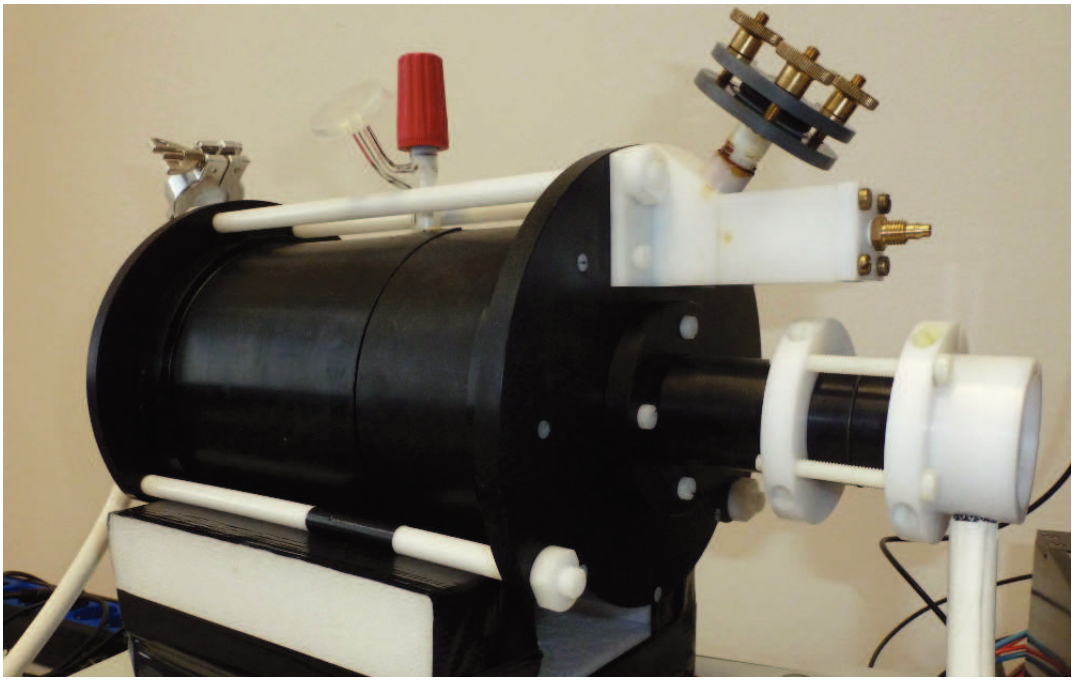

Figure 4.2: The housing of the EDM cell made of conductive plastic (PE with graphite additives) constructed by A. Scharth and S. Zimmer (Institut für Physik, Uni Mainz).

4.1.3 The Leakage Current Detection and High Voltage Supply

Currents associated with the high voltage give rise to a systematic error (see p. 115). Therefore, the currents that flow in the proximity of the sample cell, especially between the two electrodes, have to be monitored. These currents are in the pA range. At voltages of a few kV, usually the currents flowing through the insulation of the cables are much higher and cannot be easily separated from the currents that flow across the EDM cell. Thus, the following principle was applied to measure the EDM cell leakage currents (see Fig. 4.1 and 4.3):
The conductor, that contacts the Si-electrode of the EDM cell (and keeps it at the high potential, e.g., +5 kV with respect to ground), is always surrounded by an insulating layer, and then by a conductive shielding that is at the same potential as the innermost wire. Then an additional insulating layer and a conductive shielding at ground potential follow. Therefore, the voltage between the innermost wire and the first shielding is always zero, and consequently the leakage current through the first insulating layer is also zero. The high voltage between the first and second shielding (in this case 5 kV) leads to leakage currents through the second insulating layer. However, these currents do not flow through the innermost wire. Consequently, by measuring the current through the innermost wire, one measures the current that flows directly from the one electrode of the EDM cell to the other. A possible path would be the inner or outer surface of the glass wall, or a current directly through the cell volume by ionized gas particles. Currents directly flowing from the electrode to the conductive housing are suppressed by additional shielding electrodes.
This principle of double shielding was maintained throughout all connections from the electrodes to the Picoamperemeter (pA-meter) (see Fig. 4.3): The connection inside the housing is made of several concentric plastic tubes, either conductive (by graphite additives, $R \approx 20$ MΩ) or insulating polyethylene. These materials - as all materials in the proximity of the EDM cell - are non-magnetic. For the connection to the pA-meters, which are placed outside the mu-metal cylinder, a special cable was manufactured. It consists of a coaxial cable inside a silicone hose (wall thickness: 3 mm). The silicone hose is surrounded by a copper wire mesh, fixed by shrink-on tube. The high voltage is between the inner and outer shielding, e.g., across the wall of the silicone hose. The dielectric strength of silicone rubber is ≈ 30 kV/mm, so there is plenty of safety margin. (Tests have been performed with a voltage up to 30 kV.)

The Picoamperemeter

As the current through the innermost wire has to be measured, the pA-meter has to be placed at the high potential. To do so, the pA-meter circuit boards (see below) and a battery are placed in an aluminum box. This conductive box is surrounded by an insulating plastic housing, so that the whole inner box can be kept at a high potential with respect to the surroundings at ground potential (via the high voltage supply, see below). The pA-meter is read out via an optical interface (insulating optical fibers). The inner shielding of the double shielded cable is directly connected to the aluminum housing of the pA-meter, whereas the innermost wire connects the input of the pA-meter with

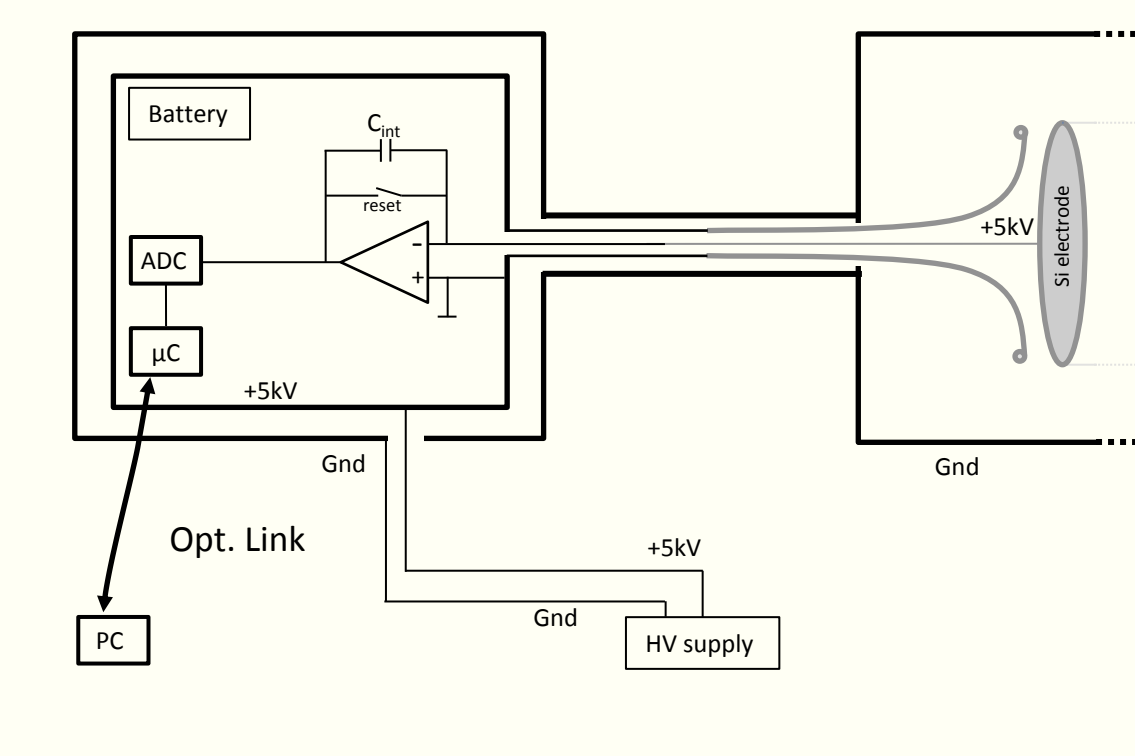

Figure 4.3: Principle drawing of the leakage current detection with double shielded cables and connections, and the pA-meter at the high potential. The connections and the pA-meter for the first electrode are shown. The setup for the other electrode is the same (with a separate pA-meter).

the electrode of the cell. The pA-meter itself was developed in close collaboration with the electronics workshop of the Physikalisches Institut, Uni Heidelberg (V. Angelov). It consists of an integrator IC (IVC102 from Burr-Brown/Texas Instruments) with a low bias-current precision operational amplifier and various integration capacitors on chip (10, 30 and 60 pF and their combinations selectable by external switches). The voltage of the (inverting) integrator output V depends on the capacity C_{int} and the actual charge Q of the capacitor: $V = -Q \cdot \frac{1}{C_{\text{int}}}$. The integrator output is digitalized by an 12 bit ADC (ADS7835 from Burr-Brown/Texas Instruments) with a typical sampling frequency $f_s = 10$ Hz , and send to a micro-controller (Atmel XMEGA32A4) that transmits the data to a measurement PC outside the shielded room. The actual current can be extracted by taking the derivative of the voltage output: $I = \frac{dQ}{dt} = -C_{\text{int}} \cdot \frac{dV}{dt}$. The calibration factor C_{int} can be roughly estimated from the data sheet (max. deviation from the nominal value: 20%, with $2.5 \cdot 10^{-5}/K$ temperature drift), but can be measured independently (see below).
Additionally, the current can be determined by a second method: The voltage of the integrator output is processed by four comparators. The comparator thresholds can be adjusted individually by DACs, and the comparator outputs are connected to input

pins of the micro-controller. Two of the comparators are intended for positive output voltages. For example, the thresholds are set to $V_{\text{low}} = 0.5$ V and $V_{\text{high}} = 4.5$ V, respectively. Let's assume that the capacitor is fully discharged at the beginning. Then, for a negative input current the integrator output voltage will rise and reach the V_{low} level. The corresponding comparator output triggers a timer inside the micro-controller. Eventually, the V_{high} level is reached and the comparator gives the stop signal for the timer. The measured time span Δt between start and stop signal is transfered to the measurement PC. The mean current can be calculated according to $I = -C_{\text{int}} \cdot \frac{V_{\text{high}} - V_{low}}{\Delta t}$.
For positive input currents the integrator output voltage decreases with time. Thus, the two remaining comparators are set to negative voltages. E.g., the timer is triggered as soon as the voltage drops below -0.5 V and stopped when the voltage reaches -4.5 V.
The voltage output is limited by the supply voltages (+6 V and -6 V) and the integrator has to be reset from time to time if the input current is non-zero. The integrator reset is triggered by either the high positive or negative comparator (4.5 V or -4.5 V), the same signal that stops the timer. This signal causes an interrupt of the micro-controller, which immediately closes the switch that discharges the capacitor C_{int} (see Fig. 4.3). After roughly 5 μs the capacitor is completely discharged and the switch opens again. The opening of the switch causes slight disturbing signals. Therefore, the low comparator levels that start the timer are set to 0.5 V and -0.5 V, respectively, instead of 0 V.
The two measurement methods are intended for different input current ranges: For currents below 100 pA the time between two integrator resets becomes longer than 1 s (assuming $C_{\text{int}} = 100$ pF) and the current is best monitored by taking the derivative of the voltage measured by the ADC. For higher currents the time between integrator resets becomes shorter and eventually the ADC sampling frequency $f_s = 10$ Hz is to low to resolve the voltage changes. Then the second method of measurement should be applied.

Calibration and Performance of the Picoamperemeter

The pA-meter can be calibrated by feeding a known current into the input. This current has to be in the order of the expected leakage current through the EDM cell, which is 1 to 10 pA. To generate such small currents in a well-defined way, the circuit in Fig. 4.5 was used. An arbitrary waveform generator was programmed, so that the output voltage U_{gen} has a trapezoidal form with a linear increase of the voltage from 0 to $U_0 = 10$ V in 100 seconds. Then the voltage stays constant for 100 s and linearly decreases to zero in 100 s. This waveform is repeated (see Fig. 4.7 top). The generator was coupled to the input of the pA-meter via an ceramic capacitor with $C_{\text{ext}} = 12.1 \pm 0.2$ pF. A class 1 capacitor was used that offers high stability and a high insulation resistance ($R_{\text{leak}} \approx 10^{15}\ \Omega$). The external current that is fed into the input is

$$I_{\text{ext}} = \frac{dU_{\text{gen}}}{dt} \cdot C_{\text{ext}} + U_{\text{gen}} \cdot R_{\text{leak}} \quad . \tag{4.1}$$

Additionally, there are offset currents I_{offset} on the printed circuit board and directly inside the IC that flow into the integrator input of the pA-meter. So the total input current is $I = I_{\text{ext}} + I_{\text{offset}}$. The offset current was measured with $U_{\text{gen}} = 0$ and the result can be seen in Fig. 4.6.
The described generator waveform has three phases (see Fig. 4.7): The rising generator

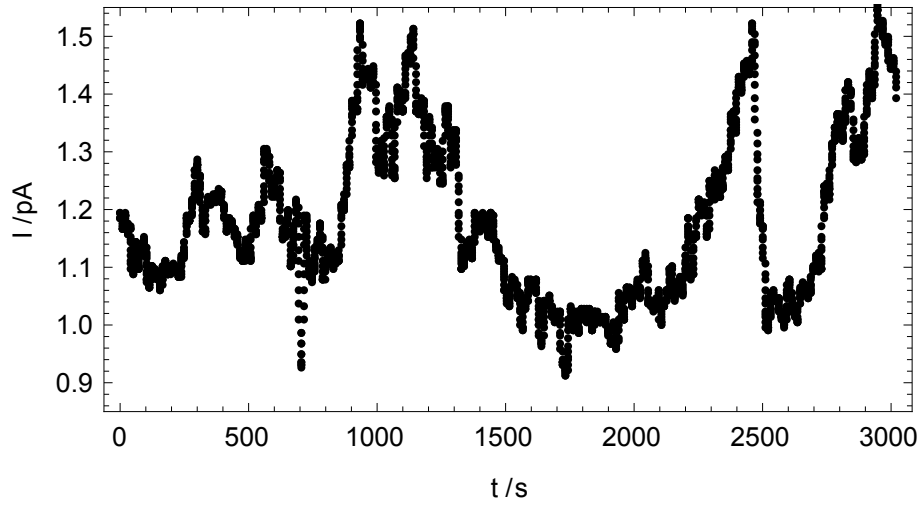

Figure 4.4: The measured leakage current of the EDM cell for a high voltage of 1 kV. The insulation resistance of the EDM cell is in the order of $R = 10^{15}$ Ω.

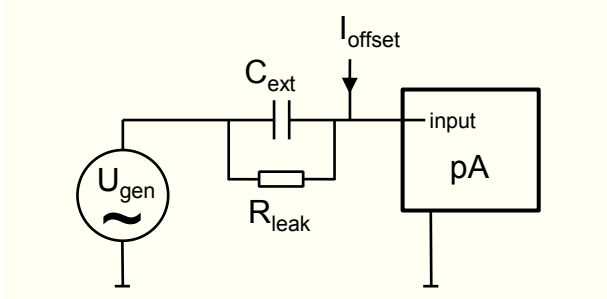

Figure 4.5: Schematic diagram of the pA-meter calibration circuit. A generator is coupled to the input of the pA-meter via an ceramic capacitor with a capacity of $C_{\text{ext}} = 12.1 \pm 0.2$ pF and an insulation resistance $R_{\text{leak}} \approx 10^{15}$ Ω. There are additional offset currents I_{offset} on the printed circuit board and directly inside the IC that flow into the integrator input of the pA-meter.

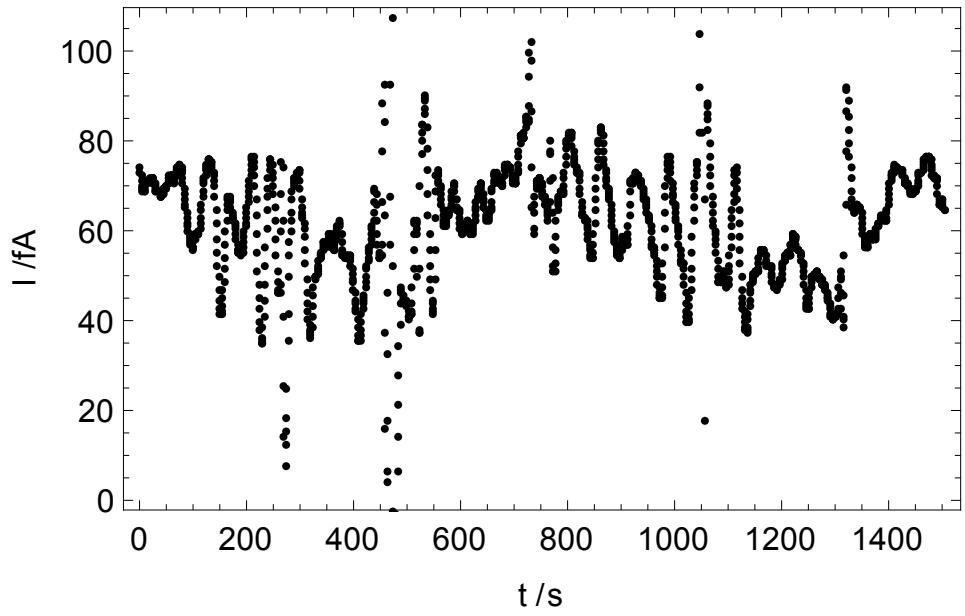

Figure 4.6: The pA-meter offset current $I_{\text{offset}} \approx 60$ fA (measured with $U_{\text{gen}} = 0$).

voltage causes a constant positive input current $I = 1.2$ pA. Then for $U_{\text{gen}} = \text{const.} = U_0$, the capacitor leakage resistance R_{leak} can be measured. In this case, $R_{\text{leak}} > 10^{14}\ \Omega$ was found. Therefore, leakage currents through the capacitor are negligible small. Then, the falling generator voltage causes a constant negative input current ($I = -1.2$ pA). These values have been used to calibrate the pA-meter. The largest uncertainty is caused by the offset currents on the printed circuit board and directly inside the IC that flow into the integrator input of the pA-meter, as these currents vary with time (see Fig. 4.6).

High Voltage Supply

The EDM cell is surrounded by a housing made of conductive plastic at ground potential. To keep the set-up symmetric, it proves beneficial to split the high voltage symmetrically: The first electrode is set to ± 5 kV, while the second electrode is set to ∓ 5 kV with respect to ground potential (instead of keeping the first electrode at ground potential and the second electrode at +10 kV or -10 kV). Therefore, a two-channel high precision high voltage supply (NHQ 246L 0n1) by Iseg [95] is used. One of the channels is set to negative output voltage and the other one to positive output voltage (the polarity can be changed manually by switches, but this is not used for this experiment). The output voltages (0 to +6 kV resp. 0 to -6 kV) of the NHQ are set remotely via RS232. Additionally, the output voltages and currents can be monitored remotely with a resolution of 100 mV and 100 pA. The ripple of the NHQ output voltage is less than 5 mV (peak to peak). The ripple is further reduced by RC low-pass filters (see Fig. 4.8). As the polarity of the voltage has to be invertible, four high voltage relays (Cynergy 3 DAT71215) are used to select the negative or positive voltage supply individually for each electrode. Large resistors at the output prevent large currents, for example, in the case of flash-overs.

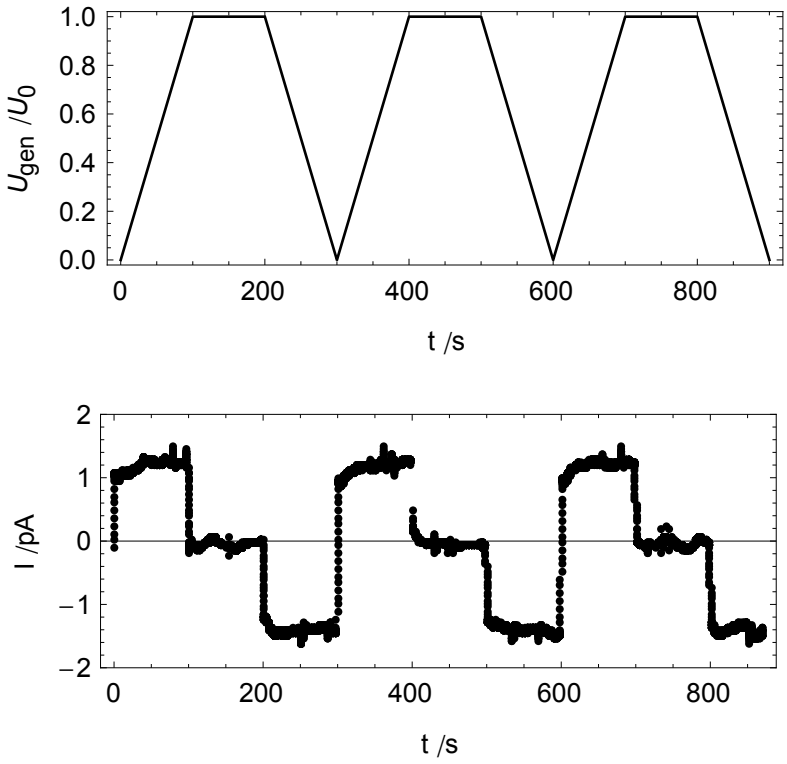

Figure 4.7: Calibration of the pA-meter. Top: Waveform of the generator output voltage. Bottom: Corresponding measured input current for $U_0 = 10$ V and $C_{ext} = 12.1$ pF. The input current is +1.2 pA for increasing input voltage, and -1.2 pA for decreasing input voltage. The uncertainty is about 2% for input currents in the pA range (stemming from the uncertainty on C_{ext}). For smaller currents, the largest uncertainty is caused by the offset currents that flow into the integrator input of the pA-meter, as these currents vary with time (see Fig. 4.6).

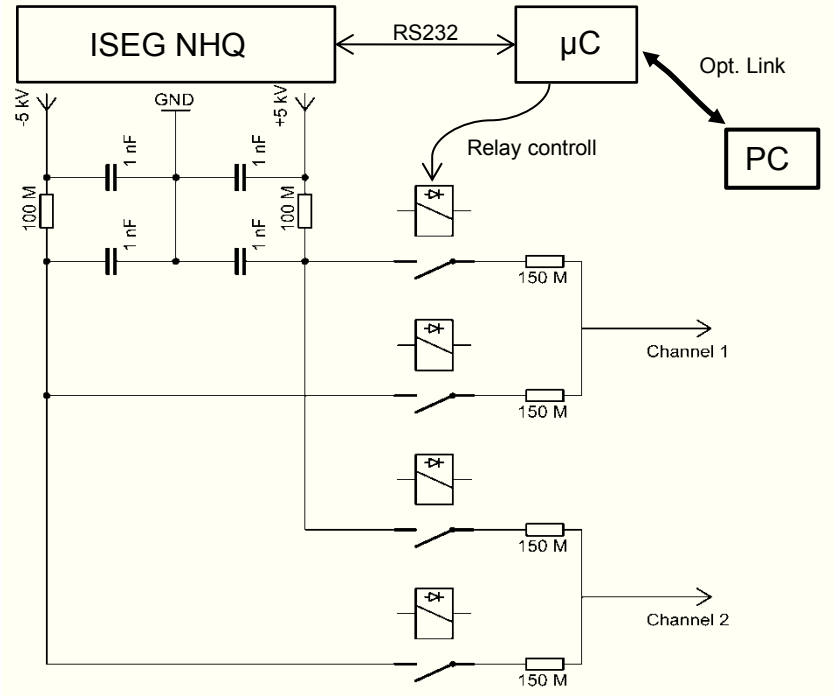

Figure 4.8: Schematic diagram of the High Voltage supply unit. A two-channel Iseg NHQ provides the positive and negative high voltages. The four relays are used to select the negative or positive voltage supply individually for each electrode. The relays and the NHQ are controlled by a micro controller that communicates with the measurement PC outside the shielded room via an optical serial interface.

The possibility to connect the electrodes to the negative or positive voltage individually has big advantages for systematic tests. For example, both electrodes could be set to +5 kV to investigate the influence of leakage currents that flow from the electrodes directly to the conductive housing at ground potential, while the electric field across the EDM cell is zero.
The relays and the NHQ are controlled by a micro-controller (Atmel XMEGA 32 A4) that communicates with the measurement PC outside the shielded room via an optical serial interface.

4.1.4 The SQUID and Data Acquisition System

The SQUID system uses a liquid helium cryostat manufactured by Cryoton. It is a low magnetic noise fiberglass model (LH-16.4-NTE) and was tested to contain no magnetizable material (e.g. small ferromagnetic particles). The cryostat has a total length of 900 mm and a diameter of 307 mm at the upper part. A finger with a smaller diameter 127 mm and a length of 200 mm is attached to the lower side. Here the distance between the inner volume at liquid helium temperature and the outside at room temperature is 14 mm. The inner volume (about 16 liters) is filled with liquid helium, which keeps the

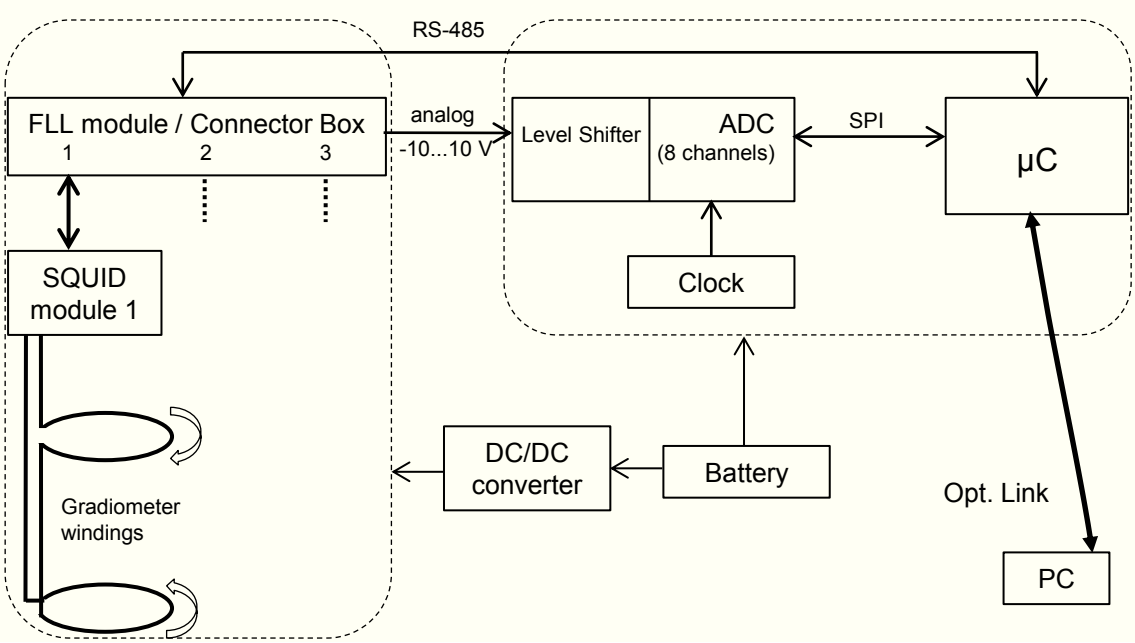

Figure 4.9: Principle of the SQUID data acquisition system. The left dashed box contains the components that have been developed and manufactured by Magnicon [94], whereas the power supply and the data acquisition system (right dashed box) have been developed in Heidelberg as a part of this thesis.

lower part of the dewar cold for eight days without refilling.
The SQUIDs, the corresponding electronics and mechanical supporting structures inside the dewar ("Probenstab") have been manufactured by Magnicon [94], while the data acquisition system was developed as a part of this dissertation.

The data acquisition system

Before explaining the components of the data acquisition system in detail, the whole set-up will be shortly summarized (see Fig. 4.9). Each individual gradiometer has a SQUID module in a niob shield at liquid helium temperature inside the cryostat. The three SQUID modules, that are used in this set-up, are controlled and read out by a three-channel FLL module, which is placed on top of the cryostat at room temperature. The connector box can connect several FLL modules (in case there are more than three gradiometers/magnetomters) and contains several filters (e.g. for the power supply). The SQUID system, as delivered by Magnicon, is shown schematically in Fig. 4.9 (left dashed box). It is controlled via RS-485, a very robust balanced serial interface widely used in low-speed communication for mostly industrial applications. The output signals of the SQUID electronics are analog voltage signals in the range of -10 to +10 V.
The development of the controlling unit of the SQUID electronics and the data acquisition system (DAQ) was a part of this doctoral thesis. The levels of the analog input signals are adjusted (amplitude and offset voltage) by a level shifter. Then the signals are digitalized by analog-to-digital converters (ADCs). The ADCs are controlled and

read out by a micro-controller that also communicates via RS-485 with the FLL module and via an optical link with the measurement PC. The whole system is placed inside the magnetically shielded chamber and battery-powered with the optical link being the only connection to the outside (the same principle as for the current sources, see p. 41; and the high-voltage system). Thus, environmental magnetic noise is effectively excluded from the measurement system.
The components of the DAQ have been chosen to meet the requirements with respect to noise, resolution, phase linearity, timing, and frequency of the sampling:
1) The noise level of the DAQ should not contribute significantly to the measured signal noise. The estimated magnetic noise due to impurities in the cryostat etc. is 2 $\mathrm{fT}/\sqrt{\mathrm{Hz}}$ and the intrinsic SQUID noise is comparable to that value. The SQUID calibration factor (the ratio between the output voltage and the magnetic field) is 20 mV/pT, typically (but this value depends on the area of the pick-up loop, the FFL gain and the the feedback resistor R_f). Thus, the the input noise level of the DAQ should be below $\sqrt{2} \cdot 2\ \mathrm{fT}/\sqrt{\mathrm{Hz}} \cdot 20\ \mathrm{mV/pT} = 56\ \mu\mathrm{V}/\sqrt{\mathrm{Hz}}$.
2) ADCs with a resolution of 24 bits are widely available in standard ICs. For 24 bit resolution at an input range from -10 to 10 V, 1 LSB corresponds to $20\ \mathrm{V}/(2^{24}-1) \approx 1.2\ \mu\mathrm{V}$, which is sufficient.
3) As the ^{3}He-^{129}Xe comagnetometer measures phases very precisely, it must be ensured that the phase of the measurement signal is not shifted. Especially components that shift the phase of the measurement signal depending on the frequency are very critical and have to be avoided. Low-pass filters (e.g. analog RC filters) that are usually present in DAQ systems as anti-aliasing filters have to be constructed very carefully. For example, if a simple RC anti-aliasing filter with a cut-off frequency ω_0 is applied, the phase shift is $\Delta\varphi(\omega) = -\arctan(\omega/\omega_0)$. For $\omega_0 = 2\pi \cdot 100$ Hz (for a ADC sampling frequency $f_s = 250$ Hz) and a 10^{-3} drift of the Larmor frequencies, this causes a shift in the weighted phase difference of $-1.8\ \mu$rad. This is just below the the actual sensitivity level of the comagnetometer of $\approx 10\ \mu$rad and should be avoided with regard to future sensitivity improvements (see below).
4) The Larmor frequencies are typically $\omega_{\mathrm{He}} \approx 2\pi \cdot 12$ Hz and $\omega_{\mathrm{Xe}} \approx 2\pi \cdot 5$ Hz ($B_0 \approx 400$ nT). In earlier measurements a sampling frequency of $f_s = 250$ Hz has proven to be a reasonable value to perform phase measurements on the precession signals, and to monitor noise sources like mechanical vibrations and power line radiation (50 and 100 Hz) while avoiding unnecessary large data files. This sampling frequency should be stable on the 10^{-6} level to monitor drifts of B_0. The sampling of the different channels should be simultaneous (and derived from the same clock, of course).
The following components have been chosen to build a DAQ system that meets the requirements:
The **ADC** ADS1299 from Texas Instruments is a low-noise, 8 channel, simultaneous-sampling, 24-bit, second-order delta-sigma converter with a built-in programmable gain amplifier and internal reference voltage. This chip was originally developed for medical instrumentation, especially ECG and EEG applications with some EEG-specific functions. These EEG specific components can be powered down to use the chip in a DAQ system. The input can be switched to balanced or unbalanced mode and the input amplifier can be programmed to a gain between 1 and 24. The input range is 0...5 V for gain=1 and unbalanced input. The sampling frequency can be selected $f_s = 2^N \cdot 250$ Hz

with $N = 0...6$ (via a variable digital decimation filter, see below for further information on the delta-sigma ADC principle). For $f_s = 250$ Hz and gain=1 the RMS-noise is $\sigma = 1.1$ μV which corresponds to an average noise amplitude spectral density of $\rho = 0.1$ $\mu\text{V}/\sqrt{\text{Hz}}$ in the frequency range from DC to 125 Hz. The ADC is controlled and read out via a SPI interface.
To shortly explain the principle and benefits of delta-sigma modulation: The analog input signal is fed into the positive-input of a difference amplifier, integrated, and then quantized by a comparator (1 bit ADC: 0 if the input voltage is smaller than 0 V; 1 otherwise). This value is latched with the modulation clock f_{Mod} (in this case $f_{\text{Mod}} = 1.024$ MHz) and fed back into the negative-input of the difference amplifier. The input signal is now encoded in a 1 bit stream with a frequency f_{Mod}. The advantage of delta-sigma ADCs is that most of the conversion process is implemented in the digital domain as the only analog components are the ones mentioned above. This results in a high performance with respect to noise and linearity. The 1 bit stream has to be further processed by digital filters. The digital decimation filter processes the 1 bit data stream with the frequency f_{Mod} and turns it into a 24 bit stream with a frequency of f_s. In this case the filter is an adjustable third order low-pass sinc-filter with the scaled Z-domain transfer function

$$|H(Z)| = \left|\frac{1 - Z^{-N_d}}{1 - Z^{-1}}\right|^3 \tag{4.2}$$

and the corresponding frequency domain transfer function is

$$|H(f)| = \left|\frac{\sin\left(\frac{N_d \pi f}{f_{\text{Mod}}}\right)}{N_d \cdot \sin\left(\frac{\pi f}{f_{\text{Mod}}}\right)}\right|^3 \tag{4.3}$$

with the selectable decimation ratio N_d (for a sampling frequency of $f_s = 250$ Hz the decimation ratio is 4096). The phase response is perfectly linear.
The input signal of the ADC is sampled with a frequency of $f_{\text{Mod}} = 1.024$ MHz that is independent of the final output sampling frequency f_s between 250 Hz and 16 kHz. Thus, the analog anti-aliasing filter can be a simple RC low-pass filter with cut-off frequency below $f_{\text{Mod}}/2$. In this case $f_{\text{RC}} = 7$ kHz was chosen.
An external temperature-stabilized quartz **oscillator** gives a $f_{\text{Osc}} = 2.048$ MHz clock for the ADCs.
As the ADC input range is 0...+5 V and the SQUID system has an -10...+10 V output range, AD8275 chips from Analog Devices were used as **level shifter**. These chips have internal matched precision laser-trimmed resistors that ensure low gain error, low temperature-dependent gain drift of less than 1 ppm/K, and a low voltage offset and drift (2.5 μV/K). The output voltage noise amplitude spectral density is 0.3 $\mu\text{V}/\sqrt{\text{Hz}}$ at 10 Hz.
The ADC is controlled and read out by a micro-controller (Atmel XMEGA 32 A4) that transmits the data to a measurement PC outside the shielded room via an optical serial interface.

4.2 Sensitivity Estimation

A permanent EDM $\boldsymbol{d}$ of a fundamental or composite particle must be aligned parallel to the spin as mentioned before. Thus, for a magnetic guiding field aligned along the z-direction, the Hamiltonian has the form $H = -\mu \cdot B_0 - d \cdot E_z$ with the corresponding frequency shift $\delta\omega_{\mathrm{EDM}} = \frac{2}{\hbar} d \cdot E_z$. By varying the z-component of the electric field E_z, the frequency shift is modulated correspondingly. Subsequently, a non-zero EDM would manifest in a modulation of the weighted phase difference, and the corresponding value d can be extracted.
To achieve maximum sensitivity, the electric field should be switched between the two extrema $\pm E_{z,0}$, i.e. parallel and anti-parallel to the magnetic guiding field (in the case of our EDM cell: $E_{z,0} = \frac{10\ \mathrm{kV}}{6\ \mathrm{cm}}$ with the typical voltage of 10 kV between the electrodes that are 6 cm apart).
The ^{3}He and ^{129}Xe Larmor frequencies are

$$\begin{aligned} \omega_{\mathrm{He}} &= \gamma_{\mathrm{He}} B_0 \\ \omega_{\mathrm{Xe}} &= \gamma_{\mathrm{Xe}} B_0 + \frac{2}{\hbar} E_z(t) \cdot d \end{aligned} \tag{4.4}$$

with corresponding weighted frequency difference

$$\Delta\omega(t) = \omega_{\mathrm{He}} - \frac{\gamma_{\mathrm{He}}}{\gamma_{\mathrm{Xe}}} \omega_{\mathrm{Xe}} = -\frac{\gamma_{\mathrm{He}}}{\gamma_{\mathrm{Xe}}} \frac{2}{\hbar} E_z(t) \cdot d \ . \tag{4.5}$$

If E_z is constant, then the weighted phase difference is

$$\Delta\Phi_{\mathrm{EDM}}(t) = -\frac{\gamma_{\mathrm{He}}}{\gamma_{\mathrm{Xe}}} \frac{2}{\hbar} E_z \cdot d \cdot t \ . \tag{4.6}$$

For an electric field, that is periodically switched between $\pm E_{z,0}$ like in Fig. 4.10 (top) (square wave with period T_a, i.e. the voltage is reversed after the time $T_a/2$), the weighted phase difference is proportional to the triangular wave $h(t, T_a)$ with period T_a and amplitude 1 (see Fig. 4.10 (bottom)):

$$\Delta\Phi_{\mathrm{EDM}}(t) = -\frac{\gamma_{\mathrm{He}}}{\gamma_{\mathrm{Xe}}} \frac{2}{\hbar} E_{z,0} \cdot d \cdot T_a \cdot h(t, T_a) \ . \tag{4.7}$$

T_a can be chosen freely for the measurement. It has a large influence on the sensitivity, and thus, the optimal value has to be determined.
To do so, the data of a single run of the Lorentz invariance measurements (lasting about 24 hours, $T^*_{2,\mathrm{Xe}} = 8.5$ h, combined data of four gradiometers) are analyzed as if a time dependent electric field $E_z(t)$ had been present during the measurement. The appropriate function that describes all deterministic phase shifts as before (chemical shift, Earth's rotation, Ramsey-Bloch-Siegert shift) and now contains the parameterization of an EDM induced phase shift ($g \cdot h(t, T_a)$)

$$\begin{aligned} \Delta\Phi_{\mathrm{fit}}(t) = {} & \Phi_0 + \Delta\omega_{\mathrm{lin}} \cdot t + E_{\mathrm{He}} \cdot e^{\frac{-t}{T^*_{2,\mathrm{He}}}} + E_{\mathrm{Xe}} \cdot e^{\frac{-t}{T^*_{2,\mathrm{Xe}}}} \\ & + F_{\mathrm{Xe}} \cdot e^{\frac{-2t}{T^*_{2,\mathrm{He}}}} + F_{\mathrm{He}} \cdot e^{\frac{-2t}{T^*_{2,\mathrm{Xe}}}} + g \cdot h(t, T_a) \end{aligned} \tag{4.8}$$

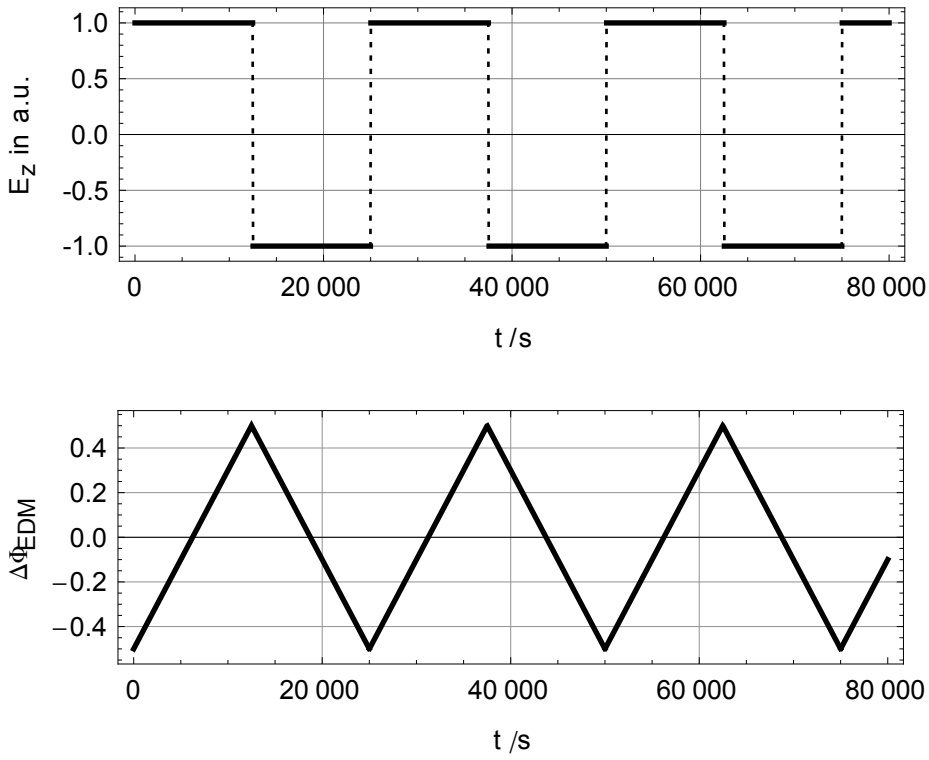

Figure 4.10: An electric field that is periodically switched between $\pm E_{z,0}$ with a period T_a (i.e. the voltage is reversed after the time $T_a/2$) causes a signal in the weighted phase difference that is proportional to a triangular wave for a non-zero EDM (here $T_a = 25000$ s). The voltage can be switched in about half a minute, which can be considered as instantaneous compared to T_a.

with different switching periods T_a is fitted to the weighted phase difference data. Estimations for the fit parameter values Φ_0, $\Delta\omega_{\mathrm{lin}}$, $E_{\mathrm{He/Xe}}$, $F_{\mathrm{He/Xe}}$ and g including their correlated and uncorrelated uncertainties are extracted. In the next step d can be calculated from g:

$$d = -\frac{\gamma_{\mathrm{Xe}}}{\gamma_{\mathrm{He}}}\frac{\hbar}{E_{z,0}\cdot T_a}\cdot g\ . \tag{4.9}$$

The corresponding uncorrelated and total (combination of uncorrelated and correlated) uncertainties δd are determined for different switching periods T_a. Here $E_{z,0} = \frac{10\ \mathrm{kV}}{6\ \mathrm{cm}}$ was assumed. The results can be found in Fig. 4.11. As expected, the uncorrelated uncertainty on d decreases with $1/T_a$, because the uncorrelated uncertainty on g is almost independent of T_a. For $T_a < 10000$ s the correlated uncertainty is negligible, because the correlation between the triangular function $h(t, T_a)$ describing the EDM induced phase shift and the other terms describing deterministic phase shifts is very small. In this regime, the total uncertainty is dominated by the uncorrelated uncertainty. However, with larger T_a, the correlation increases (especially with the exponential terms describing the Ramsey-Bloch-Siegert shift) resulting in correlated uncertainties that are a factor of ≈ 20 higher than the uncorrelated one for $T_a > 70000$. This problem is well known from the Lorentz invariance violation measurements where the modulation has an unfavorable period of a sidereal day (86164 s). For the EDM measurements, the period of the modulation can be chosen freely, and the optimum is found at $T_a =$ 20000...30000 s (see Fig. 4.11), i.e. the voltage between the two electrodes should be reversed every $T_a/2 = 10000...15000$ s. Then the correlated uncertainty is almost equal to the uncorrelated uncertainty of $\delta d = 1\cdot 10^{-28}$ ecm, resulting in a total uncertainty of $\delta d = 2\cdot 10^{-28}$ ecm. This is the achievable statistical sensitivity on the ^{129}Xe EDM within a single measurement run lasting one day assuming that the experimental conditions are the same as for the Lorentz invariance violation measurements (e.g. SNR, T_2^*). For shorter $T^*_{2,\mathrm{Xe}}$, the optimal T_a will shift to smaller values. Thus, the optimal T_a should be re-evaluated for the actual EDM measurement conditions.

4.3 Estimation of Systematic Effects

As this experiment is aiming at the 10^{-29} ecm sensitivity level (after about 100 days of measurement time), much effort has to be put into the investigation of systematic effects. In this section, possible systematic effects and measurement strategies to detect or avoid them will be discussed.

Effects that have a time dependence similar to the EDM induced phase shift must be excluded. Otherwise it would be possible that these effects mask the EDM leading to a false negative result - or produce a false positive result by a fake signal. Special care has to be taken to avoid (or minimize) effects that change sign as the electric field is inverted. Such effects ("false EDM effects") would not be distinguishable from a true EDM. In particular, high voltage correlated magnetic fields have to be considered. There are two effects that are caused by the gradients of such fields: Firstly, due to different centers of masses of ^{3}He and ^{129}Xe, comagnetometry becomes imperfect in the presence of gradients ("gravitational shift", see page 56). Secondly, the magnetic field

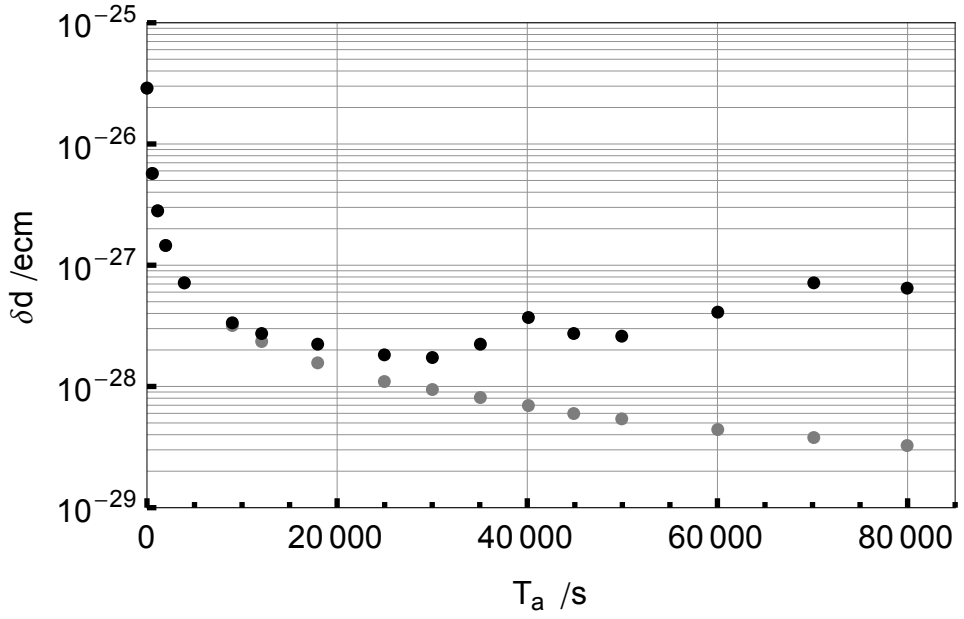

Figure 4.11: The data of a single Lorentz invariance measurement run lasting about 24 hours ($T^*_{2,\mathrm{Xe}} = 8.5$ h, combined data of four gradiometers) were analyzed as if a electric field $E_z(t)$ (periodically switched between parallel and anti-parallel to the magnetic guiding field) had been present during the measurement. The resulting uncorrelated (gray) and total uncertainties (black) δd are determined for different switching periods T_a.

gradients influence the transverse relaxation times T_2^*. The resulting gradients are the superposition of the gradients produced by the coils and the mu-metal shielding, and the magnetic field gradients that are correlated with the high voltage. For example, T_2^* may be increased for one direction of the electric field and decreased for the other direction. T_2^* has a direct impact on the Ramsey-Bloch-Siegert shift, and therefore, this might cause a false signal in the weighted phase difference.
Possible sources of high voltage correlated magnetic fields are leakage currents, the displacement current during polarity reversal of the electric field, or motional magnetic fields. These effects will be discussed in the following sections.

4.3.1 Leakage Currents

The electrodes of the EDM cell are 6 cm apart and separated partially by the glass wall, the inner gas volume (mixture of He, Xe and SF_6, total pressure about 50 mbar), and the outer gas volume inside the conductive housing (SF_6, 1 bar).
However, small leakage currents can flow on the surface of the glass wall or directly through the gas volume (ionized gas atoms). The leakage current is monitored by the pA-meters and is approximately 1 pA at a voltage of 1 kV (see Fig. 4.4).
If a leakage current $I = 10$ pA flows in a straight line between the electrodes on the outside of the glass wall, then the maximum gradients will be about $7 \cdot 10^{-16} \frac{\mathrm{T}}{\mathrm{cm}}$ (directly in the proximity of the current path). With the distance of the two centers of mass $\Delta\overline{z} = 0.31$ μm (see Eq. (2.66) on p. 56) this would lead to a gravitational shift of $4 \cdot 10^{-12}$ rad/s, which is negligible small. The influence on T_2^* is also expected to be of no further concern, as these gradients are much smaller than the gradients of the mu-metal shielding and the coils (≈ 30 pT/cm). If the leakage current flows in a single loop around the cell, then the maximum gradients will be on the same order of magnitude.
However, the influence of leakage currents can be experimentally tested by a controlled current in the proximity of the measurement cell, e.g. with a wire made of conductive plastic that connects the two electrodes at the surface of the glass wall. Then a current of about 10 nA (three orders of magnitude higher than the actual leakage currents) is send through the wire. Changes in the weighted phase difference and T_2^* are measured. Subsequently, the upper limits on false EDM effects for the smaller actual leakage currents (10 pA) can be determined. Furthermore, the performance of the comagnetometer can be tested by varying the magnitude of the magnetic guiding field (e.g. $B_0 = 400$ nT for three hours, then $B_0 = 410$ nT for three hours, ...) and looking for changes in T_2^* (which will change with the gradients) and the weighted phase difference.

4.3.2 Magnetic Field During Polarity Reversal

The direction of the electric field has to be inverted several times during a single measurement run (i.e. every few hours, see previous section). The corresponding magnetic field, that is generated by the displacement current during polarity reversal, can be calculated using Maxwell's equations:

$$\nabla \times \boldsymbol{B} \;=\; \mu_0 \boldsymbol{j} + \mu_0 \epsilon_0 \frac{\partial \boldsymbol{E}}{\partial t} \quad . \tag{4.10}$$

A change in the high voltage creates a magnetic field which is equivalent to the field of a constant current density between the two capacitor plates. The total current is

$$I = C \cdot \frac{dU}{dt} \quad . \tag{4.11}$$

The capacity is $C \approx 10^{-13}$ F, and if the voltage is slowly inverted within 200 s, then the current is $I = 10^{-13}$ F $\cdot \frac{20 \text{ kV}}{200 \text{ s}} = 10$ pA. The magnetic field strength of such a configuration is $|\boldsymbol{B}(r)| = \frac{\mu_0 I}{2\pi} \cdot \frac{r}{R^2}$ for $r < R$ and $|\boldsymbol{B}(r)| = \frac{\mu_0 I}{2\pi} \cdot \frac{1}{r}$ for $r \geq R$, where R is the radius of the cylindrical glass cell. With $R = 5$ cm and the values above this is $|\boldsymbol{B}| = \frac{\mu_0 I}{2\pi} \cdot \frac{1}{R} = 2 \cdot 10^{-17}$ T with gradients in the order of $4 \cdot 10^{-18} \frac{\text{T}}{\text{cm}}$. These gradients are even lower than the gradients produced by the "concentrated" leakage current on the surface of the glass wall.
Additionally, the noise of the high voltage source causes fluctuating displacement currents that produce magnetic noise. Assuming a RMS noise of 5 mV at 10 Hz the fluctuating current is

$$I = C \cdot \frac{dU}{dt} \approx 10^{-13} \text{ F} \cdot \frac{5 \text{ mV}}{0.1 \text{ s}} = 5 \cdot 10^{-15} \text{ A} \tag{4.12}$$

with immeasurably low corresponding magnetic noise.

4.3.3 Motional Magnetic Field

The hyper-polarized gas atoms are at room temperature $T = 300$ K and move randomly around the EDM cell. The RMS speed is

$$v_{\text{rms}} = \sqrt{\frac{3RT}{M}} = \begin{cases} 1578 \text{ m/s for } ^3\text{He} \\ 241 \text{ m/s for } ^{129}\text{Xe} \end{cases} , \tag{4.13}$$

where $R = 8.3$ J/(K mol) is the molar gas constant and M are the molar masses ($M = 3$ g/mol for ^{3}He and $M = 129$ g/mol for ^{129}Xe).
A magnetic field $\boldsymbol{B_m}$ is observed in the rest frame of the gas atom when moving with a velocity $\boldsymbol{v}$ relative to the source of an electric field $\boldsymbol{E}$. For speeds $v \ll c$ (i.e. the relativistic factor $\gamma \approx 1$), this motional magnetic field is:

$$\boldsymbol{B_m} = \frac{1}{c^2} \cdot \boldsymbol{E} \times \boldsymbol{v} \quad .$$

For example, the motional magnetic field is $B_m \approx 3$ nT for a particle that moves with a speed of $v = 1500$ m/s (realistic velocity for a ^{3}He atom in the measurement cell) perpendicular to the electric field of magnitude $E = 1.7$ kV/cm. The motional magnetic field and the static magnetic field $\boldsymbol{B_0}$, which is produced by the coils, contribute to the effective magnetic field $\boldsymbol{B}$, which is seen by the individual gas atoms:

$$\boldsymbol{B} = \boldsymbol{B_0} + \boldsymbol{B_m} \quad . \tag{4.14}$$

The magnitude of the resulting field can be expressed by:

$$\begin{aligned} B &= B_0 + \Theta_{EB} B_m + \frac{1}{2} \frac{B_m^2}{B_0} \quad , (B_m \ll B_0) \\ &= B_0 + \frac{\Theta_{EB} \cdot v \cdot E}{c^2} + \frac{v^2 E^2}{2c^4 B_0} \quad , \end{aligned} \tag{4.15}$$

where Θ_{EB} is the angle between $\boldsymbol{E}$ and $\boldsymbol{B_0}$ in the plane perpendicular to $\boldsymbol{v}$. Equation (4.15) has a term that is linear in v, and one that is quadratic in v. Both are discussed in detail in Refs. [96–98] with a focus on the neutron EDM.
Concerning the **linear effect**: For storage experiments (like the ^{3}He-^{129}Xe comagnetometer), in principle, the average velocity is zero[1]. However, it must be tested, how well this averaging works. Similar to gradients in the magnetic guiding field $\boldsymbol{B_0}$, randomly fluctuating motional magnetic fields cause a faster depolarization and a tiny frequency shift (see section "transverse relaxation" on p. 38). As the linear effect only occurs in case of a misalignment between the electric and magnetic field ($\Theta_{EB} \neq 0$), one should attempt to keep Θ_{EB} as small as possible. However, it has to be pointed out, that the requirements concerning alignment are much more stringent in the neutron EDM experiments, as in that case the average velocity is non-zero. Especially for beam experiments, this effect was the final systematic limitation, which will be demonstrated here: The Oak Ridge apparatus, that had been moved to the ILL, used a neutron beam with a velocity of 100 m/s and an electric field of roughly 100 kV/cm in their last experiment (performed in the year 1977). The corresponding motional magnetic field was in the order of 10 nT. To determine the neutron EDM with an uncertainty smaller than $1.5 \cdot 10^{-24}$ ecm, the alignment should have been better than $\Theta_{EB} = 10^{-5}$ rad [97], which is certainly not an easy task. Therefore, storage experiments are much more favorable. The influence of the linear effect in the ^{3}He-^{129}Xe comagnetometer experiment can be tested by maximizing Θ_{EB}. An electric field that is perpendicular to B_0 must be switched on and off periodically, and the corresponding change in the weighted phase difference has to be monitored to extract the magnitude of such an false EDM effect. Then upper limits on this systematic uncertainty for the "aligned case" ($\Theta_{EB} < 2°$ should be easily reached) can be determined.
The determination of the xenon EDM using the ^{3}He-^{129}Xe comagnetometer with relatively large partial pressures in the order of several mbar has an other systematic advantage in comparison to the determination of the neutron EDM in storage experiments: As neutron EDM experiments use very low neutron densities, particles might get on a circular orbit in a cylindrical vessel, if collisions are dominated by wall interaction (and not by particle-particle interactions). This would lead to a non-zero motional magnetic field (linear effect). This is called the "geometric phase effect".
If one compares the strength of these systematic effects in neutron EDM experiments and in this ^{129}Xe EDM experiment, one finds, that in neutron EDM experiments one must put much more effort into the alignment of the electric and magnetic field.
Concerning the **quadratic effect**: The quadratic term in Eq. (4.15) persists, even if the average velocity of the particles in the measurement cell is zero. Furthermore, it is independent of the alignment of electric and magnetic guiding field. To determine the effects of this quadratic term, one must consider the stochastic movement of the gas particles in the measurement cell. The motional magnetic field has a definite direction and magnitude for a time interval τ_c, which is the mean time between velocity changes due collisions of a gas particle (with another particle or the wall). The parameter τ_c depends on the density, the temperature, and the collision cross section of the gas in the mea-

[1] An exception could be a circular flow (e.g. caused by heat gradients) in an inhomogeneous electric field.

surement cell. For the gas atoms in the measurement cell (total pressure ≈ 35 mbar), the mean free path is ≈ 2 μm and $\tau_c \approx 1$ ns. For a spin-1/2 system, the net effect of the randomly fluctuating field can be quantitatively calculated using a density matrix formalism, which was done by Lamoreaux and Golub [97]. The result can be expressed as an 2x2 relaxation matrix, where the real components represent the spin relaxation, while the imaginary components of the off-diagonal elements represent a frequency shift. For $\gamma B_0 \cdot \tau_c \ll 1$, which is the case for the ^{3}He-^{129}Xe comagnetometer, the relaxation rate is

$$r = \frac{1}{4}(\gamma \frac{v}{c^2} E)^2 \tau_c \tag{4.16}$$

and the frequency shift is

$$\delta\omega = \frac{(2\pi)^3}{9}(\gamma \frac{v}{c^2} E)^2 \gamma B_0 \tau_c^2 \quad . \tag{4.17}$$

As mentioned before, one must carefully look for frequency shifts that change sign if one inverts the electric field. For the quadratic term, this is not the case, the shift is independent of the direction of the electric field (the frequency shift is always positive). However, a false EDM effect would arise if the magnitude of the electric field would not be exactly the same after polarity reversal.
Here, the ^{3}He-^{129}Xe comagnetometer benefits from a short correlation time and a relatively low electric field ($E = 1.7$ kV/cm). Typical values are $r = 10^{-10}$ s^{-1} and $\delta\omega = 10^{-15}$ Hz, which can be neglected at the current sensitivity level. However, one should perform systematic measurements, where one varies the magnitude of the electric field and looks for effects on phase and relaxation.

4.4 Summary and Outlook

In this chapter, I have presented the technical developments and modifications of the experimental set-up that have been implemented as a part of this thesis.
The sensitivity of the comagnetometer with respect to the EDM was estimated based on the Lorentz invariance violation data. Under the premise that the same signal-to-noise ratio and spin coherence times can be reached, the result is promising: After one day of coherent spin precession, the uncertainty on the EDM is $\delta d \approx 2 \cdot 10^{-28}$ ecm. This is one order of magnitude better than the current best limit by M. A. Rosenberry and T. E. Chupp [73, 74].
As this experiment is aiming at the 10^{-29} ecm sensitivity level (which can be reached after about 100 days of measurement time), much effort has to be put into the investigation of systematic effects. It must be excluded that systematic effects mask the EDM leading to a false negative result - or produce a false positive result by a fake signal. Special care must be taken to avoid (or minimize) effects that change sign as the electric field is inverted. Such effects ("false EDM effects") would not be distinguishable from a true EDM. In particular, high voltage correlated magnetic fields have to be considered. There are two effects that are caused by the gradients of such fields: Firstly, due to different centers of masses of ^{3}He and ^{129}Xe, comagnetometry becomes imperfect in the presence of gradients (gravitational shift). Secondly, the magnetic field gradients

influence the transverse relaxation times T_2^*. T_2^* has a direct impact on the Ramsey-Bloch-Siegert shift, and therefore, this might cause a false signal in the weighted phase difference. Possible sources of high voltage correlated magnetic fields are leakage currents, the displacement current during polarity reversal of the electric field, or motional magnetic fields.
The next steps to actual ^{129}Xe EDM measurements include tests of the magnetically shielded room in Jülich and the whole set-up with respect to both magnetic noise and gradients, as these values have a large influence on the attainable statistical uncertainty. Furthermore, the effect of the applied high voltage on relaxation rates and frequency shifts must be tested extensively. Then, a sensitivity of $\delta d \approx 10^{-28}$ ecm can be reached with first measurement runs. Finally, a measurement period of about 100 days follows, which is long enough to accumulate data for a statistical uncertainty on the $\delta d \approx 10^{-29}$ ecm level.

5 Conclusion and Outlook

To summarize the preceding chapters, and to point out the benefit of high-precision experiments at low energies once again:
It is widely believed that the Standard Model (SM) together with General Relativity (GR) is a low-energy manifestation of a more complete theory, that perhaps unifies the four fundamental interactions, or at least describes gravity at the quantum level. Many extensions to the SM have been proposed, and these give predictions for physical phenomena that differ from those of the SM. Some searches for new physics beyond the standard model are performed at high-energy particle colliders. There the new processes or particles would be seen directly if the energy would be sufficient to produce them. However, the effects (e.g. of a theory of quantum gravity) would become apparent at high energy scales (e.g. the Planck scale $m_P \approx 10^{19}$ GeV) that is by far out of reach for particle colliders.
As an alternative, a very sensitive probe can be constructed at low energies through precision measurements of quantities, that can be described by the SM. Then physics beyond the standard model would become apparent indirectly through a deviation of the measured values from the SM predictions. The precision measurements, that are the topic of this dissertation, are of this kind:

Firstly, a small amount of the large effects of quantum gravity at the Planck scale should remain at low energies. This can be tested by looking for a violation of Lorentz invariance in the neutron sector. As a central part of this dissertation, the experiments and methods of data evaluation have been described that put a limit on a Lorentz invariance and CPT violating coupling of the (bound) neutron spin $\boldsymbol{\sigma^n}$ to a hypothetical background field $\tilde{\boldsymbol{b}}^{\boldsymbol{n}}$. Such a coupling of the form

$$V = -\tilde{\boldsymbol{b}}^{\boldsymbol{n}} \cdot \boldsymbol{\sigma^n} \tag{5.1}$$

is motivated within the minimal Standard Model Extension. The experimental result was found to be compatible with zero:

$$\begin{aligned} \tilde{b}_X^{\mathrm{n}} &= (5.1 \pm 4.9) \cdot 10^{-34}\ \mathrm{GeV} \\ \tilde{b}_Y^{\mathrm{n}} &= (3.6 \pm 7.8) \cdot 10^{-34}\ \mathrm{GeV}\ . \end{aligned} \tag{5.2}$$

The corresponding upper limits on the equatorial component are

$$\begin{aligned} \tilde{b}_\perp^{\mathrm{n}} &< 8.4 \cdot 10^{-34}\ \mathrm{GeV} \quad (68\%\ \text{Confidence Level}) \\ \tilde{b}_\perp^{\mathrm{n}} &< 1.6 \cdot 10^{-33}\ \mathrm{GeV} \quad (95\%\ \text{Confidence Level})\ . \end{aligned} \tag{5.3}$$

This is an improvement by a factor of 50 compared to the year 2009 measurements with the ^{3}He-^{129}Xe comagnetometer [37] and an improvement by a factor of 4 compared to the former best limit measured by a ^{21}Ne-Rb-K comagnetometer [13].

Furthermore, the data can be used to extract the corresponding limits on proton interactions: $\tilde{b}_{\perp}^{\mathrm{p}} < 1.6 \cdot 10^{-33}$ GeV.
In addition, measurements using a slowly rotating magnetic guiding field have been described. Though the results of these measurements did not flow into the final limits on Lorentz invariance violation, a lot of knowledge about the behavior of the comagnetometer, the mu-metal shielding, and the measurement system etc. could be derived. Finally, this led to an optimization procedure with respect to gradient relaxation that will be also applied in future measurements. Spin coherence could be maintained for a very long time with $T_{2,Xe}^{*} \approx 8.5$ h and $T_{2,He}^{*} \approx 100$ h.

Secondly, new sources of CP violation would cause permanent EDMs of particles that are many orders of magnitude larger than the EDMs predicted by the SM. Therefore, experiments that put limits on EDMs can rule out (or at least narrow down) such models; or if they detect one, will have an unambiguous evidence of new physics. Historically, the stringent limit on the neutron EDM has ruled out more speculative models than any other single experimental approach in particle physics. EDM precision measurements in various systems with different sensitivities will continue to constrain proposed models of physics beyond the standard model. The various searches for CP violation are a good example of how low- and high-energy experiments are complementary to each other.
Several technical developments and modifications of the experimental set-up were implemented as a part of this thesis. The sensitivity of the comagnetometer with respect to the EDM was estimated based on the Lorentz invariance violation data. Under the premise that the same signal-to-noise ratio and spin coherence times can be reached, the result is promising: After one day of coherent spin precession, the uncertainty on the EDM is $\delta d \approx 2 \cdot 10^{-28}$ ecm, which would be one order of magnitude better than the current best limit. In the long run, this experiment is aiming at the 10^{-29} ecm sensitivity level (which can be reached after about 100 days of measurement time). Therefore, much effort has to be put into the investigation of systematic effects. Special care must be taken to avoid (or minimize) effects that change sign as the electric field is inverted, as such false EDM effects would not be distinguishable from a true EDM. In particular high voltage correlated magnetic fields have to be considered.
To give an outlook: The next steps to actual ^{129}Xe EDM measurements include tests of the magnetically shielded room in Jülich and the whole set-up with respect to both magnetic noise and gradients, as these values have a large influence on the attainable statistical uncertainty. Furthermore, the effect of the applied high voltage on relaxation rates and frequency shifts must be tested extensively. Then, a sensitivity of $\delta d \approx 10^{-28}$ ecm can be reached with first measurement runs. Finally, a measurement period of about 100 days follows, which is long enough to accumulate data for a statistical uncertainty on the $\delta d \approx 10^{-29}$ ecm level.

Appendix

A Calculations concerning the Lorentz invariance violation measurements

A.1 Calculation of the phase and amplitude relations of the SME parameters with respect to different measurement directions

The measurements that are described in Chapter 3 (putting limits on Lorentz invariance violation) have been performed under two different measurement directions (for runs 1 to 3 the magnetic guiding field pointed roughly to the south-south-west $\rho_1 = 208°$, and for runs 4 to 7 to east-north-east $\rho_2 = 73°$). The phase and amplitude relations for different measurement directions will be derived in the following paragraph:
A coordinate system $(\hat{X}, \hat{Y}, \hat{Z})$ is defined with $\hat{Z}$ being parallel to Earth's rotation axis. This coordinate system is fixed with respect to distant stars if one neglects the Earth's precession movement. The $\hat{X}$ axis is determined by the vernal equinox (equatorial coordinate system).
In the lab system one describes the direction of the spins (or the direction of the magnetic guiding field) with: horizontal direction, latitude Θ and geographic direction ρ. Projection of the spin direction at the time $t = 0$, when the laboratory lies in the $\hat{X}$-$\hat{Z}$ plane, on to the coordinate axes $(\hat{X}, \hat{Y}, \hat{Z})$ results in:

$$\begin{pmatrix} x \\ y \\ z \end{pmatrix}_{t_0} = \begin{pmatrix} \sin(\Theta) \cdot \cos(\rho) \\ \sin(\rho) \\ \cos(\Theta) \cdot \cos(\rho) \end{pmatrix} \tag{A.1}$$

At an arbitrary time with Earth rotation (rotation frequency is the sidereal frequency Ω_s):

$$\begin{aligned} \vec{r}(t) &= \begin{pmatrix} \cos(\Omega_s t) & \sin(\Omega_s t) & 0 \\ -\sin(\Omega_s t) & \cos(\Omega_s t) & 0 \\ 0 & 0 & 1 \end{pmatrix} \begin{pmatrix} \sin(\Theta) \cdot \cos(\rho) \\ \sin(\rho) \\ \cos(\Theta) \cdot \cos(\rho) \end{pmatrix} \\ &= \begin{pmatrix} \sin(\rho) \cdot \sin(\Omega_s t) + \sin(\Theta) \cdot \cos(\rho) \cdot \cos(\Omega_s t) \\ \sin(\rho) \cdot \cos(\Omega_s t) - \sin(\Theta) \cdot \cos(\rho) \cdot \sin(\Omega_s t) \\ \cos(\Theta) \cdot \cos(\rho) \end{pmatrix} \end{aligned} \tag{A.2}$$

The frequency shift due to an Lorentz invariance violating background field is:

$$\Omega_{LV}(t) = \frac{\left\langle \tilde{b} \right\rangle}{\hbar} \hat{\epsilon} \cdot \vec{\sigma} \tag{A.3}$$

$$= \frac{\left\langle \tilde{b} \right\rangle}{\hbar} \begin{pmatrix} \epsilon_x \\ \epsilon_y \\ \epsilon_z \end{pmatrix} \cdot \vec{r}(t)$$

$$= \frac{\left\langle \tilde{b} \right\rangle}{\hbar} \cdot [\epsilon_x \cdot (\sin(\rho) \cdot \sin(\Omega_s t) + \sin(\Theta) \cdot \cos(\rho) \cdot \cos(\Omega_s t))$$
$$+ \epsilon_y \cdot (\sin(\rho) \cdot \cos(\Omega_s t) - \sin(\Theta) \cdot \cos(\rho) \cdot \sin(\Omega_s t))$$
$$+ \epsilon_z \cdot \cos(\Theta) \cdot \cos(\rho)] \tag{A.4}$$

$$=: \frac{\left\langle \tilde{b} \right\rangle}{\hbar} \cdot [(c'_{11}\epsilon_x + c'_{22}\epsilon_y)\cos(\Omega_s t) + (c'_{12}\epsilon_x + c'_{21}\epsilon_y)\sin(\Omega_s t) + const_1] \tag{A.5}$$

To get the phase one integrates over time:

$$\Phi_{LV}(t) = \int_{t_0}^{t} \Omega_{LV}(t')dt' \tag{A.6}$$

$$= const_2 + lin \cdot t + \frac{\left\langle \tilde{b} \right\rangle}{\hbar\Omega_s}[(c'_{11}\epsilon_x + c'_{22}\epsilon_y)\sin(\Omega_s t) - (c'_{12}\epsilon_x + c'_{21}\epsilon_y)\cos(\Omega_s t)] \tag{A.7}$$

The constant and linear terms can not be measured in our experiment, and therefor they are neglected in the following equations.
Thus:

$$\Phi_{LV}(t) = \frac{\left\langle \tilde{b} \right\rangle}{\hbar\Omega_s}[-\sin(\rho)\epsilon_x \cos(\Omega_s t) + \cos(\rho)\sin(\Theta)\epsilon_x \sin(\Omega_s t)$$
$$+ \sin(\rho)\epsilon_y \sin(\Omega_s t) + \cos(\rho)\sin(\Theta)\epsilon_y \cos(\Omega_s t)] \tag{A.8}$$

This is equivalent to:

$$\Phi_{LV}(t) = \frac{\left\langle \tilde{b} \right\rangle}{\hbar\Omega_s}[A \cdot \epsilon_x \cdot \sin(\Omega_s t + \varphi) + A \cdot \epsilon_y \cdot \cos(\Omega_s t + \varphi)] \tag{A.9}$$

with

$$A = \sqrt{\sin^2\rho + \sin^2\Theta \cdot \cos^2\alpha}$$
$$\varphi = \arctan[-\tan\rho / \sin\Theta] \quad . \tag{A.10}$$

In our case with $\Theta = 52.52°$, $\rho_1 = 208°$, $\rho_2 = 73°$ this results in $A_1 = 0.84$, $A_2 = 0.98$, $\varphi_1 = -0.55$ and $\varphi_2 = -1.33$.
If one now chooses $t = 0$ with a sidereal phase $\varphi_{SD} \neq 0$, this phase has to be added: $\varphi_{1,2} \to \varphi_{1,2} + \varphi_{SD}$. In our case with $\varphi_{SD} = 0.104 \cdot 2\pi$: $\varphi_1 = 0.103$ and $\varphi_2 = -0.677$.
Comment: A is called $\sin\chi$ in the [53].

A.2 Using the data of several gradiometers

The data of several gradiometers or magnetometers can only be combined if they can be considered as independent measurements. In other words: the intrinsic SQUID noise must dominate over external noise in order to combine the gradiometers or magnetometers. Therefore one has to look for correlation in the noise of the measured SQUID signals. Correlated noise in the SQUID signals may be produced for example by a noisy current source that causes a noise in the magnetic guiding field that is seen by all gradiometers. On the other hand, the intrinsic SQUID noise is uncorrelated.
In the following figures a small set of data is shown. The data have been split into smaller sub-sets with 800 data points (3.2s) each. Then a fit to the data of each sub-set has been performed with the fit function

$$a_0 + a_1 \cdot t + b_1 \cdot \cos(\omega_{He} t) + b_2 \cdot \sin(\omega_{He} t) + c_1 \cdot \cos(\omega_{Xe} t) + c_2 \cdot \sin(\omega_{Xe} t) \ . \quad \text{(A.11)}$$

Then this fitted function was subtracted from the data points (calculation of residuals). Thus, only the noise remained. The noise data of two gradiometers or magnetometers are now available in time series

$$x(i \cdot \Delta t) \text{ and } y(i \cdot \Delta t) \text{ with } i = 1...N \text{ and } \Delta t = \frac{1}{f_{\text{sampling}}} = 4 \text{ ms} \ . \quad \text{(A.12)}$$

The following tests have been performed:

- **Scatter plots:** One forms a set of points of the form $(\frac{x(i\cdot\Delta t)}{\sigma_x}, \frac{y(i\cdot\Delta t)}{\sigma_y})$. These points are plotted. One would expect that all points lie on a straight line if the data are perfectly linearly correlated. Complex (non-linear) correlation should manifest in the formation of patterns. On page 130 one can find the scatter plots for all combinations of the gradiometers Z2K-Z7K, Z2E-Z7E, Z3F-Z7F and Z1E+Z9E, which are used for the evaluation of the Lorentz invariance violation data (800 points each). Apparently there is no pattern.
  On page 132 (left) one can find the scatter plot for the combination of the single magnetometers Z2K and Z7K. One can clearly see a small correlation.

- **Cross- and auto-correlation:** One calculates the sums:
  $\bar{\rho}(\tau) = \frac{1}{N\sigma_x\sigma_y} \sum_{i=1}^{N} x(i \cdot \Delta t) \cdot y(i \cdot \Delta t + \tau)$
  These values are plotted as a function of τ for all combinations of the gradiometers Z2K-Z7K, Z2E-Z7E, Z3F-Z7F and Z1E+Z9E on page 131. As one would expect, the auto-correlation (on the diagonals) is 1 for $\tau = 0$ and then drops to zero ($\text{sinc}(x)$ behavior of the auto-correlation function, because the noise is band limited). The cross-correlation (different gradiometers) fluctuates around zero. For the individual magnetometers the situation is different (see page 132 right). The cross-correlation is about 0.3 for $\tau = 0$.

Result of the analysis: The noise of the gradiometers is not correlated. Therefore the data of different gradiometers can be combined.

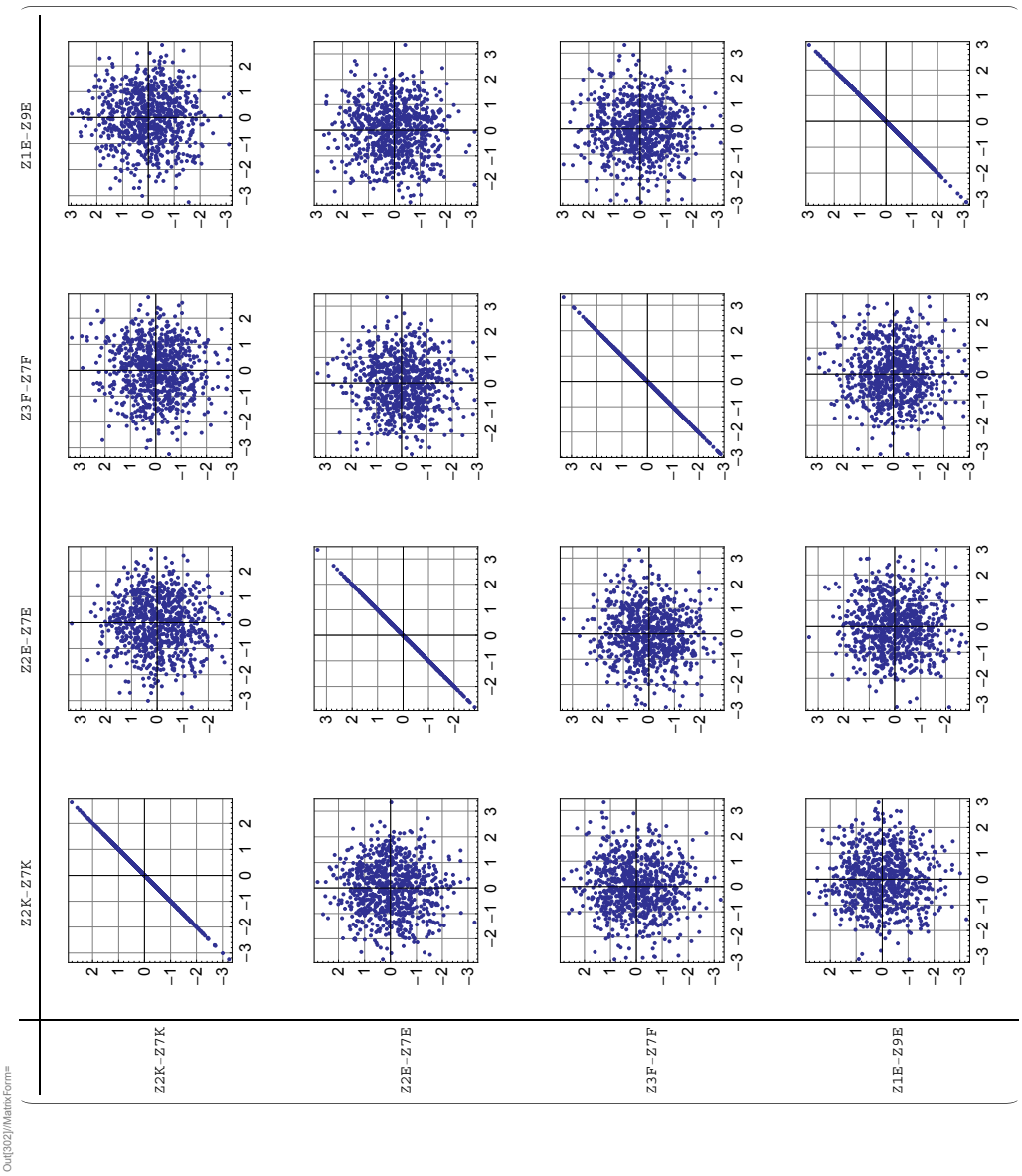

Figure A.1: Scatter plots for all combinations of the gradiometers Z2K-Z7K, Z2E-Z7E, Z3F-Z7F and Z1E+Z9E, which are used for the evaluation of the Lorentz invariance violation data (800 points each).

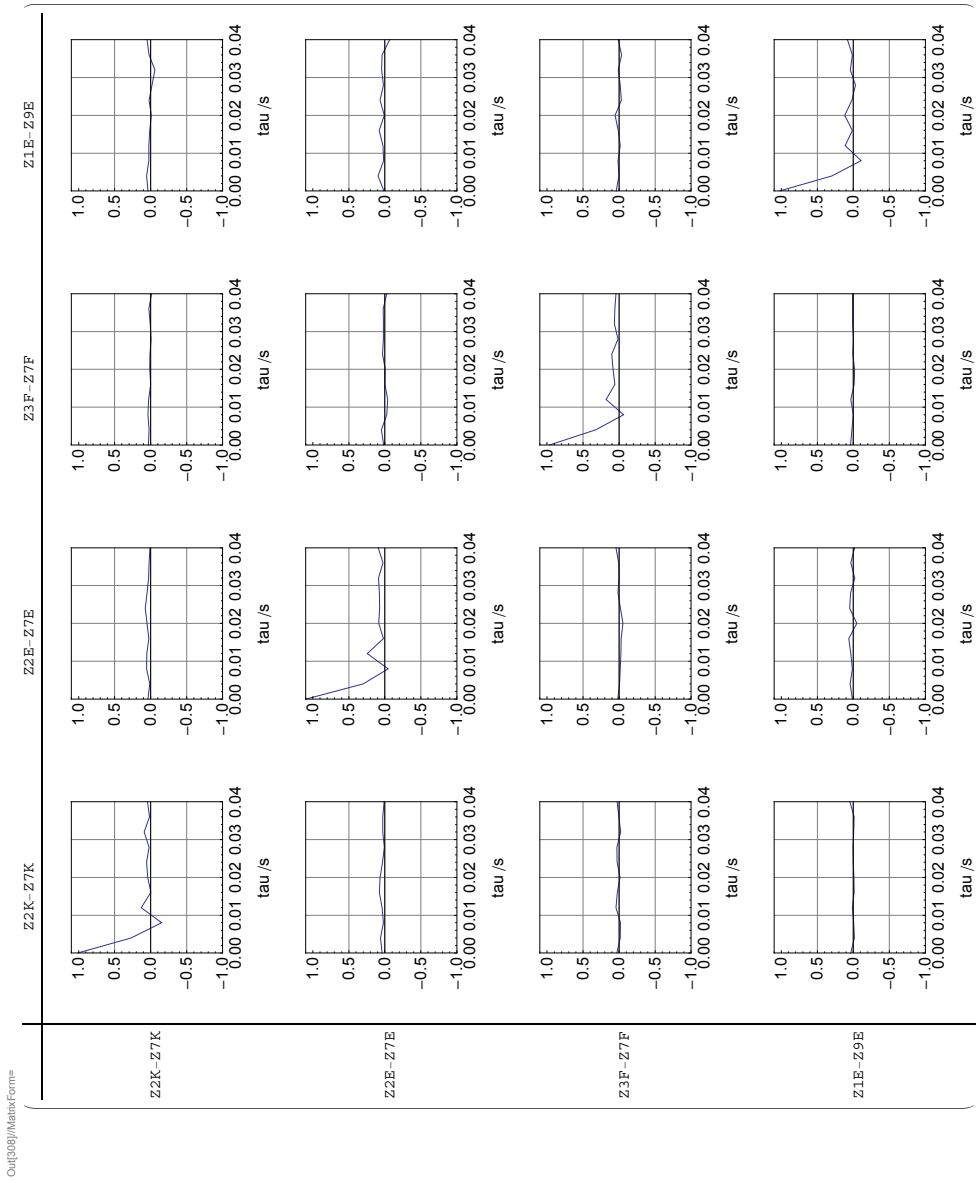

Figure A.2: Auto- resp. cross-correlation as a function of τ for all combinations of the gradiometers Z2K-Z7K, Z2E-Z7E, Z3F-Z7F and Z1E+Z9E.

Figure A.3: Scatter plots and auto- resp. cross-correlation as a function of τ for the combination of the single magnetometers Z2K and Z7K.

A.3 Calculation of the upper limits on $\tilde{b}^{\mathrm{n}}_\perp$

As the Earth's rotation is used to modulate a posited frequency shift in the Larmor frequencies due to the coupling of the spins to a hypothetical background field $\tilde{\boldsymbol{b}}^{\mathrm{n}}$, only the components perpendicular to the Earth axis can be measured. These two components $\tilde{b}^{\mathrm{n}}_{\mathrm{x}}$ and $\tilde{b}^{\mathrm{n}}_{\mathrm{y}}$ can directly be extracted from the fit result. However, if the result is consistent with a zero background field, it is useful to determine upper limits on the magnitude $\tilde{b}^{\mathrm{n}}_\perp$ of such a field, while the direction stays unspecified. In the following paragraphs, a consistent and statistically sound method will be presented how such an upper limit should be calculated.

A.3.1 Test for zero effect

The null hypothesis is: There is no background field,

$$\left\langle \begin{pmatrix} \tilde{b}^{\mathrm{n}}_x \\ \tilde{b}^{\mathrm{n}}_y \end{pmatrix} \right\rangle = \begin{pmatrix} 0 \\ 0 \end{pmatrix} \quad . \tag{A.13}$$

The measurement of the components of the background field has an uncertainty σ. To simplify the argument we can assume that the measurement sensitivity is isotropic. This is not exactly the case due to slightly different measurement times and thus different statistics for the x and y components. But the principle stays the same, with the difference that the following integrals will have to be solved numerically.
The probability density function (pdf) to measure a specific pair (b_x, b_y) is given by:

$$f(b_x, b_y) = \frac{1}{2\pi\sigma^2} \cdot \exp(-\frac{1}{2\sigma^2}(b_x^2 + b_y^2)) \tag{A.14}$$

Transformation to polar coordinates and integration over φ gives the pdf to measure a specific value $b_\perp = \sqrt{b_x^2 + b_y^2}$:

$$g(b_\perp) = \frac{b_\perp}{\sigma^2} \cdot \exp(-\frac{b_\perp}{2\sigma^2}) \tag{A.15}$$

The expectation value of this pdf is $< b_\perp >= \sqrt{\frac{\pi}{2}}\sigma$ and the standard deviation is $\sigma_\perp = \sqrt{2 - \frac{\pi}{2}}\sigma \approx 0.66\sigma$.
One has to reject the null hypothesis if the measured value $b_\perp$ is larger than $b^0_\perp$, which is a solution of the following equation:

$$\int_0^{b^0_\perp} g(b_\perp) db_\perp \stackrel{!}{=} 95\% \tag{A.16}$$

For our measurements with $\sigma \approx 5 \cdot 10^{-34}$ GeV one finds $b^0_\perp \approx 12 \cdot 10^{-34}$ GeV.
The measured values are $b_\perp = \sqrt{b_x^2 + b_y^2} = 5 \cdot 10^{-34}$ GeV. Thus there is no reason to reject the null hypothesis.

A.3.2 First method

The probability density function for a certain result if one repeats the measurement in our case is given by the two-dimensional normal distribution

$$N(x, y; x_0, \sigma_x, y_0, \sigma_y, \rho) \tag{A.17}$$

with the expectation value $(x_0, y_0) = (\tilde{b}_x^{\mathrm{n}}, \tilde{b}_y^{\mathrm{n}})$, the standard deviations σ_x and σ_y and the correlation (between x and y) ρ. The integration of this pdf over a circle with center $(0, 0)$ and radius R gives the probability p, that a repeated measurement would result in $\tilde{b}_\perp^{\mathrm{n}} = \sqrt{(\tilde{b}_x^{\mathrm{n}})^2 + (\tilde{b}_y^{\mathrm{n}})^2} < R$.

$$\begin{aligned} p &= \int_{circle} d^2\vec{r}\ \ N(x, y; x_0, \sigma_x, y_0, \sigma_y, \rho) \\ &= \int_{-R}^{R} dx \int_{-\sqrt{R^2-x^2}}^{\sqrt{R^2-x^2}} dy \frac{1}{2\pi\sigma_x\sigma_y\sqrt{1-\rho^2}} \\ &\cdot \exp\left[-\frac{1}{2(1-\rho^2)}\left(\left(\frac{x-x_0}{\sigma_x}\right)^2 - 2\rho\left(\frac{x-x_0}{\sigma_x}\right)\left(\frac{y-y_0}{\sigma_y}\right) + \left(\frac{y-y_0}{\sigma_y}\right)^2\right)\right] \end{aligned} \tag{A.18}$$

The integral is solved numerically and one chooses R in a way, so that $p = 68\%$ resp. $p = 95\%$.
This method was probably used by [12].

A.3.3 Second method

The first method is too conservative in some points: If the expectation value of the hypothetical background field is indeed $\left\langle \begin{pmatrix} \tilde{b}_x^{\mathrm{n}} \\ \tilde{b}_y^{\mathrm{n}} \end{pmatrix} \right\rangle = \begin{pmatrix} 0 \\ 0 \end{pmatrix}$ (this is: there is no background field), the direction of the field is not defined. And if the result of the measurement is consistent with zero, one can give no statement about the direction of the background field. However, in the probability density function that is used for the first method the direction bears a meaning.
In the following paragraph it will be shown that one can derive even tighter limits on the magnitude $\tilde{b}_\perp^{\mathrm{n}}$ of a posited Lorentz invariance violating background field if the direction of such a field stays undetermined.
Let μ_t be the true (but unknown) value of the magnitude $\tilde{b}_\perp^{\mathrm{n}}$ and let x_0 be the experimentally determined value. In our case this is $x_0 = \sqrt{4.1^2 + 2.9^2} \cdot 10^{-34}\mathrm{GeV} = 5 \cdot 10^{-34}\mathrm{GeV}$.
Then, let $L(x|\mu_t)$ be the probability density function to measure a specific value x as a function of the "true" value μ_t. $L(x|\mu_t)$ can be calculated by taking the two-dimensional normal distribution $(\tilde{b}_x^{\mathrm{n}}, \tilde{b}_y^{\mathrm{n}})$, transforming to polar coordinates (x, ϕ) and integration over ϕ (the direction has no meaning). For $\mu_t = 0$ and $\sigma_x = \sigma_y$ this can be solved numerically. In other cases one has to solve this numerically. The result is shown in Fig. A.4 for an energy resolution of $\sigma = 5.5 \cdot 10^{-34}\mathrm{GeV}$.
A cut through the x-L-plane with $\mu_t = 0$ is shown in Fig. A.5 (top). This is exactly

described by Eq. (A.15). For larger μ_t this distribution approaches the normal distribution (see Fig. A.5 (bottom)).

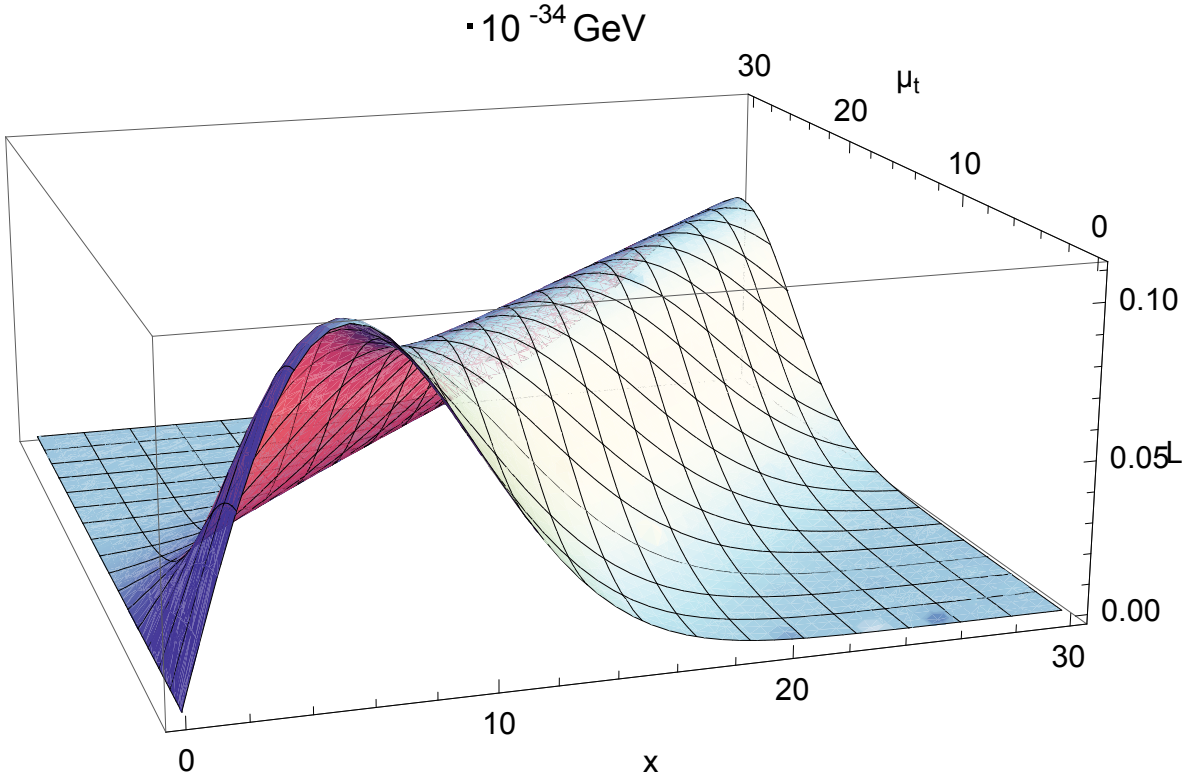

Figure A.4: $L(x|\mu_t)$ is the probability density function to measure a specific value x as a function of the "true" value μ_t.

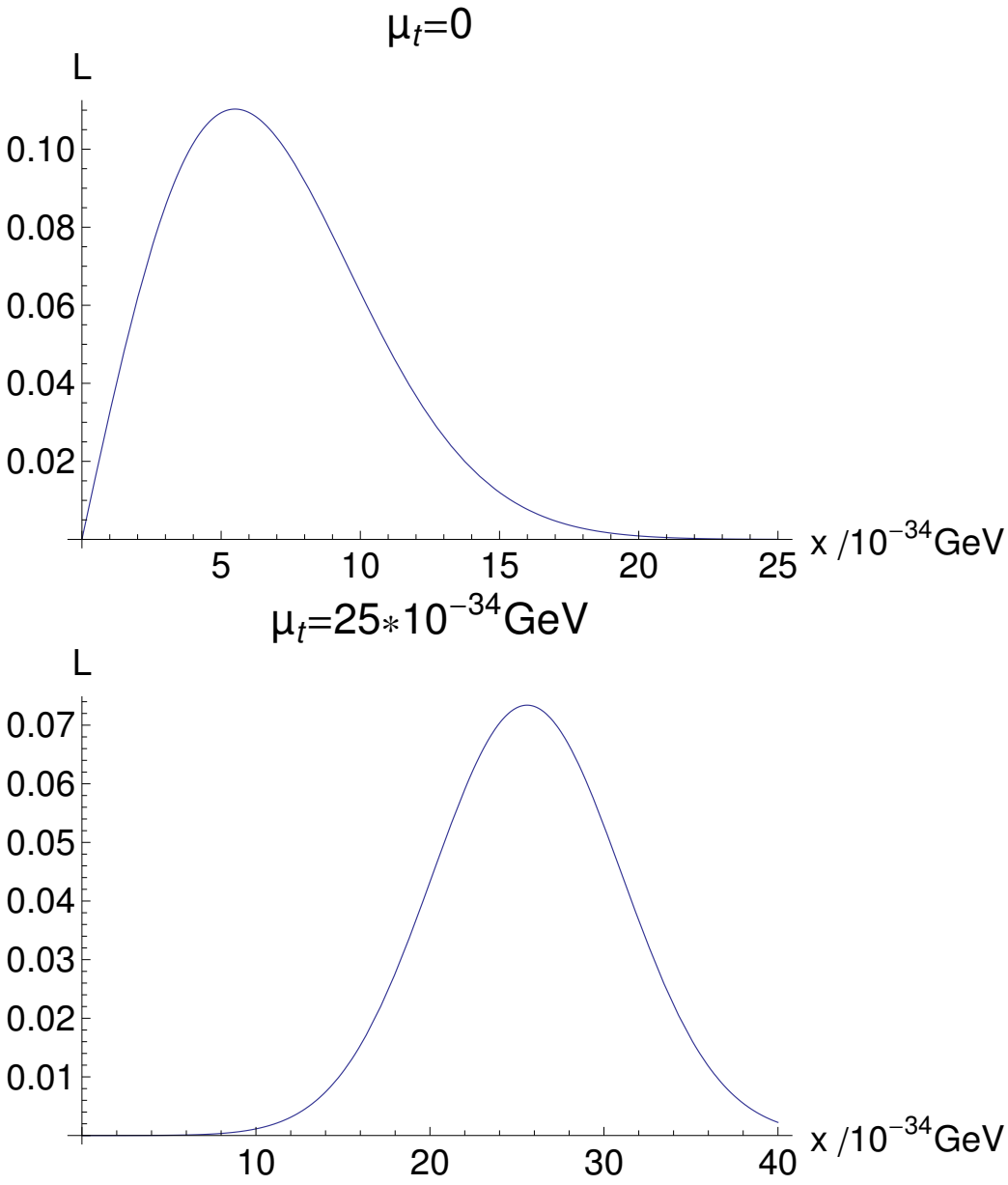

Figure A.5: $L(x|\mu_t)$ with the fixed values $\mu_t = 0$ und $\mu_t = 25 \cdot 10^{-34}$GeV.

Let $P(\mu_t|x_0)$ be the distribution that describes the probability density of the true value μ_t as a function of the measured value x_0. Taking Bayes' Theorem one can calculate $P(\mu_t|x_0)$ from $L(x|\mu_t)$:

$$P(\mu_t|x_0) = L(x|\mu_t) \cdot \frac{P_1(\mu_t)}{P_2(x_0)} \tag{A.19}$$

Here $P_1(\mu_t)$ is the a-priory-probability density function of μ_t. In our case we know nothing about this true value μ_t (except that it is the magnitude of a field and therby positive). Thus one assumes that $P_1(\mu_t)$ is equally distributed in the in the interval

$[0;\infty[$. $P_2(x_0)$ is the a-priory probability density function to measure a specific value x_0. The ratio Norm$=\frac{P_1(\mu_t)}{P_2(x_0)}$ is consequently a normalization factor that depends on x_0 and can be calculated using

$$1 \stackrel{!}{=} \int_0^\infty \text{Norm} \cdot L(x_0|\mu_t) d\mu_t \ . \tag{A.20}$$

The distribution $P(\mu_t|x_0)$ is a cut through the L-μ_r-plane of $L(x|\mu_t)$ with a constant $x = x_0$ (including the normalization factor). In Fig. A.6 such a cut including the normalization for $x_0 = 5 \cdot 10^{-34}$GeV is shown.

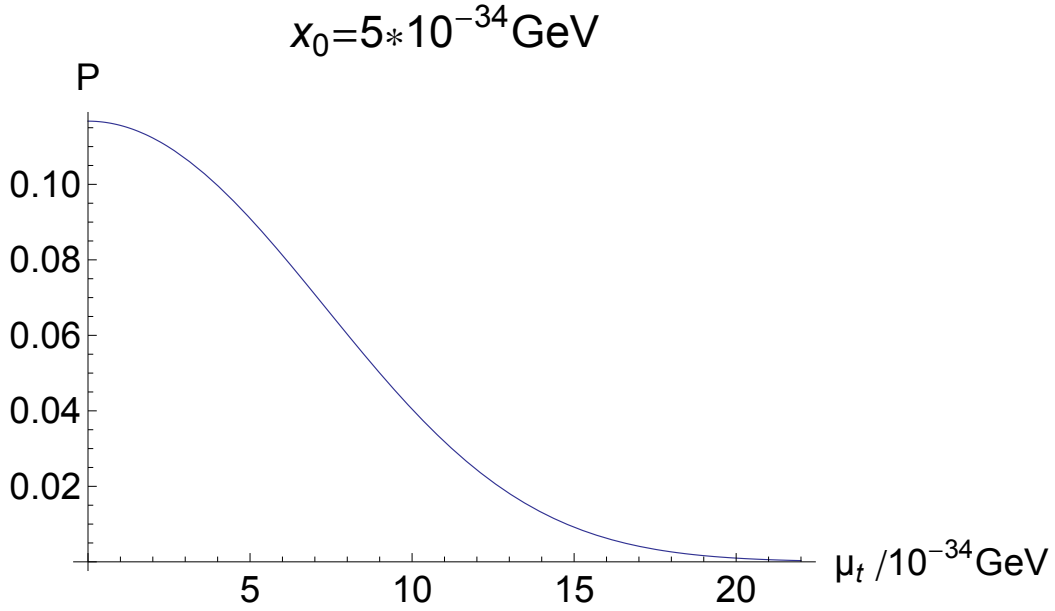

Figure A.6: $P(\mu_t|x_0)$ is the distribution that describes the probability density of the true value μ_t as a function of the measured value $x_0 = 5 \cdot 10^{-34}$GeV.

The confidence intervals or upper limits G for the magnitude of the background field can be derived by integrating $P(\mu_t|x_0)$ (with experimental result $x_0 = 5 \cdot 10^{-34}$GeV):

$$\int_0^G p(\mu_t|x_0) d\mu_t = \int_0^G \text{Norm} \cdot L(x_0|\mu_t) d\mu_t \stackrel{!}{=} 1 - \alpha = \begin{cases} 68\% \\ 95\% \end{cases} \tag{A.21}$$

This results in $G = 6.7 \cdot 10^{-34}$GeV (68%) resp. $G = 13 \cdot 10^{-34}$GeV (95%) and can be interpreted as:

$\tilde{b}_\perp^{\text{n}} < 6.7 \cdot 10^{-34}$ GeV,	68% Confidence Level	
$\tilde{b}_\perp^{\text{n}} < 1.3 \cdot 10^{-33}$ GeV,	95% Confidence Level	(A.22)

A.3.4 Remarks

- For large experimentally determined values ($x_0 \gg \sigma$), $P(\mu_t|x_0)$ transforms into the normal distribution (see Fig. A.7). This limit can be easily calculated in classical statistics ("Frequentist Approach") and as expected one gets the same result.
- This second method (using Bayes' Theorem) can be used without any changes if one can not easily answer the question if the measurement result is compatible with zero.
- This method allows to combine the results of different experiments to put even tighter limits on $\tilde{b}_{\perp}^{n}$, e. g. by adjusting the a-priory-probability density function $P_1(\mu_t)$.

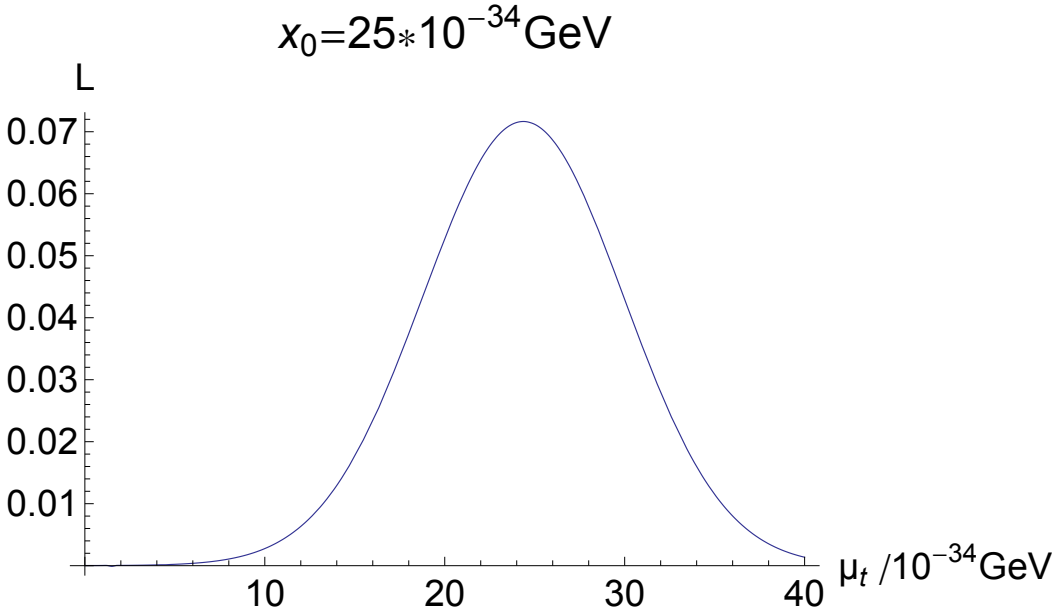

Figure A.7: $P(\mu_t|x_0)$ is the distribution that describes the probability density of the true value μ_t as a function of a hypothetically measured value $x_0 = 25 \cdot 10^{-34}$GeV that is by far larger than the energy resolution of the experiment.

A.4 Details on the the current sources

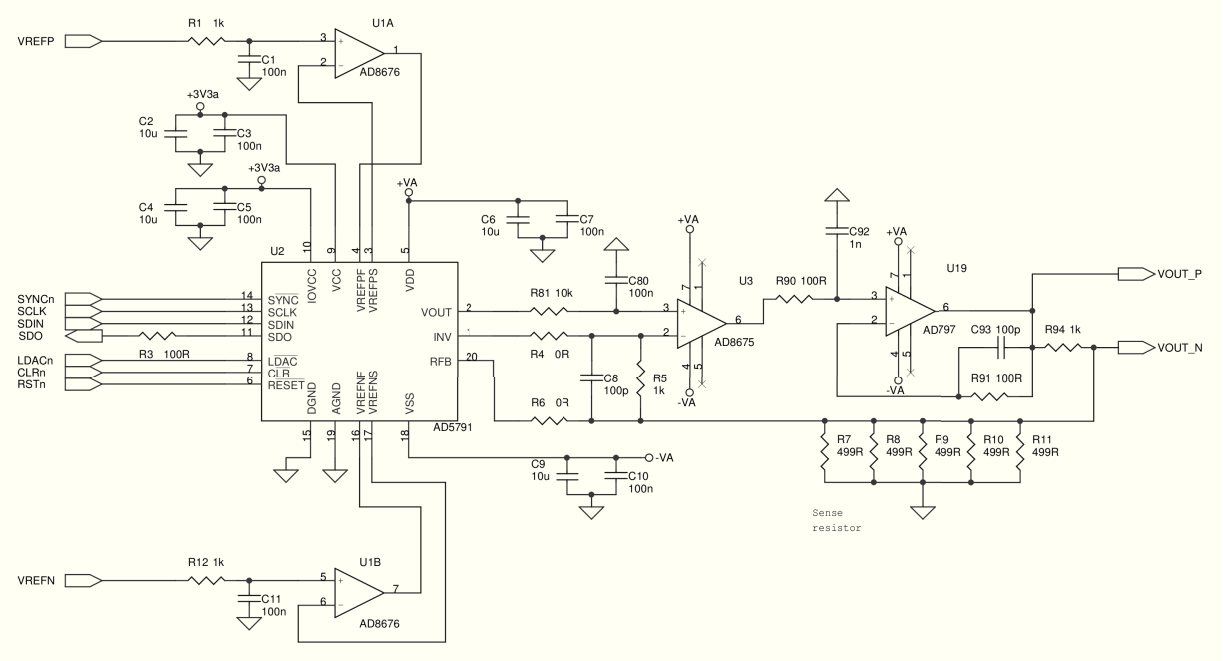

Figure A.8: Schematic of the high-precision low-noise dual current source (single output stage). The current source is controlled from the outside via an optical link and it is powered by LiPo cells. A micro-controller is used for the communication via the optical link and to control the digital-to-analog converters (DACs). The output voltage of the 20-bit DAC AD5791 is filtered (low-pass filter of C80 and R81) and buffered by an AD8675 low-noise operational amplifier. Then the output current is driven by an AD797 operational amplifier. Finally, the current through the load resistance causes a voltage drop over the sense resistors (R7...R11) that is coupled back into a feed-back mechanism. (R94 is only needed if there is no external load attached.)

B Influence of the SQUID position on the measured amplitude and phase

A uniformly magnetized sphere of radius R_0 and magnetization $\boldsymbol{M}$ produces a homogeneous magnetic field $\boldsymbol{B}_{in} = \frac{2\mu_0}{3}\boldsymbol{M}$ inside the sphere. The field outside the sphere is the field of a dipole $\boldsymbol{p} = \frac{4\pi R_0^3}{3}\boldsymbol{M}$ at the center of the sphere. This result can be found in [50], for example. Thus, the external field of a spherical sample cell filled with precessing spins can be described by a rotating dipole $\boldsymbol{p}(t)$ at the center of the cell, e. g.

$$\boldsymbol{p}(t) \;=\; p_0 \cdot (\sin(\omega t), 0, \cos(\omega t)) \tag{B.1}$$

for a magnetic guiding field pointing into the y-direction.
The field of a dipole in the origin is

$$\boldsymbol{B}(\boldsymbol{r}) \;=\; \frac{\mu_0}{4\pi}\left(3\frac{\boldsymbol{p}\cdot\boldsymbol{r}}{r^5}\boldsymbol{r} - \frac{\boldsymbol{p}}{r^3}\right) \tag{B.2}$$

with $r = |\boldsymbol{r}|$. Thus, a **point-like central SQUID** at the position $\boldsymbol{r} = (0, 0, R)$ measuring the z-component of the magnetic field would give a signal proportional to

$$\begin{aligned} B_z &= \frac{\mu_0}{4\pi}\left(3\frac{p_z \cdot R^2}{R^5} - \frac{p_z}{r^3}\right) \\ &= \frac{\mu_0}{2\pi}\frac{p_0}{R^3}\cos(\omega t)\ . \end{aligned} \tag{B.3}$$

More general, the signal of a point-like SQUID measuring the z-component of the magnetic field at the position $\boldsymbol{r} = (x, y, z)$ with $R = \sqrt{x^2 + y^2 + z^2}$ is proportional to

$$\begin{aligned} B_z &= \frac{\mu_0}{4\pi}\left(3\frac{p_x \cdot x + p_z \cdot z}{R^5} \cdot z - \frac{p_z}{r^3}\right) \\ &= \frac{\mu_0}{4\pi} p_0 \left[\frac{3xz}{R^5}\sin(\omega t) + \left(\frac{3z^2}{R^5} - \frac{1}{R^3}\right)\cos(\omega t)\right]\ , \end{aligned} \tag{B.4}$$

i. e. a signal proportional to $\cos(\omega t + \varphi_{\text{pos}})$ with a phase that depends on the SQUID position

$$\varphi_{\text{pos}} \;=\; \arctan\left(\frac{3xz}{3z^2 - R^2}\right)\ . \tag{B.5}$$

In the case $\sqrt{x^2 + y^2} \ll z$ this can be approximated by $\varphi_{\text{pos}} \approx \frac{3x}{2R}$.
To investigate the influence of the spatial extent on the measured amplitude: The SQUID has a spatial extent measuring the flux through a certain area $\boldsymbol{A}$. In this case the area is a circle with radius ρ. Then for a central SQUID at the position $\boldsymbol{r} = (0, 0, R)$

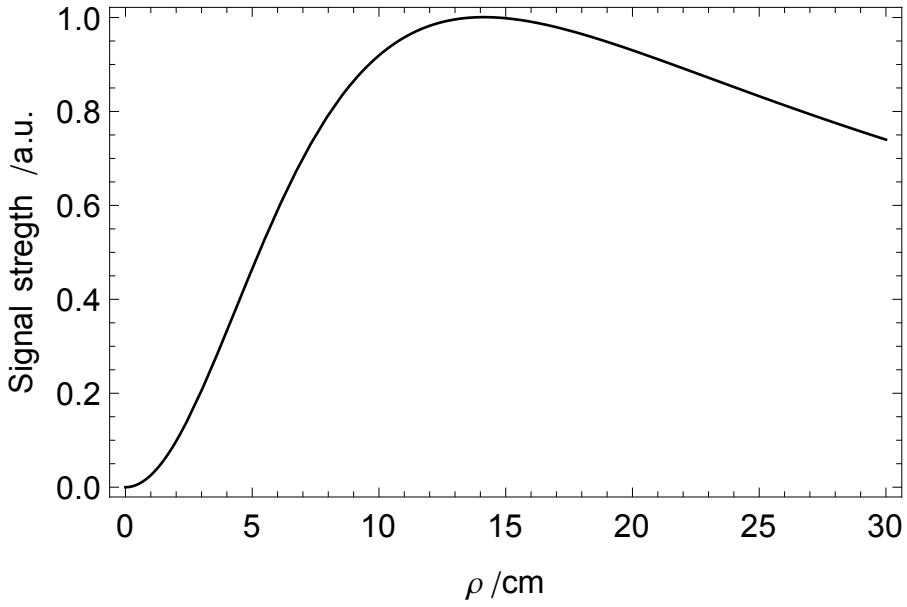

Figure B.1: The measured signal amplitude as a function of the pick-up loop radius ρ for $R = 10$ cm.

measuring the z-component of the magnetic field would give a signal proportional to

$$\begin{aligned}
\Phi(t) &= \int_A \boldsymbol{B}(t) d\boldsymbol{A} = \int_A B_z(t) dA \\
&= \int_{-\rho}^{\rho} dx \int_{-\sqrt{\rho^2-x^2}}^{\sqrt{\rho^2-x^2}} dy B_z(t, x, y, z = R) \\
&= \int_{-\rho}^{\rho} dx \int_{-\sqrt{\rho^2-x^2}}^{\sqrt{\rho^2-x^2}} dy \frac{\mu_0}{4\pi} \left[3 \frac{\boldsymbol{p} \cdot (x, y, R)}{(R^2 + x^2 + y^2)^{5/2}} \cdot R - \frac{p_z}{(R^2 + x^2 + y^2)^{3/2}} \right] \cdot \cos(\omega t) \\
&= \frac{\mu_0}{2} p_0 \frac{\rho^2}{(R^2 + \rho^2)^{3/2}} \qquad \text{(B.6)}
\end{aligned}$$

Thus, if $\rho \ll R$ the measured signal amplitude increases linearly with the sensitive area of the SQUID (e.g. the area enclosed by the pick-up loop). Laborbuch Seite 62 bis 66

C Lists

C.1 List of Figures

C.2 List of Tables

D Bibliography

[1] A. D. Sakharov "Violation of CP invariance, C asymmetry, and baryon asymmetry of the universe". Journal of Experimental and Theoretical Physics **5**: 24-27 (1967).

[2] J. Schwinger "The Theory of Quantized Fields I". Physical Review **82** (1951).

[3] G. Lüders "On the Equivalence of Invariance under Time Reversal and under Particle-Antiparticle Conjugation for Relativistic Field Theories". Kongelige Danske Videnskabernes Selskab, Matematisk-Fysiske Meddelelser **28** (1954).

[4] Planck Mission, "Planck 2013 results. I. Overview of products and scientific results". arXiv:1303.5062.

[5] Y. V. Stadnik and V. V. Flambaum, arXiv:1408.2184.

[6] A. A. Michelson and E.W. Morley, Am. J. Sci. **34**, 333 (1887).

[7] Ch. Eisele, A.Yu. Nevsky, and S. Schiller, Phys. Rev. Lett. **103**, 090401 (2009).

[8] S. Herrmann *et al.*, Phys. Rev. D **80**, 105011 (2009).

[9] V. W. Hughes, H. G. Robinson, and V. Beltran-Lopez, Phys. Rev. Lett. **4**, 342 (1960).

[10] R. W. P. Drever, Philos. Mag. **6**, 683 (1961).

[11] J. D. Prestage, J. J. Bollinger, Wayne M. Itano, and D. J. Wineland , Phys. Rev. Lett. **54**, 2387 (1985).

[12] J. M. Brown, S. J. Smullin, T.W. Kornack, and M.V. Romalis, Phys. Rev. Lett. **105**, 151604 (2010).

[13] M. Smiciklas *et al.*, "New Test of Local Lorentz Invariance Using a 21Ne-Rb-K Comagnetometer". Phys. Rev. Lett. **107** (17): 171604 (2011).

[14] S. K. Lamoreaux *et al.*, Phys. Rev. Lett. **57**, 3125 (1986).

[15] S. K. Lamoreaux *et al.*, Phys. Rev. A **39**, 1082 (1989).

[16] T. E. Chupp *et al.*, Phys. Rev. Lett. **63**, 1541 (1989).

[17] C. J. Berglund *et al.*, Phys. Rev. Lett. **75**, 1879 (1995).

[18] D. Bear, R. E. Stoner, and R. L. Walsworth, Phys. Rev. Lett. **85**, 5038 (2000).

[19] D. Bear *et al.*, Phys. Rev. Lett. **89**, 209902(E) (2002).

[20] D. F. Phillips *et al.*, Phys. Rev. D **63**, 111101(R) (2001).

[21] F. Canè *et al.*, Phys. Rev. Lett. **93**, 230801 (2004).

[22] B. R. Heckel *et al.*, Phys. Rev. D **78**, 092006 (2008).

[23] B. R. Heckel *et al.*, "New CP-Violation and Preferred-Frame Tests with Polarized Electrons", Phys. Rev. Lett. **97** (2), 021603 (2006).

[24] I. Altarev *et al.*, Phys. Rev. Lett. **103**, 081602 (2009).

[25] S. K. Peck *et al.*, Phys. Rev. A **86**, 012109 (2012).

[26] D. Colladay and V. A. Kostelecký, Phys. Rev. D **58**, 116002 (1998).

[27] V. A. Kostelecký and C. D. Lane, Phys. Rev. D **60**, 116010 (1999).

[28] V. A. Kostelecký and S. Samuel, Phys. Rev. D **39**, 683 (1989).

[29] R. Bluhm, Lect. Notes Phys. **702**, 191 (2006).

[30] O. W. Greenberg, "CPT Violation Implies Violation of Lorentz Invariance". Phys. Rev. Lett. **89** (23), (2002).

[31] J. Ellis, N. E. Mavromatos, and D. V. Nanopoulos, Phys. Rev. D **63**, 024024 (2000), and references therein.

[32] D. Sudarsky, L. Urrutia, and H. Vucetich, Phys. Rev. Lett. **89**, 231301 (2002).

[33] H. Nicolai, K. Peeters, and M. Zamaklar, Class. Quantum Grav. **22**, R193 (2005).

[34] R. Gambini and J. Pullin, Phys. Rev. D **59**, 124021 (1999).

[35] P. M. Crichigno and H. Vucetich, Phys. Lett. B **651**, 313 (2007).

[36] A. Kostelecký and N. Russell, arXiv:0801.0287v6.

[37] C. Gemmel *et al.*, Phys. Rev. D **82**, 111901(R) (2010).

[38] C. Gemmel *et al.*, Eur. Phys. J. D **57**, 303 (2010).

[39] C. Gemmel, "Test of Lorentz Symmetry with a ^{3}He/^{129}Xe Clock-Comparison Experiment", Dissertation, Universität Mainz, (2010).

[40] W. Heil *et al.*, Ann. Phys. (Berlin) **525**, 539 (2013).

[41] K. Tullney *et al.*, Phys. Rev. Lett. **111**, 100801 (2013).

[42] K. Tullney, "Search for a Spin-Dependent Short-Range Force between Nucleons with a ^{3}He/^{129}Xe Clock-Comparison Experiment", Dissertation, Universität Mainz, (2013).

[43] J. Bork et al., in Biomag 2000: Proceedings of the 12th International Conference on Biomagnetism (Springer, New York, 2000), p. 970.

[44] B. C. Anger *et al.*, Phys. Rev. A **78**, 043406 (2008).

[45] International Council for Science: Committee on Data for Science and Technology (CODATA), www.codata.org, (2007).

[46] M. Pfeffer and O. Lutz, J. Magn. Reson. A **108**, 106 (1994).

[47] C. D. Hoyle *et al.*, Phys. Rev. D **70**, 042004 (2004).

[48] F. Bloch and A. Siegert, Phys. Rev. **57**, 522 (1940).

[49] N.F. Ramsey, Phys. Rev. **100**, 1191 (1955).

[50] J.D. Jackson,"Classical Electrodynamics" (3rd Edition), (Wiley, New York, 1999) (pp. 198-200).

[51] S. M. Kay, "Fundamentals of Statistical Signal Processing: Estimation Theory (Vol. 1)", (Prentice Hall, New Jersey, 1993), specifically chapter 7.

[52] F. Allmendinger *et al.*, arXiv:1307.5165

[53] F. Allmendinger *et al.*, Phys. Rev. Lett **112** (11): 110801 (2014).

[54] U. Schmidt *et al.*, arXiv:1307.5604

[55] D. W. Allan, "Statistics of Atomic Frequency Standards, Proceedings of IEEE", **54**, pp. 221–230, (1966).

[56] D. W. Allan, "The measurement of frequency and frequency stability of precision oscillators", Proc. Sixth Ann. Precise Time and Time Interval Planning Meet., Washinton, DC, pp. 109-142, (1974).

[57] J.A. Barnes et al., IEEE Trans. Instrum. Meas. **20**, 105 (1971).

[58] Th. Schmidt, Z. Phys. **106**, 358 (1937).

[59] P. L. Anthony *et al.*, Phys. Rev. D **54**, 6620 (1996).

[60] V. A. Dzuba, V.V. Flambaum, and P. G. Silvestrov, Phys. Lett. B **154**, 93 (1985).

[61] H. Harcken *et al.*, J. Magn. Reson. **206**, 168-170 (2010).

[62] J. S. M. Ginges and V. V. Flambaum, Physics Reports **397** (2004).

[63] V. A. Dzuba, V. V. Flambaum, J. S. M. Ginges and M. G. Kozlov, Phys. Rev. A **66** (2002).

[64] B. Regan, E. Commins, C. Schmidt, D. DeMille, Phys. Rev. Lett. **88**, 071805 (2002).

[65] J. J. Hudson *et al.*, Nature **473**, 493–496 (2011).

[66] D. M. Kara *et al.*, New J. Phys. 14, 103051 (2012).

[67] The ACME Collaboration, "Order of Magnitude Smaller Limit on the Electric Dipole Moment of the Electron", Science **343**, 269 (2014).

[68] J. H. Smith, E. M. Purcell, N. F. Ramsey, "Experimental Limit to the Electric Dipole Moment of the Neutron". Physical Review **108**: 120–122, (1957).

[69] C. A. Baker *et al.* , "Improved Experimental Limit on the Electric Dipole Moment of the Neutron". Physical Review Letters **97** (13), (2006).

[70] W. C. Griffith *et al.*, Phys. Rev. Lett. **102**, 101601 (2009).

[71] W. C. Griffith, "Limiting CP violation through a search for a permanent electric dipole moment of Mercury 199 atoms", Dissertation, University of Washington, (2009).

[72] M. D. Swallows *et al.*, Phys. Rev. A **87**, 012102 (2013).

[73] M. A. Rosenberry and T. E. Chupp, "Atomic Electric Dipole Moment Measurement Using Spin Exchange Pumped Masers of ^{129}Xe and ^{3}He", Phys. Rev. Lett **89**, (2001).

[74] M. A. Rosenberry, "A precision measurement of the ^{129} electric dipole moment using dual noble gas masers", Dissertation, University of Michigan, (2000).

[75] C. P. Slichter. "Principles of Magnetic Resonance". Springer, (1978).

[76] A. G. Redfield, IBM J.Research Develop. **1**,19 (1957).

[77] G.D. Cates, S.R. Schaefer and W. Happer, Phys. Rev. A **37**, 2877 (1988).

[78] G. D. Cates, D. J. White, T. Chien, S. R. Schaefer, and W. Happer, Phys. Rev. A **38**, (1988).

[79] D.D. McGregor, Phys. Rev. A **41**, 2631 (1990).

[80] R. Barbé, M. Leduc, F. Laloe, J. Phys. France **35**, 935 (1974).

[81] J. Schmiedeskamp, W. Heil, E. W. Otten, R. K. Kremer, A. Simon, and J. Zimmer. "Paramagnetic relaxation of spin polarized ^{3}He at bare glass surfaces", European Physical Journal D, **38**:427-438, (2006).

[82] A. Deninger, W. Heil, E. W. Otten, M. Wolf, R. K. Kremer, and A. Simon. "Paramagnetic relaxation of spin polarized ^{3}He at coated glass walls", European Physical Journal D, **38**:439-443, (2006).

[83] J. Schmiedeskamp, H.-J. Elmers, W. Heil, E. W. Otten, Yu. Sobolev, W. Kilian, H. Rinneberg, T. Sander-Thömmes, F. Seifert, and J. Zimmer, "Paramagnetic relaxation of spin polarized ^{3}He by magnetized ferromagnetic contaminants", European Physical Journal D, **38**:445-454, (2006).

[84] N.R. Newbury, A.S. Barton, G.D. Cates, W. Happer, and H. Middleton, "Gaseous ^{3}He-^{3}He magnetic dipolar spin relaxation", Phys. Rev. A, **48**, (1993).

[85] B. Chann, I.A. Nelson, L.W. Anderson, B. Driehuys, and T.G. Walker, "^{129}Xe-^{129}Xe molecular spin relaxation", Phys. Rev. Lett., **88**, (2002).

[86] M. Wolf. "Erzeugung höchster ^{3}He-Kernspinpolarisation durch metastabiles optisches Pumpen". Dissertation, Universität Mainz, (2004).

[87] S. Appelt, A.B.A. Baranga, C.J. Erickson, M.V. Romalis, A.R. Young, and W. Happer. "Theory of spin-exchange optical pumping of ^{3}He and ^{129}Xe", Physical Review A **58**(2), (1998).

[88] W. Kilian, "Erzeugung von hyperpolarisiertem ^{129}Xe-Gas und Nachweis mittels in vivo NMR-Bildgebung, NMR-Spektroskopie sowie SQUID-Messtechnik", Dissertation, Freie Universität Berlin, (2001).

[89] F. Thiel, A. Schnabel, S. Knappe-Grüneberg, D. Stollfuß, and M. Burghoff, "Demagnetization of magnetically shielded rooms", Rev. Sci. Instrum. **78**, 035106 (2007).

[90] J. Bork, H. Hahlbohm, R. Klein, A. Schnabel, "The 8-layered magnetically shielded room of the PTB: Design and construction", in Biomag2000, Proc. 12th Int. Conf. on Biomagnetism, J. Nenonen, R.J. Ilmoniemi, and T. Katila, eds. (Helsinki Univ. of Technology, Espoo, Finland, 2001), pp. 970-973.

[91] John Clarke and Alex I. Braginski (editors), "The SQUID Handbook: Volume I: Fundamentals and Technology of SQUIDs and SQUID Systems", Wiley-VCH, (2004).

[92] John Clarke and Alex I. Braginski (editors), "The SQUID Handbook: Volume II: Applications of SQUIDs and SQUID Systems", Wiley-VCH, (2006).

[93] F. Thiel, A. Schnabel, S Knappe-Grüneberg, M Burghoff, D Drung, F Petsche, S Bechstein, U Steinhoff, W Müller, D Stollfuß, D Gutkelch, S Hartwig, H-J Scheer, L Trahms and H Koch, Biomed. Technik (Biomedical Engineering), **50**, (2005).

[94] Magnicon GmbH, Hamburg, Germany, www.magnicon.com.

[95] ISEG Spezialelektronik GmbH, Radeberg, Germany, www.iseg-hv.com.

[96] S. K. Lamoreaux, Phys. Rev. A **53**, 6 (1996).

[97] S. K. Lamoreaux and R. Golub, J. Phys. G: Nucl. Part. Phys. **36**, (2009).

[98] G. Pignol and S. Roccia, Phys. Rev. A **85**, (2012).